Novel Theory for Shear Stress Computation in Cracked Reinforced Concrete Flexural Beams

by

AlaaEldin Abouelleil

B.S., Kansas State University, 2013
M.S., Kansas State University, 2015

AN ABSTRACT OF A DISSERTATION

submitted in partial fulfillment of the requirements for the degree

DOCTOR OF PHILOSOPHY

Department of Civil Engineering
College of Engineering

KANSAS STATE UNIVERSITY
Manhattan, Kansas

2018

Abstract

This study is conducted because of the lack of an existing theory to accurately predict the diagonal tension cracking in shallow reinforced concrete beams. A rational approach is followed to numerically derive the shear stress profile across the depth of the beam in cracked beams based on the smeared crack approach. Furthermore, the determined shear stress distribution coupled with the normal axial stress distribution are used to predict the principal stress variation across the depth and along the shear span using standard Mohr's circle. Following a biaxial stress cracking criterion, the likely diagonal tension cracks along their orientation profile are predicted.

Furthermore, this study is conducted to provide a mechanics-based understanding of the shear stress distribution in cracked reinforced concrete. This approach utilizes the transversal shear differential equation to evaluate the shear stress at any given depth by the variation of the axial stress distribution within an infinitesimal beam segment at that depth. In addition, this study presents a more accurate representation of the change in the strain profile parameters with respect to the sectional applied moment. Furthermore, the dowel action effect is derived to illustrate its significance on the shear stress distribution at various stages of loading.

Novel Theory for Shear Stress Computation in Cracked Reinforced Concrete Flexural Beams

by

AlaaEldin Abouelleil

B.S., Kansas State University, 2013
M.S., Kansas State University, 2015

A DISSERTATION

submitted in partial fulfillment of the requirements for the degree

DOCTOR OF PHILOSOPHY

Department of Civil Engineering
College of Engineering

KANSAS STATE UNIVERSITY
Manhattan, Kansas

2018

Approved by

Major Professor
Dr. Hayder A. Rasheed

Copyright

Abstract

This study is conducted because of the lack of an existing theory to accurately predict the diagonal tension cracking in shallow reinforced concrete beams. A rational approach is followed to numerically derive the shear stress profile across the depth of the beam in cracked beams based on the smeared crack approach. Furthermore, the determined shear stress distribution coupled with the normal axial stress distribution are used to predict the principal stress variation across the depth and along the shear span using standard Mohr's circle. Following a biaxial stress cracking criterion, the likely diagonal tension cracks along their orientation profile are predicted.

Furthermore, this study is conducted to provide a mechanics-based understanding of the shear stress distribution in cracked reinforced concrete. This approach utilizes the transversal shear differential equation to evaluate the shear stress at any given depth by the variation of the axial stress distribution within an infinitesimal beam segment at that depth. In addition, this study presents a more accurate representation of the change in the strain profile parameters with respect to the sectional applied moment. Furthermore, the dowel action effect is derived to illustrate its significance on the shear stress distribution at various stages of loading.

Table of Contents

List of Figures

List of Tables

Acknowledgements

I wish to express my sincere appreciation to my major advisor, Dr. Hayder A. Rasheed for his guidance and support that he provided during my pursuit of the Doctoral Degree. I would also like to acknowledge and thank Dr. Bacim Alali, Dr. Hani Melhem, and Dr. Christopher Jones for their willingness to serve on my supervisory committee.

Dedication

To my parents and Family

Notations

$\boldsymbol{A_s}$ = Tensile steel area mm^2 (in^2)

$\boldsymbol{A'_s}$ = Compressive steel area mm^2 (in^2)

$\boldsymbol{A_{cc}}$ = The integral of the shear stress profile due to the compressive concrete contribution N/mm (k/in)

$\boldsymbol{A_{cs}}$ = The integral of the shear stress profile due to the compressive steel contribution N/mm (k/in)

$\boldsymbol{A_{tc1}}$ = The integral of the shear stress profile due to the tensile concrete contribution (part 1) N/mm (k/in)

$\boldsymbol{A_{tc2}}$ = The integral of the shear stress profile due to the tensile concrete contribution (part 2) N/mm (k/in)

$\boldsymbol{A_{ts}}$ = The integral of the shear stress profile due to the tensile concrete contribution N/mm (k/in)

$\boldsymbol{c}$ = Compression depth mm (in)

$\boldsymbol{C_c}$ = Concrete compressive force KN (kips)

$\boldsymbol{C_s}$ = Steel compressive force KN (kips)

$\boldsymbol{d}$ = Tension steel depth from the top surface mm^2 (in^2)

$\boldsymbol{d'}$ = Compression steel depth from the top surface mm^2 (in^2)

$\boldsymbol{d_{ts}}$ = Depth (measured from the top surface) at which the concrete tensile model ends mm^2 (in^2)

$\boldsymbol{E_c}$ = Concrete modulus of elasticity MPa (ksi)

$\boldsymbol{E_s}$ = Steel modulus of elasticity MPa (ksi)

$\boldsymbol{E'_s}$ = Steel hardening slope after yielding MPa (ksi)

$\boldsymbol{f_c}$ = Concrete compressive stress MPa (ksi)

$\boldsymbol{f'_c}$ = Concrete maximum compressive stress MPa (ksi)

$\boldsymbol{f_t}$ = Concrete tensile stress MPa (ksi)

$\boldsymbol{f_r}$ = Concrete cracking stress MPa (ksi)

$\boldsymbol{f_y}$ = Steel yielding stress MPa (ksi)

$\boldsymbol{M_{cc}}$ = Moment due to the compressive concrete KN.m (K.in)

$\boldsymbol{M_{cs}}$ = Moment due to the compressive steel KN.m (K.in)

$\boldsymbol{M_{tc1}}$ = Moment due to the tensile concrete (part one) KN.m (K.in)

$\boldsymbol{M_{tc2}}$ = Moment due to the tensile concrete (part two) KN.m (K.in)

$\boldsymbol{M_{ts}}$ = Moment due to the tensile steel

$\boldsymbol{T_{c1}}$ = Concrete tensile force induced due to the first part of the concrete tensile profile KN (kips)

$\boldsymbol{T_{c2}}$ = Concrete tensile force induced due to the second part of the concrete tensile profile KN (kips)

$\boldsymbol{T_s}$= Steel tensile force KN (kips)

$\boldsymbol{\gamma}$ = The centroid of the compressive concrete stress profile to the compression depth ratio KN.m (K.in)

$\boldsymbol{\varepsilon_t}$ = Concrete tensile strain

$\boldsymbol{\varepsilon_{tu}}$ = Concrete tensile strain corresponding to the end of the concrete tensile constitutive model

$\boldsymbol{\varepsilon_{cr}}$ = Concrete cracking strain

$\boldsymbol{\varepsilon_y}$ = Steel yielding strain

$\boldsymbol{\varepsilon_c}$ = Concrete compressive strain

$\boldsymbol{\varepsilon_c'}$ = Concrete compressive strain corresponding to concrete maximum compressive stress

$\boldsymbol{\varepsilon_{cf}}$ = Concrete compressive strain at the maximum compressive fiber

$\boldsymbol{\sigma_1}$ = Major principal tensile stress MPa (ksi)

$\boldsymbol{\sigma_2}$ = Minor principal compressive stress MPa (ksi)

$\boldsymbol{\sigma_{1t}}$ = Major principal tensile stress limit MPa (ksi)

$\boldsymbol{\sigma_{2c}}$ = Minor principal compressive stress limit MPa (ksi)

$\boldsymbol{\tau_{xy}}$ = Transversal shear MPa (ksi)

$\boldsymbol{\tau_{yx}}$ = Longitudinal shear MPa (ksi)

$\boldsymbol{\tau_{cc}}$ = Shear stress due to the compressive concrete contribution MPa (ksi)

$\boldsymbol{\tau_{cs}}$ = Shear stress due to the compressive steel contribution MPa (ksi)

$\boldsymbol{\tau_{tc1}}$ = Shear stress due to the tensile concrete contribution (part 1) MPa (ksi)

$\boldsymbol{\tau_{tc2}}$ = Shear stress due to the tensile concrete contribution (part 2) MPa (ksi)

$\boldsymbol{\tau_{ts}}$ = Shear stress due to the tensile steel contribution MPa (ksi)

$\boldsymbol{\varphi}$ = Cross section curvature 1/mm (1/in)

Chapter 1 - Introduction

1.1 Background

Although many studies have been conducted to fully understand the shear behavior of reinforced concrete beams, the consensus regarding one explanation is missing. There is some sort of agreement regarding the parameters that affect the shear behavior, yet there is no agreement regarding the mechanics of shear behavior. Arch action and beam action are two main explanations which were introduced to represent the shear behavior in cracked reinforced concrete members. However, many researchers suggested a combination of these two approaches. These actions suggest three main mechanisms to transmit shear across the cracked beams without shear reinforcement: the compression zone, aggregate interlock between cracks and dowel action of the longitudinal steel reinforcement. The main parameters that influence the beam behavior includes concrete behavior in tension and compression, beam size effect, aggregate size and shear span to depth ratio.

Among the first researchers to study the behavior of reinforced concrete beams under shear loads is Morsch (1903). He was the first to point out that the shear failure is nothing but a principal tensile failure. Also, he suggested the similarity between web reinforcement behavior and the diagonal members in a truss. However, Talbot (1908-1909), after conducting a series of tests, noted that the stress calculated based on truss analogy is higher than the experimentally measured stresses, yet, he suggested a design modification to limit shear load carried by web reinforcement to two-thirds of the beam capacity. In addition, Talbot's tests showed that beam shear capacity is affected by the concrete characteristics as well as number of longitudinal bars and shear span to effective depth ratio. These findings were confirmed by Richart and Larson (1928). They also stated that stirrup stresses were small until shear cracks are developed and the

point of intersection between the crack and web reinforcement produced the highest stress in the reinforcement. Hognestad (1951) described the concept of stress redistribution upon the commencement of the diagonal tensile cracks in restrained beams, where the original stress distribution is no longer valid around the cracked zone. After two years, Zwoyer (1954) observed the similarity between the diagonal tensile cracks and the flexural compression failure (concrete crushing). Using this observation, Moody et al. (1954) described the failure of reinforced concrete beams to compose of two stages; the first stage includes diagonal tension cracking followed by crushing as a second stage. However, the described failure mode was found to be controlled by (M/Vd) ratio. With smaller ratios, the described mode of failure occurs. Larger (M/Vd) ratio resulted in almost pure flexural failure.

1.2 Objectives

In this study, the authors attempt to present a mechanics based approach to illustrate the behavior of shallow reinforced concrete beams under concentrated load, taking into account the different stages of loading; pre-cracking, post cracking and post yielding. Shear stresses are evaluated based on the shear differential equation and the smeared crack approach. These shear stresses coupled with the normal stress distribution are used to predict the principal stress variation across the depth and along the shear span using standard Mohr's circle. Following a biaxial stress cracking criterion like that of Kupfer and Gerstle (1973), the likely diagonal tension cracks are predicted.

1.3 Scope of Dissertation

The research work in this dissertation includes an introduction to the shear behavior in reinforced concrete beams in chapter one, and then followed by six main chapters. The second chapter

discusses the development of a concrete constitutive tensile model to represent the tensile behavior of concrete. The later step is a critical part in predicting shear cracks in shallow reinforced concrete bean, which is presented in chapter three. An innovative nonlinear numerical approach is derived and applied in this chapter. Chapter four treats the analytical formulation of the shear stress distribution in cracked reinforced concrete flexural members. While chapter five points out the similarity in behavior and nature of the shear-flexural cracking to the concrete crushing failure mode. Chapter six presents the experimental data of a tested beam as well as series of comparisons between the experimental results and the proposed analysis. The study conclusions and recommendation are summarized in chapter seven,

1.4 References

Hognestad, E., (1952) "What Do We Know About Diagonal Tension and Web Reinforcement in Concrete? " University of Illinois Engineering Experiment Station, Circular Series No. 64.

Moody,K.G., Viest, I.M., Elstner, R.c., and Hognestad,E. (1954) "Shear Strength of Reinforced Concrete Beams, Part-1 Tests of Simple Beams ". ACI Journal, proceedings Vol. 51, pp. 317-332.

Morsch, E., (1903) "Versuche Uber Schubspannugen in Betoneisentragern," Beton und Eisen Berlin, Vol. 2, No. 4, pp. 269-274.

Richart, Frank E., and Larson, L.J., (1928) "An Investigation of Web Stresses in Concrete Beams, Part II, Restrained Beams", University of Illinois Engineering Experiment Station, Bulletin 175.

Talbot, A.N., (1908)" A Test of Three Large Reinforced Concrete Beams" University of Illinois Engineering Experiment Station, Bulletin No. 28.

Talbot, A.N., (1909)" Tests of Reinforced Concrete Beams: Resistance to Web Stresses". University of Illinois Engineering Experiment Station, Bulletin No. 30, 1909.

Zwoyer, E.N., and Siess, C.P., (1954) "Ultimate Strength in Shear of Simply-Supported Prestressed Concrete Beams Without Web Reinforcement". ACI Journal, Proceedings Vol. 51, pp. 181-200.

Chapter 2 - Calibrating a New Constitutive Tension Model to Extract a Simplified Nonlinear Sectional Analysis of Reinforced Concrete Beams

A nonlinear analysis for the structural members is vital to understand the behavior and the response of reinforced concrete members. Although most design procedures concentrate on the ultimate stage of response towards the end of the post-yielding zone as the decisive design criterion, the structural members usually function at the service load levels within the post-cracking zone. Therefore, cracking is a critical aspect of concrete behavior that affects the overall response of reinforced concrete beams. The initiation and the propagation of the cracks are affected directly by the tension and shear stresses in the beam. In flexural beams, the tensile stresses dominate the crack onset and its growth. Cracks in reinforced concrete flexural beams create non-cracked regions in between cracked sections. In order to apply a consistent analysis strategy, the smeared crack approach averages the behavior of these different cracked sections and uncracked regions to generate an accurate global response of the entire beam. This study presents a numerical constitutive tensile model that captures the complete tensile response of the reinforced concrete flexural member, in terms of averaged/smeared crack response. As a second step, this model was examined against a large pool of experimental data to validate its accuracy. Overall, the main objective of this study is to develop a representative constitutive tensile model for reinforced concrete flexural members and validate its accuracy against experimental results. The full nonlinear sectional analysis is analytically-realized, based on the assumed trilinear moment-curvature response and the assumed trilinear moment-extreme fiber compressive strain response. This is considered as the secondary outcome of the present study.

2.1 Introduction

The full tensile response of reinforced concrete includes but not limited to plain concrete softening, reinforced concrete stiffening and shrinkage effects. Other parameters might be aggregate size, concrete-steel bond slip mechanism, creep effect and cyclic loading. However, most of the researchers consider the tension stiffening to be the main parameter when describing the reinforced concrete tensile behavior beyond the cracking strain.

Plain concrete tension softening was first presented by Hillerborg et al. (1976) who introduced the softening phenomenon through discrete crack model based on fracture mechanics. A series of analytical approaches were introduced after that based on the smeared crack approach, which is more applicable than the discrete crack approach. In addition, a number of experimental studies were performed for concrete in tensile uniaxial tests.

On the other hand, many researchers proposed empirical functions to estimate the tension stiffening effects. Leonhardt (1977) presented a model for computing the mean strains. Between two cracked sections, the average steel strain over the entire length (ε_{sm}), is less than the bare bar strain (ε_s) which is the strain developed by the steel alone after cracking. The difference between ($\varepsilon_{s)}$ and (ε_{sm}) is referred to as "tension stiffening". Several structural codes followed Leonhardt approach with different parameters like British standards BS 8110-1997 and Eurocode2 (2004).

The second approach is to estimate the tension stiffening effects by assuming a stress-strain profile beyond the cracking point. This profile includes numerical parameters calibrated against the global experimental response of beams or tensile specimens. Scanlon and Murray (1974) were the first to model the tension stiffening in terms of the degraded concrete modulus. Vebo and Ghali (1977) proposed a linear and a bilinear descending curve in their analysis of concrete

slabs. Nayal and Rasheed (2006) adopted a bilinear descending function with a sudden drop of 20% of the cracking strength right at the cracking strain, see Figure 2-1. It is important to note here that all of the earlier tension stiffening models completely degrade the concrete contribution at a multiple of the cracking strain while this parameter seems to be related to the yielding strain of steel.

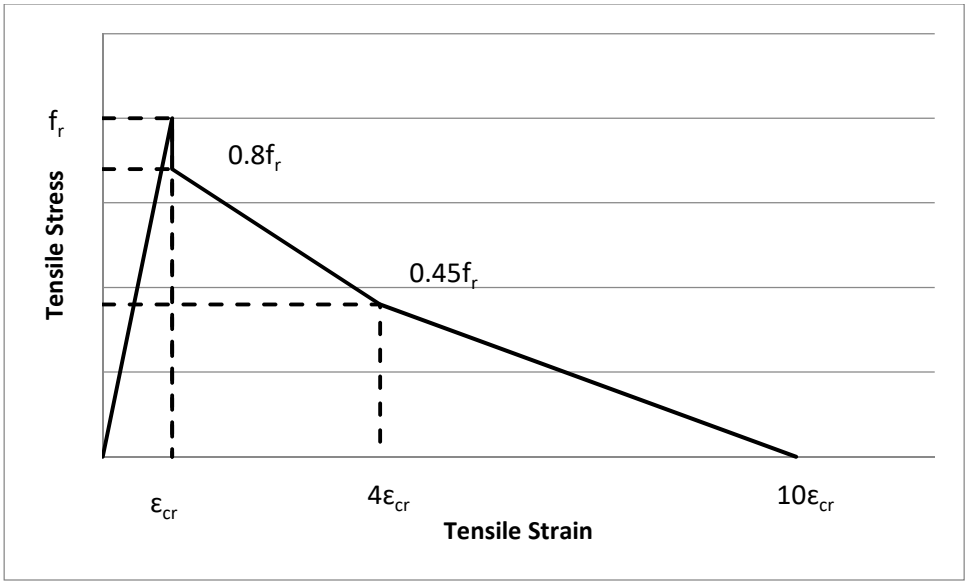

Figure 2-1 Nayal and Rasheed (2006) proposed tension stiffening model

In this study, the second approach to the modeling of the tension stiffening effects is adopted to develop a newly calibrated model composed of a single mathematical expression. The controlling parameters of a natural logarithmic function selected are calibrated based on close agreements between the nonlinear load-deflection response, especially in the post cracking loading range, and the experimental load-deflection response of a set of tested beams. The resulting analysis procedure lends itself to analytical formulation of the entire nonlinear sectional response as presented in this study.

2.2 Flexural Formulation

2.2.1 Constitutive Models Used

The stress-strain relationships for the concrete and the reinforcement steel are assumed to be independent of each other. The axial stress in steel would be only a result of the axial strain in the steel. Also, shear stresses in the steel bars on a plane perpendicular to their longitudinal axis are assumed to be negligible. The steel axial stress-axial strain relationship is idealized by a bilinear function, which is the same intension and compression, see Figure 2-2.

$$\boldsymbol{f_s = E_s \varepsilon_s \leq f_y} \quad \textbf{(2.1)}$$

$$f_s = f_y + E'_s(\varepsilon_s - \varepsilon_y), for\ f_s > f_y \quad (2.2)$$

Where (f_s) is the steel stress corresponding to the axial stress (ε_s), (E_s) is the modulus of elasticity of steel, (f_y) is the yielding strength in steel. The steel is assumed to start hardening once exceeding the yielding strain (f_y) according to equation (2.2).

(E'_s) is the slope of steel hardening line after yielding. It is determined based on an equal area under the strain hardening region in the actual experimental curve and the analytical model. Table 2-1 shows the relationship between the estimated (E'_s) and the corresponding (f_y) as measured by Rasheed (1990).

Table 2-1 The Relationship between the estimated (E's) and the corresponding (f_y)

f_y (ksi)	E'_s / E_s
40-45	0.3-0.7%
45-50	0.7-1.2%
50-63	1.2-2.5%

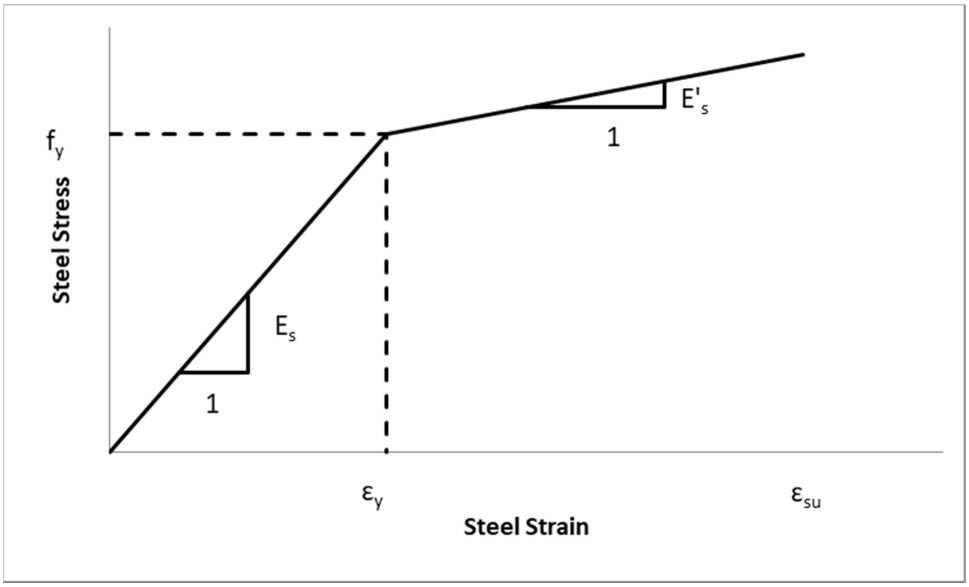

Figure 2-2 Steel stress-strain curve

The concrete stress-strain relationship is assumed to follow the Hognestad's curve, equation (2.3), for compressive stresses (f_c), see Figure 2-3.

$$f_c = f_c' \left(2\frac{\varepsilon_c}{\varepsilon_{c'}} - \left(\frac{\varepsilon_c}{\varepsilon_c'}\right)^2\right) \quad (2.3)$$

A linear relationship with a slope equal to the concrete modulus of elasticity (E_c) up to cracking strain (ε_{cr}) in tension is assumed. This linear relationship is then followed by a descending curve as a function of (ε_{cr}) and the steel yielding strain (ε_y), which will be further developed in the study, see Figure 2-4.

The concrete tensile rupture strength (f_r) is taken as a lower bound value as given in ACI 318-14.

$$f_r = (5 - 7.5)\sqrt{f_c'} \quad (2.4)$$

The rupture strength (f_r) for light weight concrete is simply reduced by 25%. The Factor 5 is taken to account for sections with low compressive steel area to the tensile steel area ratio, which allows for more shrinkage and more residual tensile stresses.

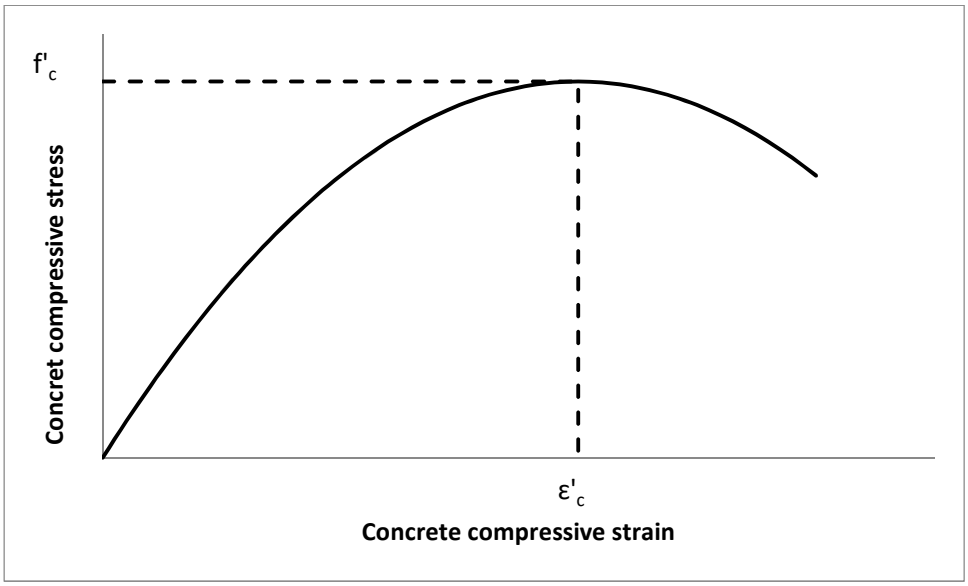

Figure 2-3 Concrete compressive stress-strain curve (Hognestad's Parabola)

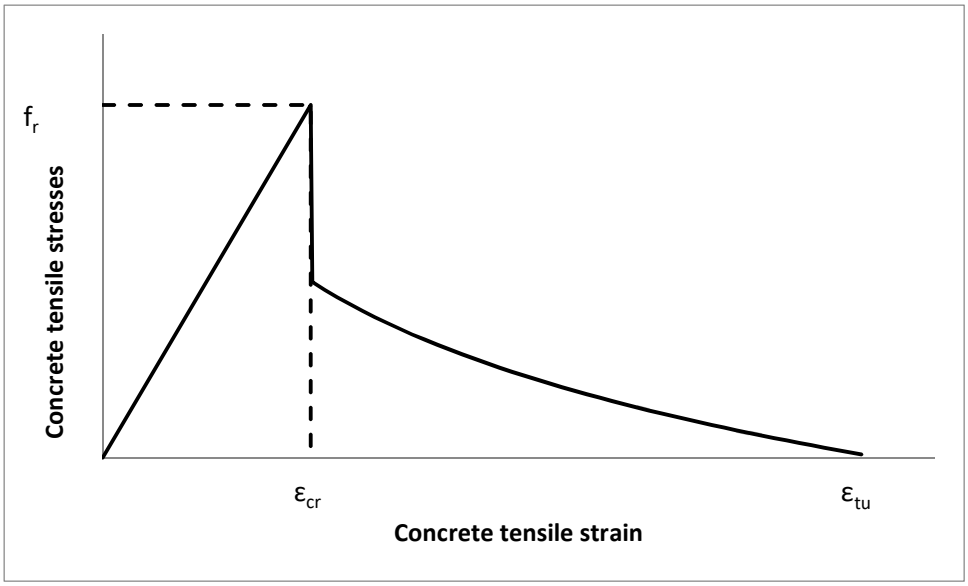

Figure 2-4 Concrete tensile stress-strain curve

2.2.2 Analysis Assumptions

In this study, the following assumptions were made

1. Plane sections before bending remain plane after bending (i.e. linear strain profile across the section depth is assumed before and after cracking).

2. Perfect bond exists between steel bars and the surrounding concrete.

3. Plane sections after bending are assumed to be perpendicular to the mid surface (i.e. shear deformations are negligible).

4. Smeared crack approach (i.e. averaged tensile strains are continuous in concrete in tension).

5. Dowel action effect is neglected.

2.2.3 Flexural Analysis

2.2.3.1 Forces

Compressive Forces

Compressive concrete contribution

By integrating the Hognestad's profile over the area from the neutral axis up to the maximum compressive concrete fiber strain, the concrete compressive force (C_c) is determined for the section based on the following equations

$$C_c = \int_0^C f_c . b \, dy \tag{2.5}$$

$$C_c = f_c' b . \frac{\Phi}{\varepsilon_c'} (c^2 - \frac{\Phi}{3} \frac{C^3}{\varepsilon_c'}) \tag{2.6}$$

Compressive Steel Contribution

The compressive steel force (C_s) is a direct linear relationship with the corresponding steel strain (ε_s') in addition to subtracting the contribution of the concrete in compression occupied by the compression steel bars. This relationship was determined based on the assumption of the bilinear response of steel bars.

behavior for the steel analysis.

$$C_s = A'_s f'_s - A'_s f'_c((2\frac{\varepsilon_s{}'}{\varepsilon_{c'}} - \left(\frac{\varepsilon_s{}'}{\varepsilon_{c'}}\right)^2) \quad (2.7)$$

Where f'_s is computed from equations (2.1)-(2.2) by substituting $\varepsilon_s{}'$ for ε_s.

Tensile Forces

Tensile Concrete contribution

The concrete tensile contribution is divided into two main profiles, Figure 2-4. The first profile is a linear relationship up to the cracking strain (ε_{cr}) with a slope equal to the concrete modulus of elasticity (E_c). This profile leads to a tensile force (T_{c1}) equals to

$$T_{c_1} = \int_0^{d_t} f_t . b \, dy \quad (2.8)$$

$$T_{c_1} = \frac{b f_r^2}{2 E_c \varphi} \quad (2.9)$$

The second profile is a descending curve, which mainly contributes to the total concrete tensile force. This profile is a result of the concrete softening, concrete stiffening due to the steel bond as well as the residual stresses due to shrinkage effect. The tensile force due to this profile (T_{c2}) is calibrated against global experimental response to be a function of the concrete cracking strength and the steel yielding strain. The tensile constitutive model and its calibration against experimental results are presented in section 3 of this study. The equation for (T_{c2}) is presented there.

Tensile steel Contribution

The tensile steel force (T_s) follows the same bilinear behavior based on equations (2.1)-(2.2)

$$T_s = A_s E_s \varepsilon_s - A_s f_{ct}(\varepsilon_s) \, , when \; f_s \leq f_y \quad (2.10)$$

$$T_s = A_s(f_y + E'_s(\varepsilon_s - \varepsilon_y)) - A_s f_{ct}(\varepsilon_s), when \; f_s > f_y \quad (2.11)$$

Where $f_{ct}(\varepsilon_s)$ is taken from the uncracked or post-cracked parts of the concrete tensile constitutive functions. Note that $f_{ct}(\varepsilon_s) = 0, when\ \varepsilon_s \geq \varepsilon_{tu}$.

2.2.3.2 Moments

Compressive concrete contribution

The point of application of concrete compressive force is measured from the extreme compressive fiber (ɣ.c) based on the centroid location of the area under the Hognestad's parabola.

$$\gamma = 1 - \frac{\int_0^{\varepsilon_{cf}} \varepsilon_c . f_c . d\varepsilon_c}{\varepsilon_{cf} \int_0^{\varepsilon_{cf}} f_c . d\varepsilon_c} = \frac{\frac{1}{3} - \frac{\varepsilon_{cf}}{12 f'_c}}{1 - \frac{\varepsilon_{cf}}{3\varepsilon'_c}} \quad (2.12)$$

$$M_{cc} = (c - \gamma . c) * C_c \quad (2.13)$$

Where (c) is the depth of the compression zone to the position of neutral axis and (ɣ) is the ratio of the centroid depth to the neutral axis depth, both measured from the top compression fiber.

Compressive Steel Contribution

The compression steel moment is calculated according to the following equation

$$M_{cs} = C_s(c - d') \quad (2.14)$$

Tensile Concrete contribution

(M_{tc1}) is the moment induced due to the concrete contribution up to the cracking point. While (M_{tc2}) is the moment induced due to the descending constitutive tensile model.

$$M_{tc1} = T_{c1} . \frac{2}{3} \frac{f_r}{E_c . \varphi} \quad (2.15)$$

The equation for (M_{tc2}) is presented in section 3 of this study.

Tensile steel Contribution

The contribution of the moment induced due to the steel reinforcement at any stage of loading is determined as follows

$$M_{ts} = T_s(d - c) \quad (2.16)$$

Where, the tension force of steel is defined according to equations (2.10)-(2.11).

2.2.4 Numerical Moment-Curvature Calculations

A numerical procedure was followed to generate the moment-curvature curve. In this procedure, the maximum compressive fiber strain value (ε_{cf}) was gradually increased until reaching the concrete crushing strain of (0.003). In order to accurately calculate the strain profile under each step value of ε_{cf}, the correct depth of the compression zone (c) was necessary to define the strain profile and the corresponding stress profile and forces/moments. The sectional force equilibrium equation was then applied to validate the depth of the compression zone (c) by iterating for the correct depth of compression zone that makes the summation of forces equal to zero, equilibrium is maintained, see Figure 2-5.

$$\varphi = \frac{\varepsilon_{cf}}{c} \quad (2.17)$$

$$\varepsilon_s = \varphi(d - c) \quad (2.18)$$

$$\varepsilon_s{}' = \varphi(c - d') \quad (2.19)$$

$$\varepsilon_{sf} = \varphi(h - c) \quad (2.20)$$

The summation of moments due to concrete and steel contributions then yielded the total applied moment of the section corresponding to the curvature in equation (2.17), and the numerical moment-curvature curve was then generated for the entire range of extreme compressive fiber strains.

2.2.5 Numerical Load-Deflection Calculations

The numerical nonlinear load–deflection solution of the beams is formulated using the moment-area integration. Half the span of the beam was divided into a number of segments and the

flexural rigidity was calculated at the middle of each segment. The mid-span deflection for symmetric four-point bending loading protocol was then calculated by performing numerical integration of the moment of curvature along the half span of the beam. The numerical integration was expressed as a summation of the analytical contribution of each segment as follow

$$\Delta\ at\ midspan = \int_0^{L/2} x.\phi(x).dx = \sum_0^{N_s}[\frac{P}{2EI_{si}}\left(\frac{x_{i+0.5}^3 - x_{i-0.5}^3}{3}\right)] + \frac{PL_a}{2EI_{si}}\frac{\left(\frac{L}{2}\right)^2 - (L_a)^2}{2} \qquad (2.21)$$

Where, (N_s) is the number of segments along the shear span (L_a), (P) is the total load applied on the beam, ($x_{i+0.5}$) and ($_{xi-0.5}$) are the distances from the support to the end and the beginning of each segment, respectively, and EI_{si} is the secant or effective flexural rigidity of the segment mid-section defined as

$$EI_{si} = \frac{M_i}{\emptyset_i} \qquad (2.22)$$

Figure 2-5 presents the flow chart of the progressive moment-curvature calculation procedure along with the integrated load-deflection point corresponsing to each maximum moment-curvature value. Figure 2-5 is limited to the post-cracking region up to steel yielding. However, the same procedure may be followed to generate the response of the post-yielding region.

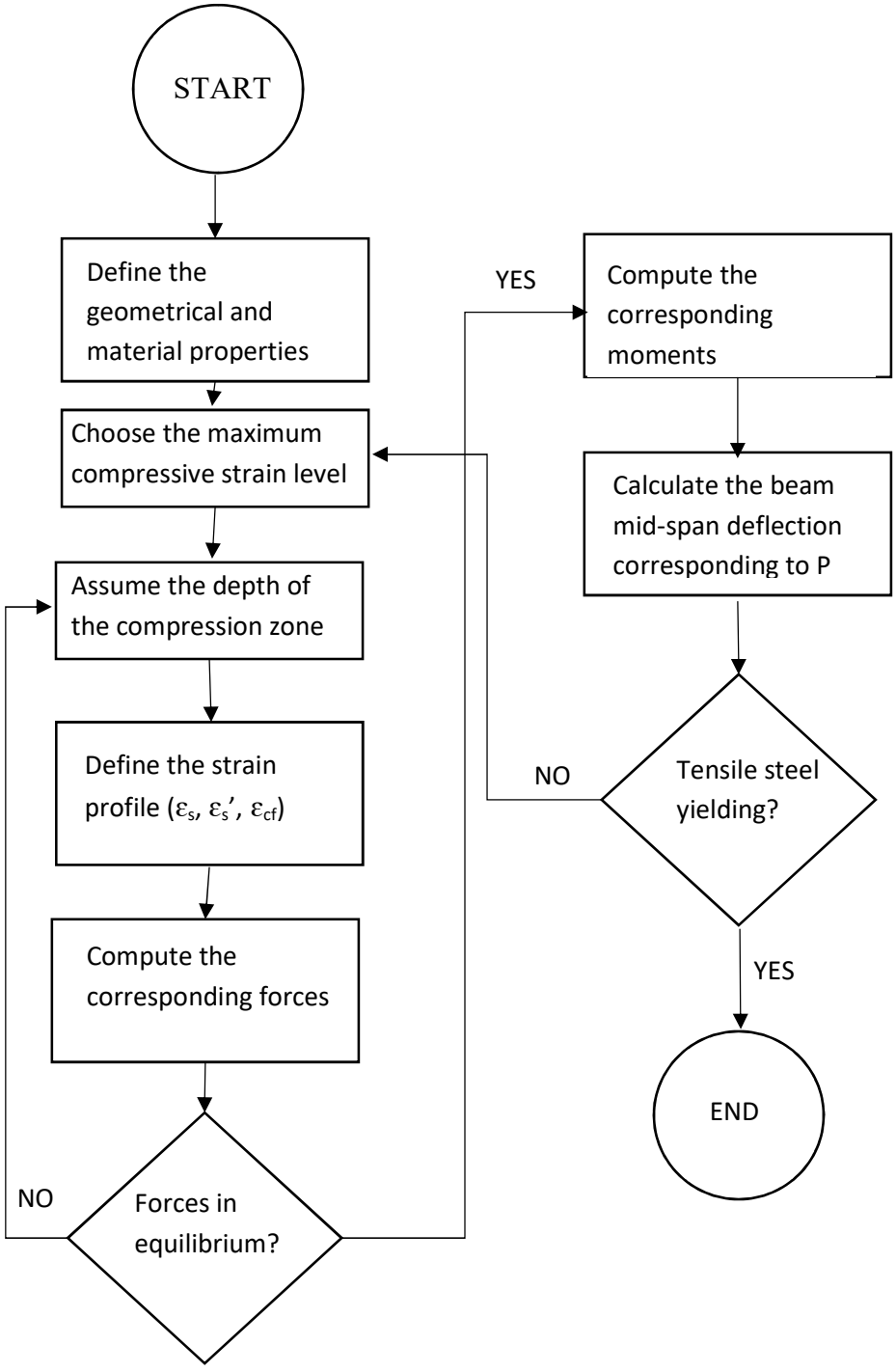

Figure 2-5 Flexural analysis flow chart up to yielding point

2.3 Constitutive tension model

The proposed model in this study is based on cycles of numerical analysis and material model adjustments until convergence to the experimental response. A descending model was critical to represent the gradual loss of stiffness with the propagation of the beam cracks. This model represents the contribution of concrete in tension between two successive cracked sections. This approach is known as the smeared crack approach, which simulates the global response of the element. Hence, this response could be understood as an averaged behavior for all the beam sections. Therefore, the tension model may be a function of the structural element and the loading patterns considered. A uniaxial plain concrete element would show a different behavior than a reinforced concrete flexural beam due to the steel-concrete bond in the latter. Similarly, a reinforced concrete shear beam with a smaller shear span to beam depth ratio would act differently than a flexural beam due to the effect of the concrete shear deformation.

The presented constitutive tension model for reinforced concrete flexural beams is a summation of various reinforced concrete features. Plain concrete softening and steel tension stiffening are considered the main phenomena to develop the constitutive model. Hillerborg et al. (1976) were the first to describe tension softening, which occurs due to the development of concrete flexural cracks. The fracture energy, transformed from the strain energy, advances existing major cracks and initiates minor micro cracks, which weaken the concrete at relatively high rates. Steel-Reinforced concrete tension stiffening is the second important characteristic that represents the local bond-slip between the concrete and the steel bars. This feature causes the tensile stresses in the concrete to gradually reduce in between two successive primary cracks. Tension softening and Tension stiffening are usually referred to as the main parameters responsible of post-cracked concrete tensile behavior. However, shrinkage and aggregate size also participates in

altering the concrete tensile behavior. Shrinkage builds up residual stresses in the concrete while hardening. This results in lowering the tensile strength and tension stiffening effects. On the other hand, the aggregate size/shape effects are mainly observed when shear and tensile stresses are combined. Therefore, a numerical constitutive tension model based on calibrating the global experimental response is important to capture all these characteristics in one model.

The proposed constitutive concrete tensile model relates the tensile strain (ε_t) with the tensile concrete stresses (f_t) as a function of the material parameters calibrated based on experiments for flexural reinforced concrete beams. The model is presented as a function of concrete cracking and steel yielding parameters, Equation 2.23. Stress and strain constants in the equation were extracted by actively matching the analysis to a large pool of four points bending tests on flexural beams.

$$\frac{f_t}{0.5f_r} = 1 - \frac{1}{\ln(\frac{1.4\varepsilon_y}{\varepsilon_{cr}})} \ln\left(\frac{\varepsilon_t}{\varepsilon_{cr}}\right) \tag{2.23}$$

This proposed descending function on the domain ($\varepsilon_{cr} \leq \varepsilon_t \leq 1.4\varepsilon_y$) shows a sudden drop to (0.5 f_r) at the cracking strain (ε_{cr}) upon strain to fracture energy conversion and continues to descend till zero when the tensile strain reaches (1.4 ε_y), see Figure 2-6. The sudden drop in stress at cracking is a function of the tension softening effect while the exhaustion of the tension stiffening effect is expected to be related steel yielding.

The axial force due to the proposed constitutive tensile model (T_{c2}) is the integral of the given stress profile over the distance from the cracking depth $d_{cr} = \frac{f_r}{E_c\varphi}$ to the end of the model at $\frac{1.4\varepsilon_y}{\varphi}$ or the full tensile depth of the section, Equation (2.24).

$$T_{c_2} = \int_{d_{cr}=\frac{f_r}{E_c\varphi}}^{\hat{d}} f_t . b \, dy \tag{2.24}$$

Where $\hat{d}$ is the end of the proposed model at $\frac{1.4\varepsilon_y}{\varphi}$ or the full tensile depth of the section $(h-c)$.

$$T_{c_2} = \int_{d_{cr}=\frac{f_r}{E_c\varphi}}^{\hat{d}} (0.5f_r - \frac{0.5f_r}{\ln\left(\frac{1.4\varepsilon_y}{\varepsilon_{cr}}\right)} ln\left(\frac{\varepsilon_t}{\varepsilon_{cr}}\right)) b\, dy \quad (2.25)$$

Let, $k = \frac{0.5f_r}{\ln\left(\frac{1.4\varepsilon_y}{\varepsilon_{cr}}\right)}$ (2.26)

$$T_{c_2} = b((0.5f_r + kln(\varepsilon_{cr}) + 1)y - kyln(\varphi) - kyln(y))\Big|_{d_{cr}=\frac{f_r}{E_c\varphi}}^{\hat{d}} \quad (2.27)$$

The moment induced due to the proposed constitutive tensile model (M_{tc2}) is calculated as follow

$$M_{tc2} = \int_{d_{cr}=\frac{f_r}{E_c\varphi}}^{\hat{d}} f_t.b.y.dy \quad (2.28)$$

$$M_{tc2} = b(\frac{y^2}{2}\left(0.5f_r + kln(\varepsilon_{cr}) + \frac{k}{2}\right) - k\frac{y^2}{2}ln(\varphi) - k\frac{y^2}{2}ln(y))\Big|_{d_{cr}=\frac{f_r}{E_c\varphi}}^{\hat{d}} \quad (2.29)$$

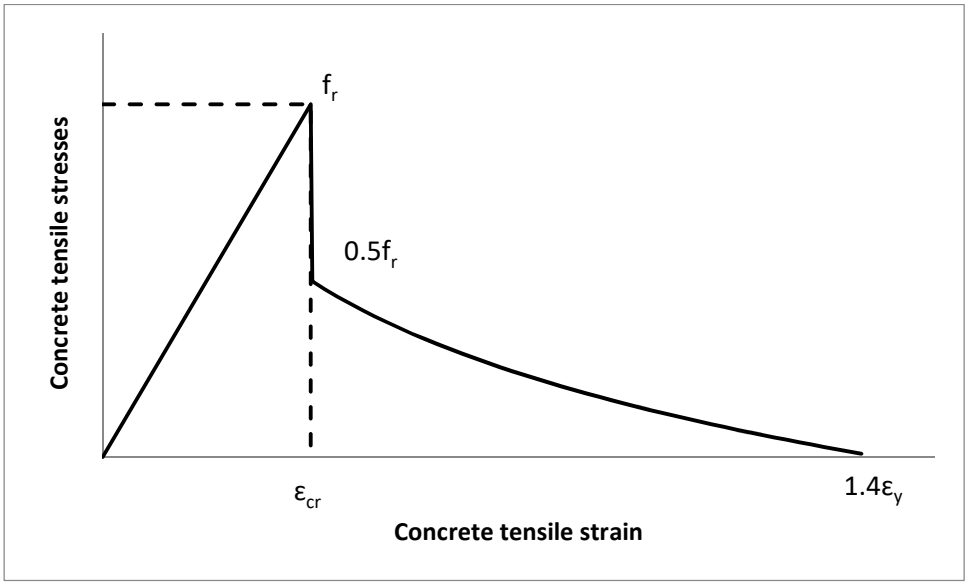

Figure 2-6 Suggested concrete constitutive tensile model

2.4 Results

The reinforced concrete beam tests collected in this study cover a big range of geometrical and material parameters. Normal weight concrete and lightweight concrete were covered in the database, the maximum compressive concrete strength range is 27.5-83 MPa (4-12 ksi). The steel yielding strength range is 344.75-551.6 MPa (50-80 ksi). Singly and doubly reinforced sections with different ratios are included for representative comparisons. A wide range of steel ratios is examined to confirm the applicability of the model, see tables 2-2 and 2-3.

Table 2-2 The geometrical parameters for the tested beams

Number	Reference	h(mm)	b(mm)	d(mm)	cc(mm)	d'(mm)	L/2(mm)	La(mm)
1	Tavares et al. 2008	299.72	149.86	269.24	29.97	27.94	1447.80	939.80
2	Arduini et al. 1997	398.78	299.72	349.76	25.40	49.78	1249.98	1100.07
3	Spadea et al. 1998	299.97	139.95	262.99	37.08	36.83	2400.00	1800.10
4	Ahmad and Baker 1991 LR8-22	304.80	152.40	258.83	45.97	0.00	1727.20	1498.60
5	Ahmad and Baker 1991 LR8-51	304.80	152.40	258.83	45.97	0.00	1727.20	1498.60
6	Ahmad and Baker 1991 LR11-24	304.80	152.40	257.30	47.50	0.00	1727.20	1498.60
7	Ahmad and Baker 1991 LR11-54	304.80	152.40	228.60	76.20	0.00	1727.20	1498.60
8	Ahmad and Batts 1991 LJ 8-44	304.80	152.40	225.55	79.25	53.34	1727.20	1498.60
9	Ahmad and Batts 1991 LJ 11-22	304.80	152.40	250.95	53.85	50.80	1727.20	1498.60
10	Ahmad and Batts 1991 LJ 11-47	304.80	152.40	222.25	82.55	53.34	1727.20	1498.60

Table 2-3 The material parameters for the tested beams

Number	f'_c (MPa)	f_y(MPa)	E_s(MPa)	E_c(MPa)	f_r(MPa)	ε_{cr}	ρ_s	ρ_s'
1	44.0	539.9	200,000	21723.1	3.3	0.00015	0.0061	0.0016
2	30.0	339.9	200,000	25994.2	1.9	0.00007	0.0037	0.0025
3	30.0	434.4	200,000	25921.1	2.3	0.00009	0.0109	0.0109
4	59.0	413.7	200,000	25925.2	2.4	0.00008	0.0101	0
5	60.5	413.7	200,000	25925.2	2.4	0.00008	0.0226	0
6	79.7	413.7	200,000	30407.0	2.8	0.00009	0.0145	0
7	79.9	413.7	200,000	32889.2	2.8	0.00008	0.0326	0
8	57.6	413.7	200,000	29705.0	2.3	0.00008	0.0233	0.0116
9	80.9	413.7	200,000	35201.5	2.8	0.00008	0.0148	0.0067
10	76.3	413.7	200,000	34166.8	2.7	0.00008	0.0335	0.0168

The common factors between these beams are 1) they are all flexural beams, 2) they were tested in four points bending to match the goal of this study and 3) they have comparable section height and width while varying the tensile steel area. Each beam was analyzed using the proposed model, then the load-deflection graph was generated and compared against the actual experimental response of the beam, (e.g. see Figure 2-7). In addition, the moment-curvature graph and the moment-maximum compressive strain graph were developed to confirm the accuracy of the trilinear moment-curvature approximated behavior, (e.g. see Figures 2-8 and2-9).

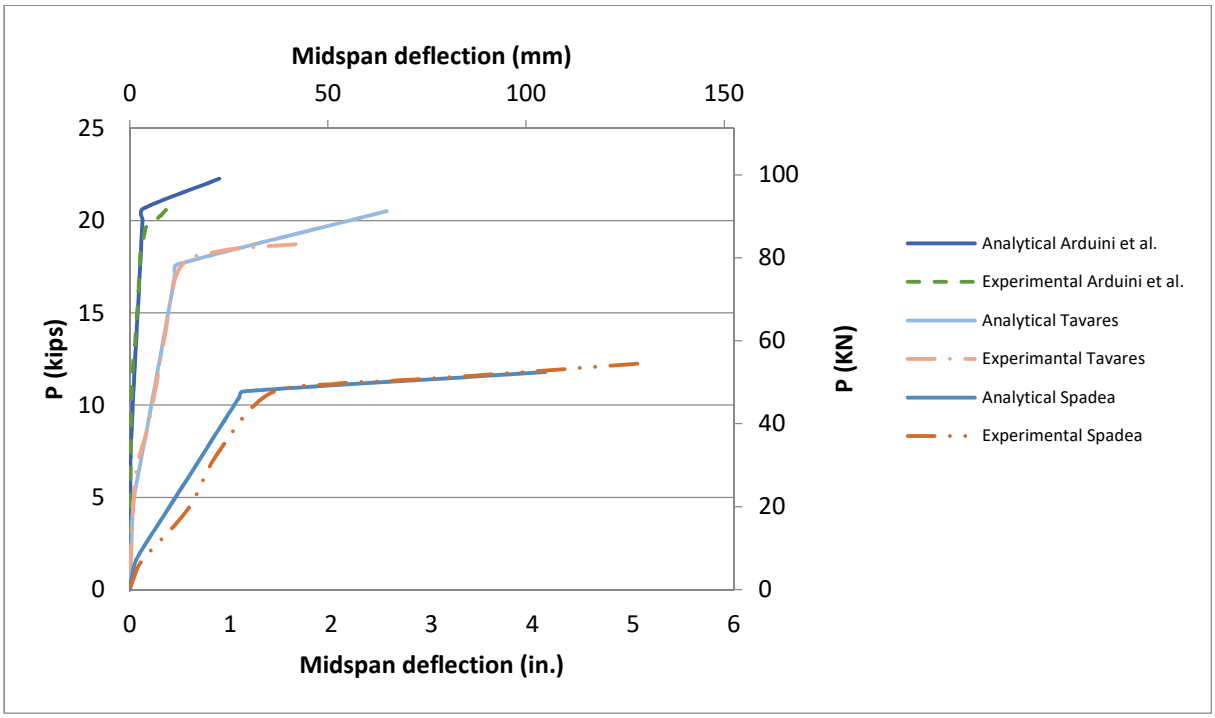

Figure 2-7 Arduini et al. (1997), Tavares et al. (2008) and Spadea et. Al. (1998) load vs. midspan deflection comparisons

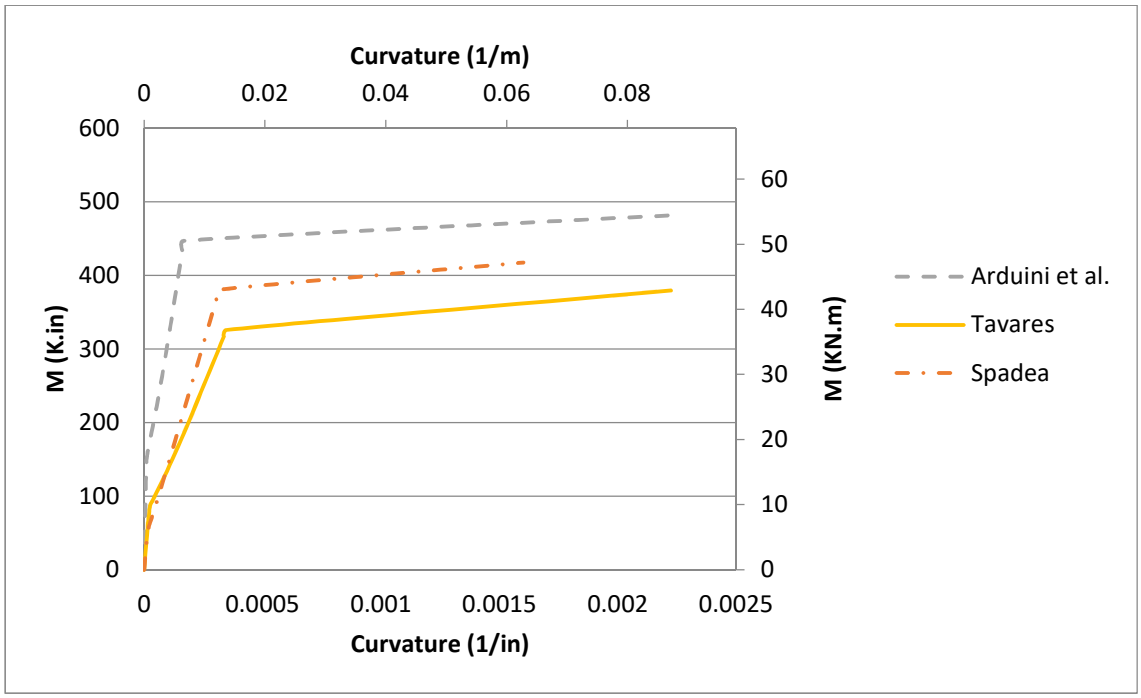

Figure 2-8 Arduini et al. (1997), Tavares et al. (2008) and Spadea et. Al. (1998) moment vs. curvature analytical graphs

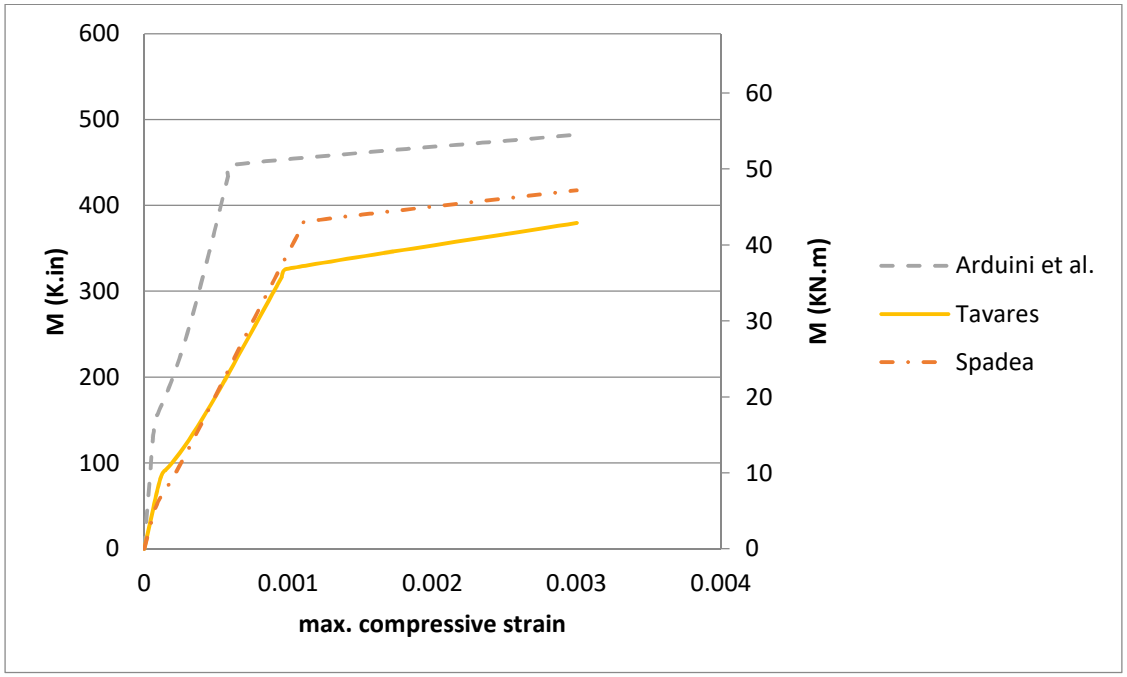

Figure 2-9 Arduini et al. (1997), Tavares et al. (2008) and Spadea et. Al. (1998) moment vs. maximum compressive strain analytical graphs

The proposed analysis was performed for Tavares et al. (2008), Arduini et al. (1997) and Spadea et al. (1998). The geometric and material parameters of these beams are listed in Table 2-2 and 2-3. Excellent agreements were observed against Tavares et al. (2008), Arduini et al. (1997) and Spadea et. Al. (1998) experimental results, see Figure 2-7. The trilinear analysis for Moment-curvature behavior and Moment-Maximum compressive strain behavior was confirmed for the three experimental beams.

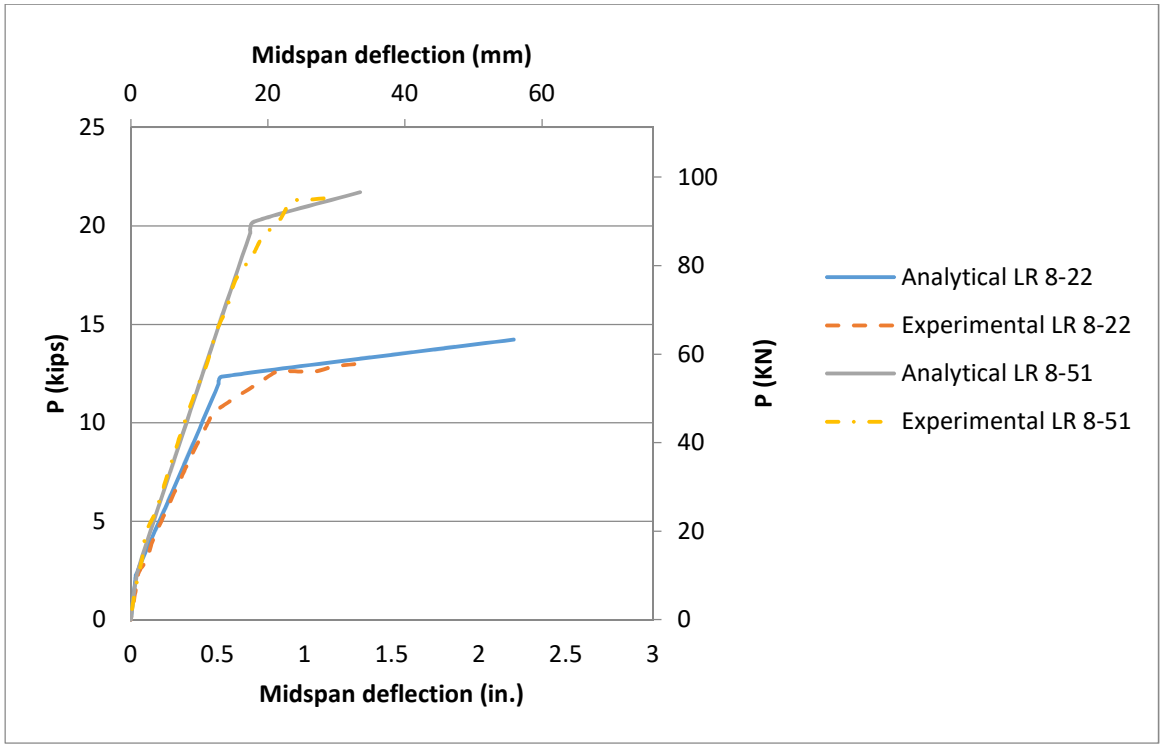

Figure 2-10 Ahmad and Baker (1991) load vs. midspan deflection comparisons

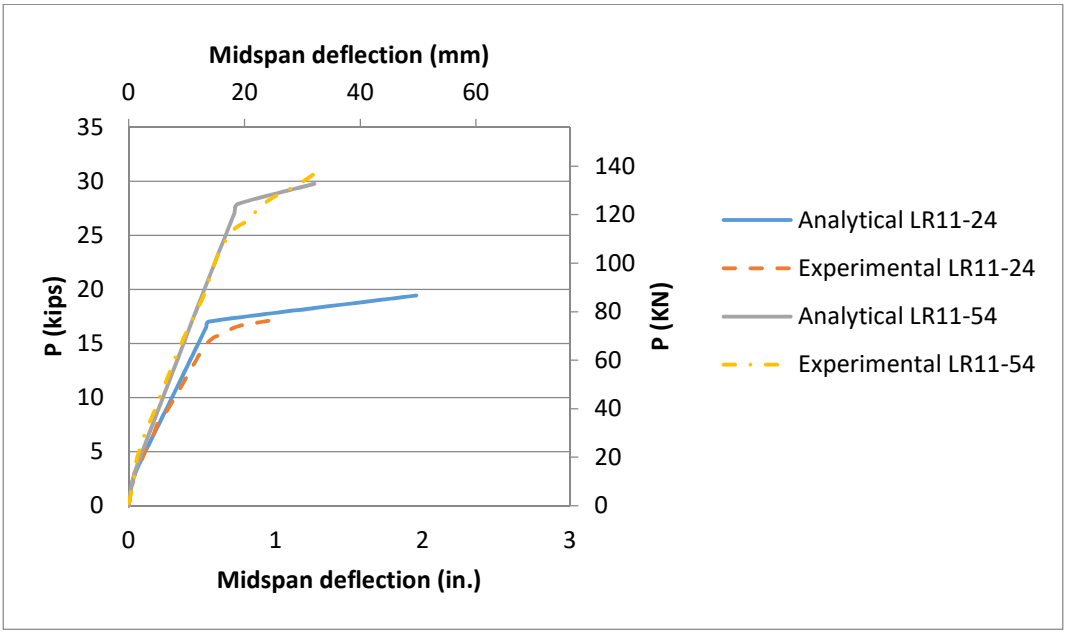

Figure 2-11 Ahmad and Baker (1991) load vs. midspan deflection comparisons

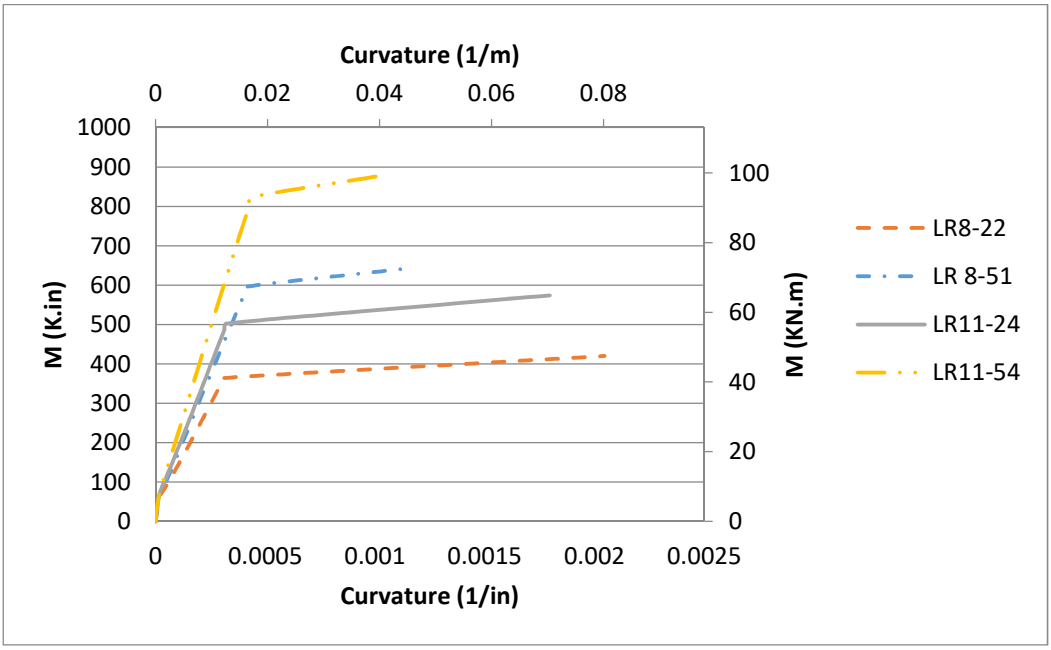

Figure 2-12 Ahmad and Baker (1991) moment vs. curvature analytical graphs

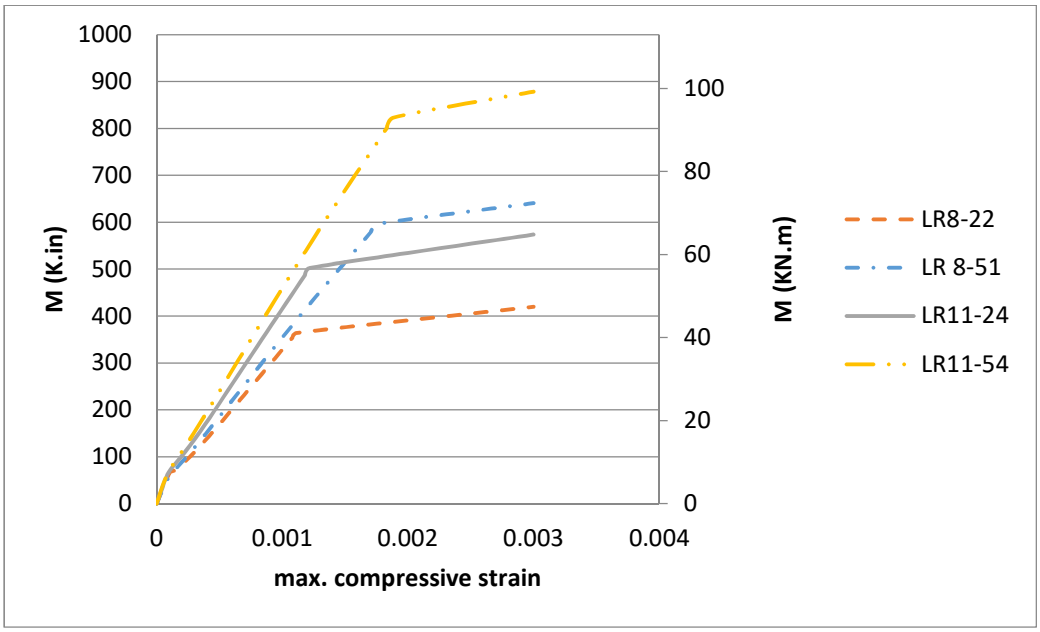

Figure 2-13 Ahmad and Baker (1991) moment vs. maximum compressive strain analytical graphs

The four beams tested by Ahmed and Baker (1991) were analyzed here. All four beams have the same cross section 304.8 mm*152.4mm (12 inx6 in) and the same clear span of 3.45 m (136 in). The beams were singly reinforced with (ρs=.0101, .0226, .0145, .0326) and high strength light weight concrete of 59.3, 59.3, 80, 80 MPa (f'_c=8.6, 8.6, 11.6, 11.6) ksi respectively for LR8-22, LR8-51, LR11-24 and LR11-54. Excellent matches were observed against the experimental analysis for all four beams, Figures 2-10 and 2-11. For all four beams the Trilinear behavior for the precracking, post cracking and post yielding zones was fully confirmed for the moment-curvature and moment-maximum compressive strain, see Figures 2-12 and 2-13.

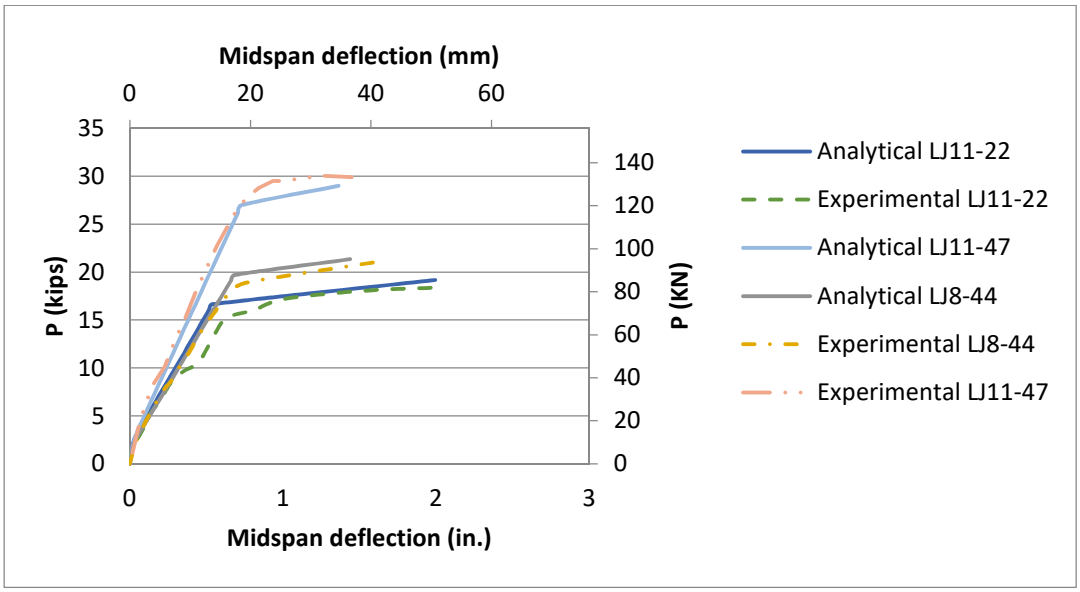

Figure 2-14 Ahmad and Batts (1991) load vs. midspan deflection comparisons

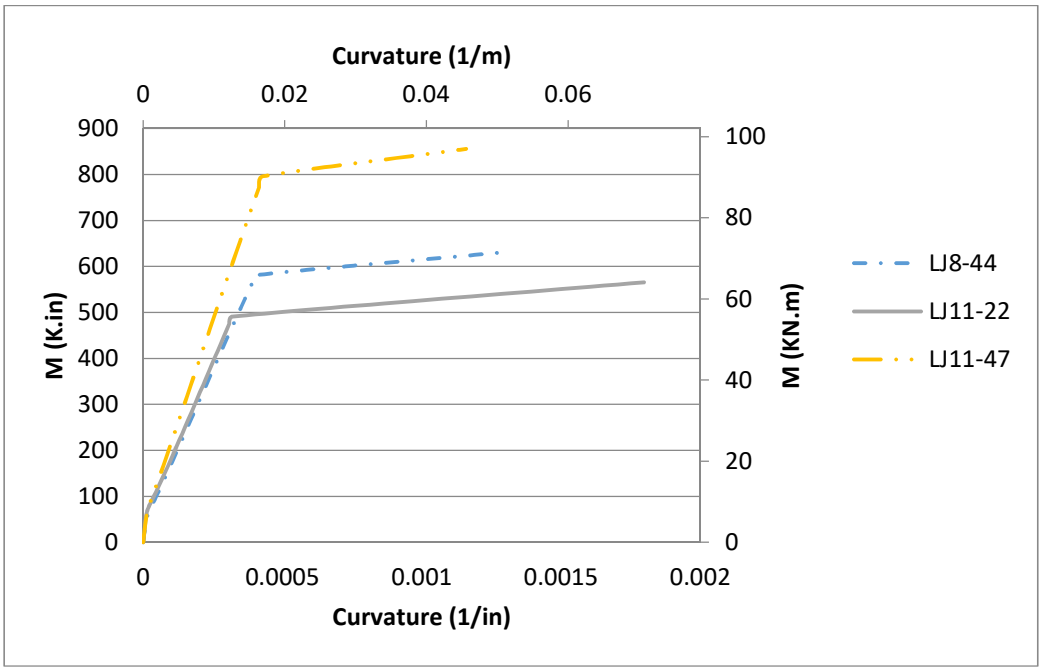

Figure 2-15 Ahmad and Batts (1991) moment vs. curvature analytical graphs

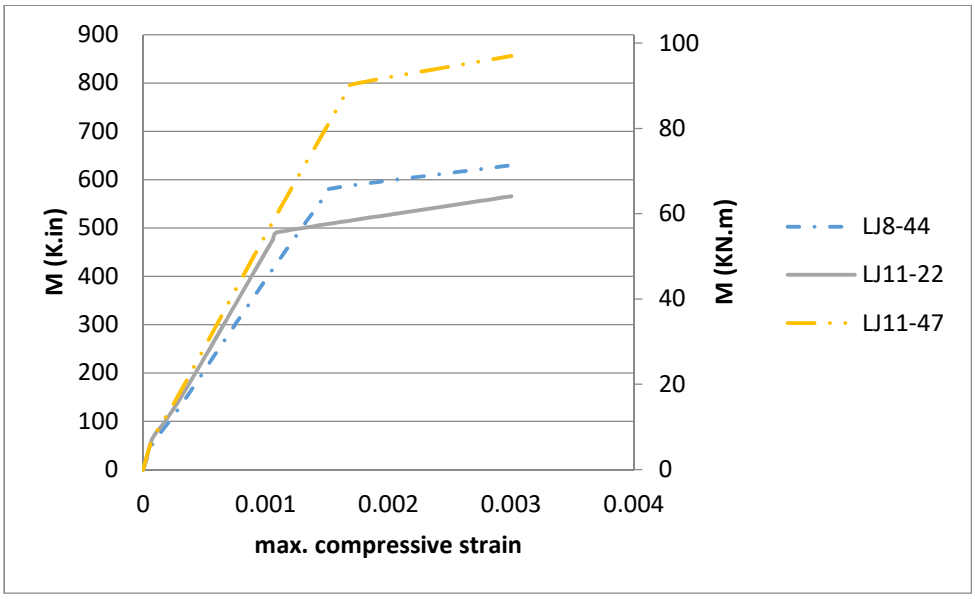

Figure 2-16 Ahmad and Batts (1991) moment vs. maximum compressive strain analytical graphs

The last three analyzed beams were tested by Ahmad and Batts (1991). All three beams have the same cross section 304.8 mm*152.4mm (12in*6in) and the same clear span of 136 in. The tested beams were doubly reinforced, see table 2-3 .Light weight high strength concrete was used for all three beams. Excellent matches were obtained against the experimental results for all three beams at the pre-cracking, post-cracking and post-yielding zones. LJ11-22 showed a sudden change of stiffness in the post cracking zone which generally indicates the development of shear cracks. For all three beams the trilinear behavior for the pre-cracking, post-cracking and post-yielding zones was fully confirmed for the moment-curvature and moment-maximum compressive strain.

2.4.1 Simplified Non-linear Sectional and Beam Analysis

All previous comparisons showed a good agreement with the experimental data in terms of the global response of the beam load vs mid-span deflection. In this section, a detailed comparison

is presented against Decker (2007) and Almusallam (1997) experimental work. Decker reported the global and sectional responses in his work. The sectional response was obtained by locating strain gauges at the tensile steel level and the top surface of the beam, which allowed for a full strain profile development. Unfortunately, Decker (2007) reported the failure of the strain gauges in the post-yielding zone. The beams were simply supported and were tested in four-points bending. The supports were placed 3 inches from the edge of the beam, providing a clear span of 4.72 m (15.5 ft). Tables 2-4 and 2-5 show the geometrical and material properties of the beam. Similarily, Almusallam (1997) reported the experimental load-deflection and the experimental moment-curvature curves. Tables 2-6 and 2-7 show the geometrical and material properties of the analyzed beams.

Table 2-4 The geometrical parameters for Decker (2007) beam

h (mm)	b(mm)	d(mm)	cc(mm)	d'(mm)	L/2(mm)	L_a(mm)
304.8	152.4	261.87	25.4	39.62	2362.2	1752.6

Table 2-5 The material parameters for Decker (2007) beam

f'_c (MPa)	f_y(MPa)	E_s(MPa)	E_c(MPa)	n	f_r(MPa)	ε'_c	ρ_s	ρ_s'
34.5	475.8	200,000	27794.4	7.20	3.65	0.00212	0.0100	0.0036

Table 2-6 The geometrical parameters for Almusallam (1997) beam

h (mm)	b(mm)	d(mm)	cc(mm)	d'(mm)	L/2(mm)	La(mm)
209.80	199.90	159.99	25.40	43.18	1350.01	1249.68

Table 2-7 The material parameters for Almusallam (1997) beam

f'_c (ksi)	f_y(ksi)	Es(ksi)	E_c(ksi)	n	f_r(ksi)	ε'c	ρ_s	ρ_s'
4.54	80.19	29000.00	3840.63	7.55	0.337	0.002	0.0138	0.0009

The analysis, of these two extra beams, was performed as described to obtain the load-mid span deflection graphs and the load-tensile steel strain curve as well as the moment-curvature and the moment-maximum compressive strain curves. This comparison was necessary to illustrate that the presented constitutive model matches not only the global response of the beam but also it matches the sectional local response.

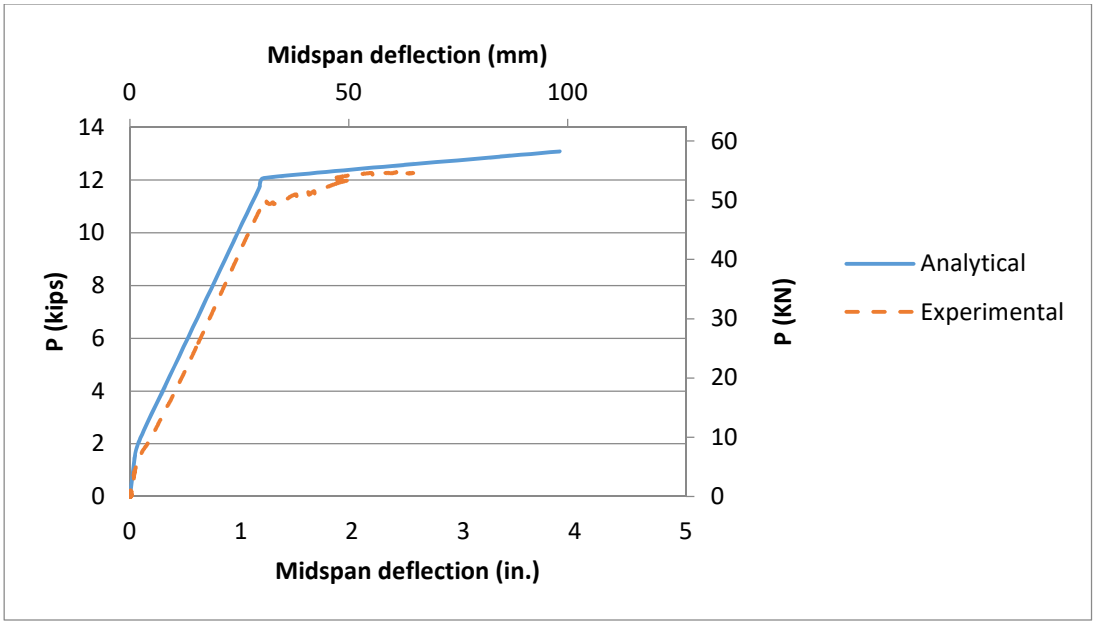

Figure 2-17 Decker (2007) load vs. midspan deflection comparisons

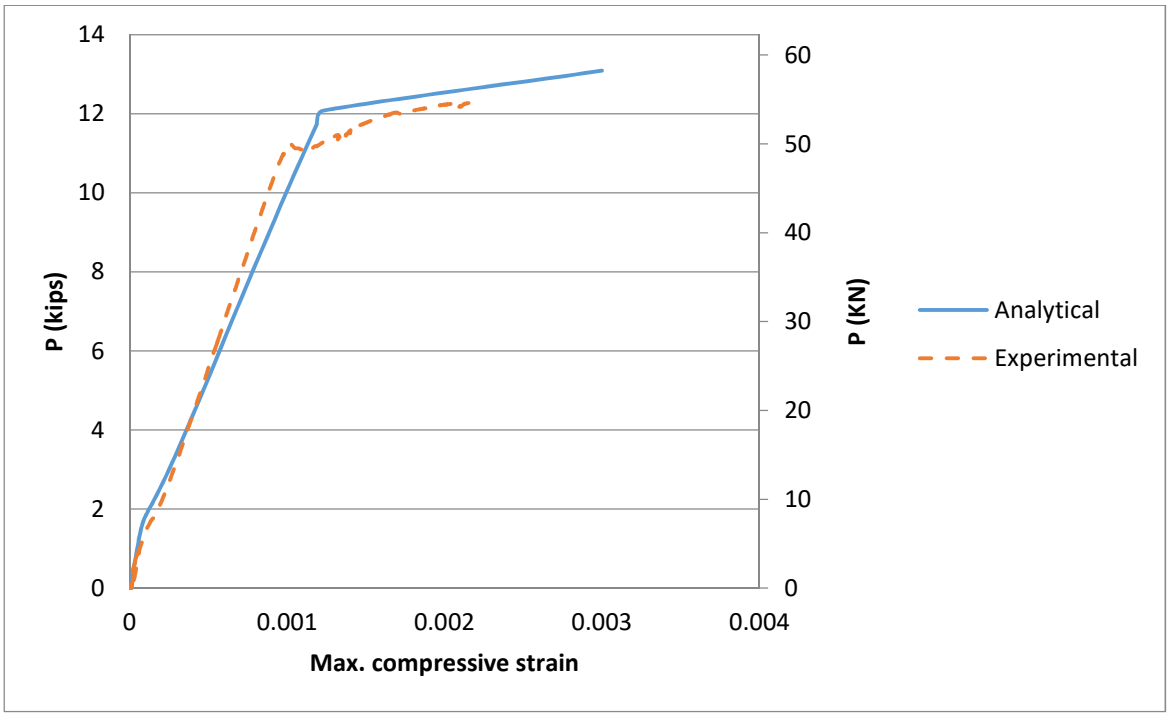

Figure 2-18 Decker (2007) load vs. maximum compressive strain comparison

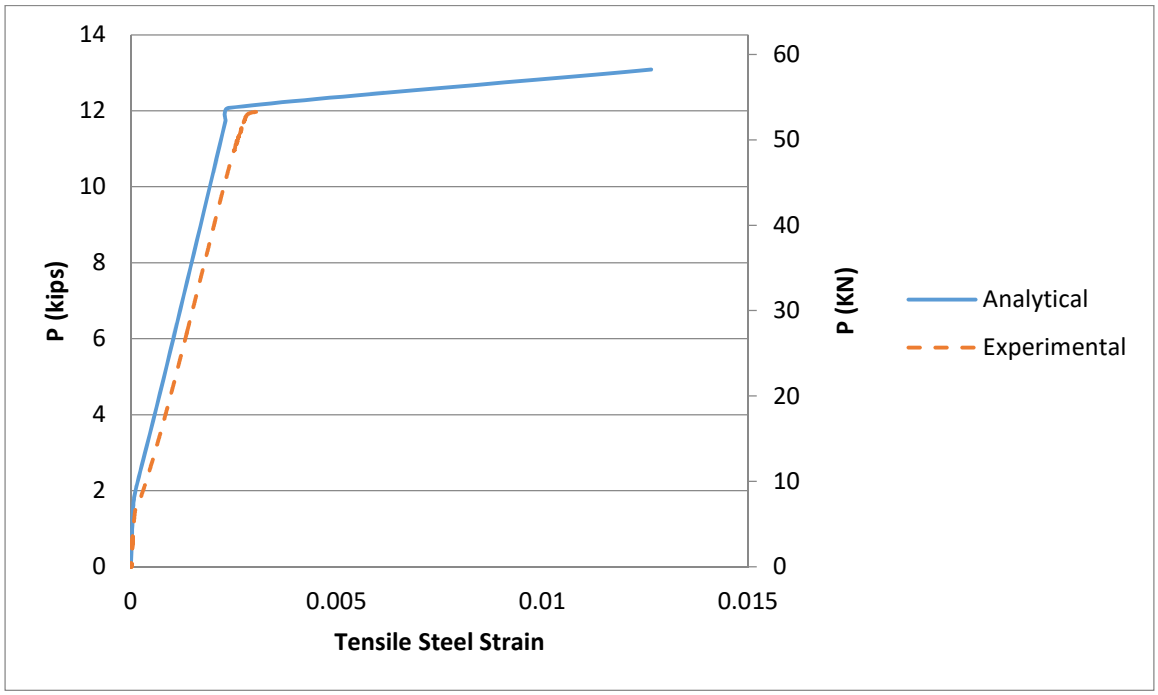

Figure 2-19 Decker (2007) load vs. tensile steel strain comparison

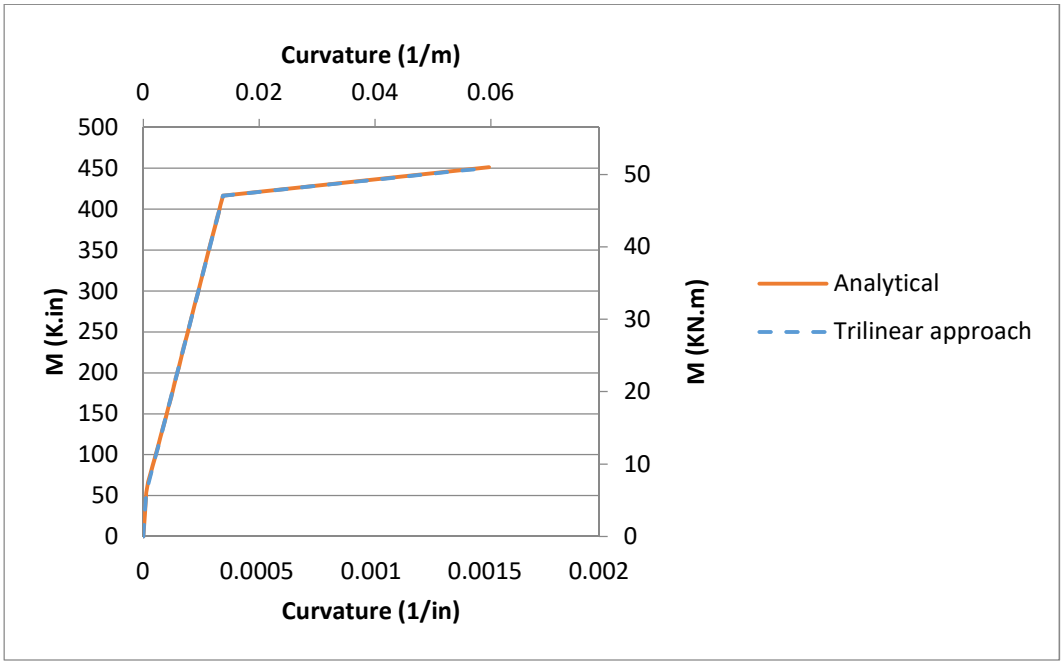

Figure 2-20 Decker (2007) moment vs. curvature analytical graphs

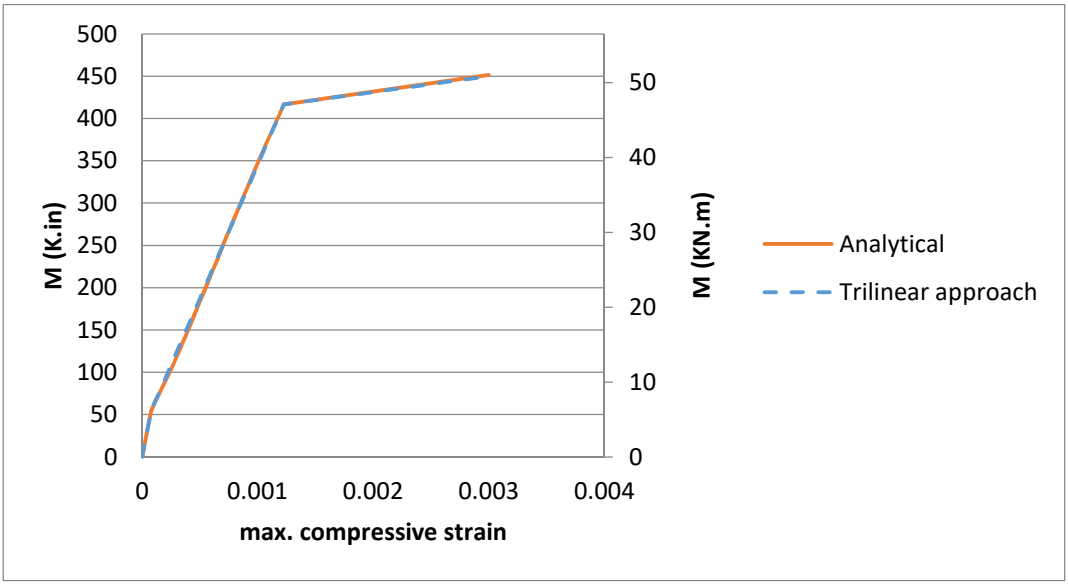

Figure 2-21 Decker (2007) moment vs. maximum compressive strain analytical graphs

Decker (2007) tested a full-scale rectangular beam with a cross section of 304.8 mm*152.4mm (12in*6in) and a clear span of 4.72 m (186 in). A good agreement between the experimental and the analytical Load-Deflection is shown in Figure 2-17. This agreement confirms the accuracy

of the proposed model against the global behavior of the beam. However, it is important to validate the constitutive tensile model against the local sectional response. Figure 2-18 and 2-19 show Load vs. Maximum compressive strain and load vs. tensile steel strain. Excellent agreements between the analytical and the experimental results were observed for the two comparisons. Furthermore, Figures 2-20 and 2-21 confirm the trilinear behavior of the Moment-Curvature and Moment-Maximum compressive strain graphs.

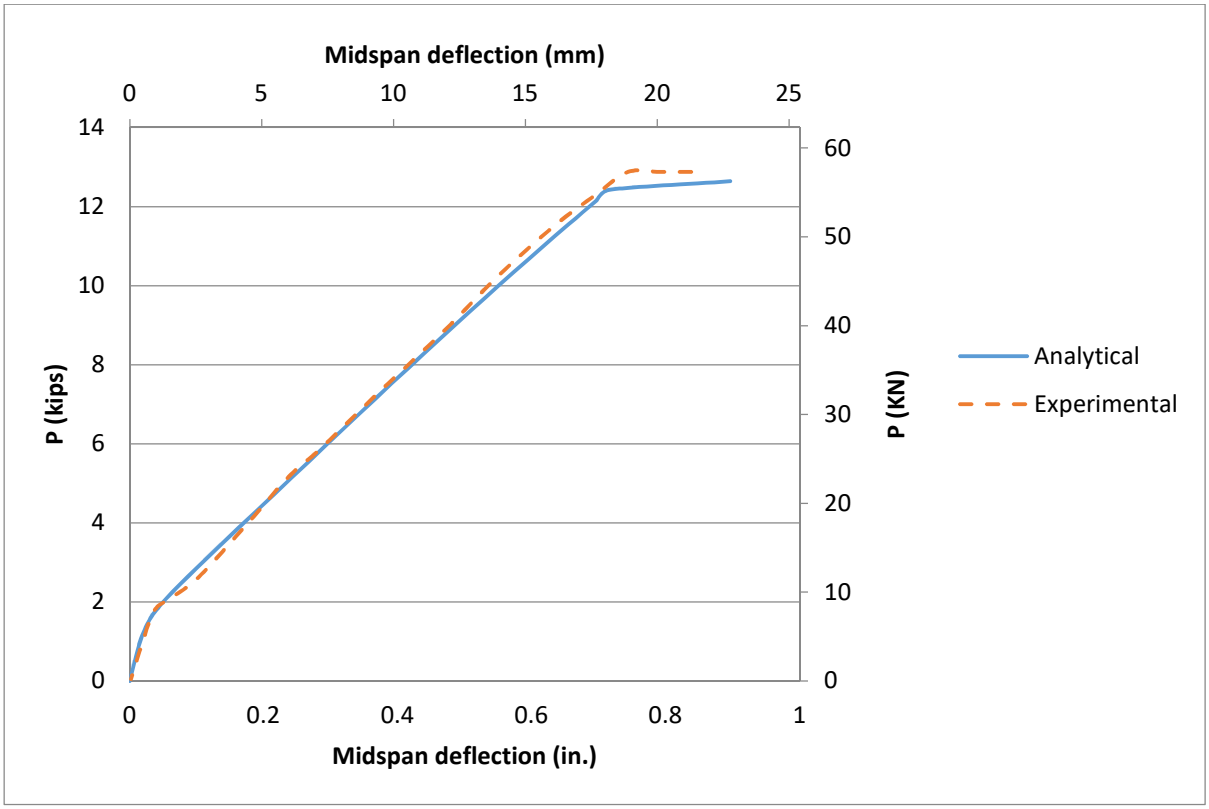

Figure 2-22 Almusallam (1997) load vs. midspan deflection comparisons

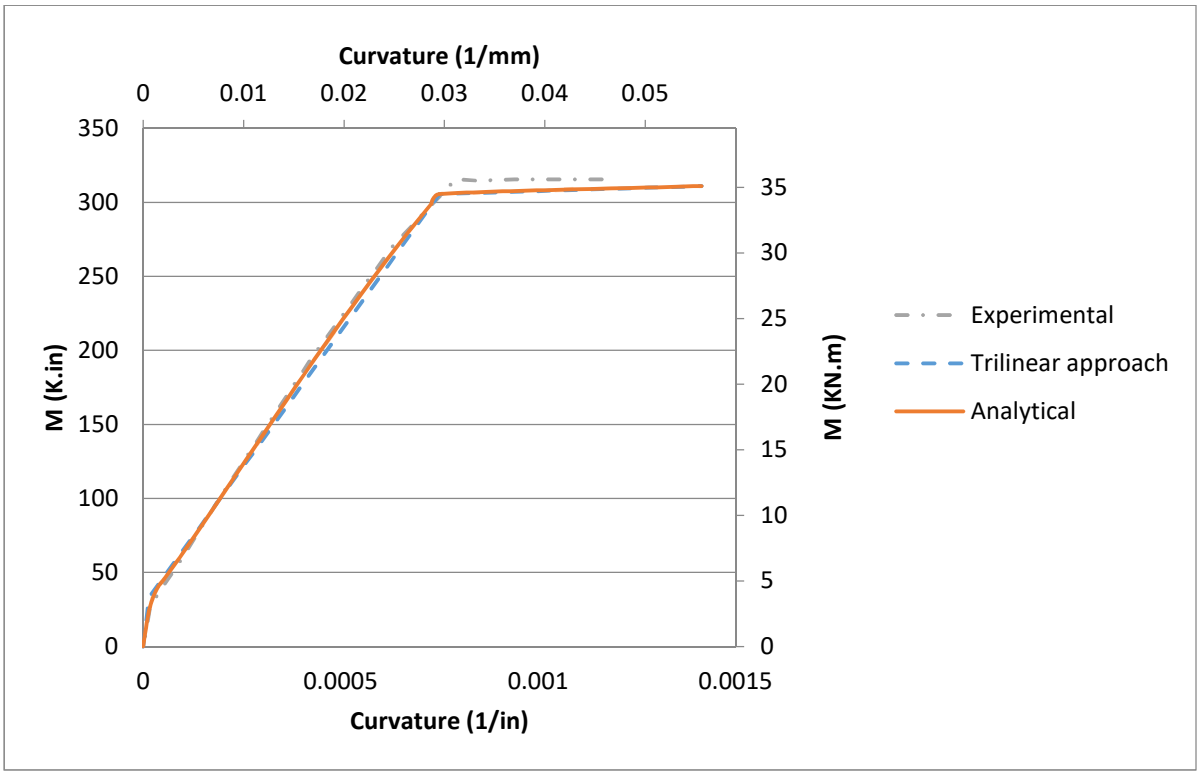

Figure 2-23 Almusallam (1997) moment vs. curvature analytical graphs

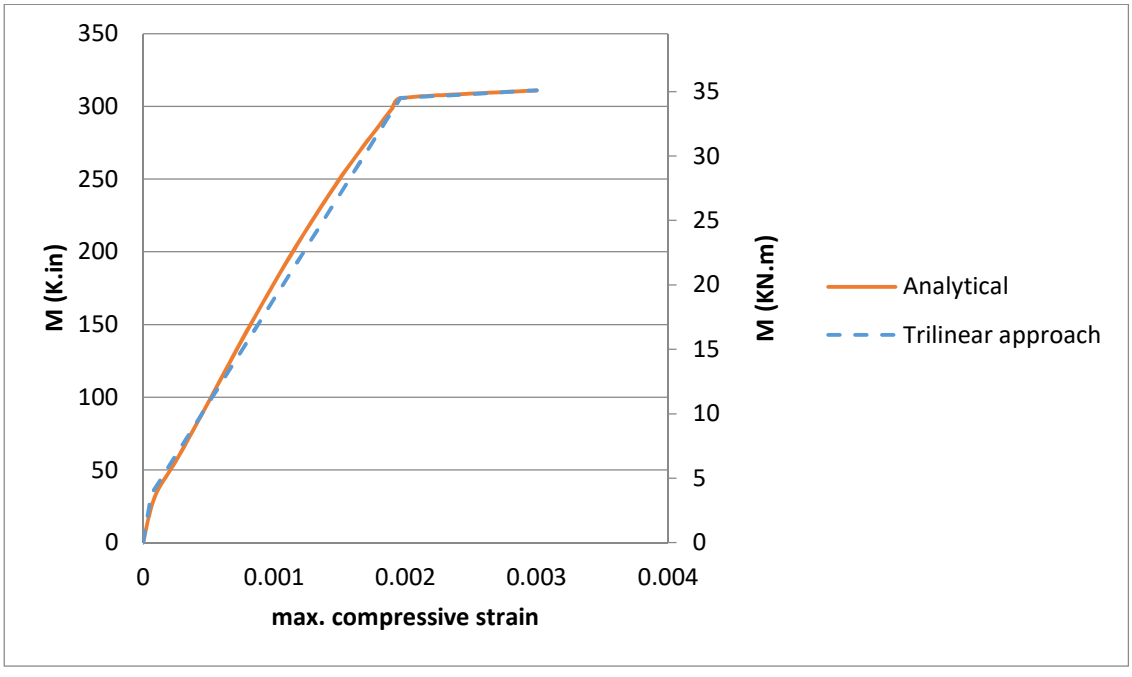

Figure 2-24 Almusallam (1997) moment vs. maximum compressive strain analytical graphs

Almusallam (1997) tested the second beam in four point bending. This beam was also analyzed by the present procedure. The beam section was 210.8 mm* 200.7 mm (8.3 in*7.9 in) with a clear span of 2.7 m (106.4 in). It was doubly reinforced with (ρs=.0144, ρs'=.0009). Figure 2-22 shows the full analytical and experimental response. An excellent match was obtained using the proposed constitutive tension model for the experimental vs. analytical load-deflection data and moment-curvature data. Also the Trilinear behavior of the pre-cracking, post-cracking and post-yielding zones was fully confirmed for the moment-curvature and moment-maximum compressive strain response against the experimental points, see Figures 2-23 and 2-24.

2.5 Conclusions

This study was conducted to develop a tensile constitutive model for nonlinear analysis of flexural concrete beams reinforced with steel bars. An incremental-iterative numerical analysis was followed to study the nonlinear flexural beam behavior and generate the analytical graphs. The proposed tensile constitutive model has a sudden drop at cracking strain, followed by a descending curve up to zero at ($1.4\varepsilon_y$). Series of comparisons were performed to validate the accuracy of the adopted model against the global experimental behavior for a large pool of beams. Two extra comparisons were conducted to check the applicability of the model against the sectional response of different beams. As a result of these comparisons, the model showed an excellent agreement with the validating experiments for the sectional and the global responses. The second main goal of this study was to confirm the trilinear behavior for moment versus curvature and moment versus maximum compressive strain graphs. Through all the comparisons in this study, and by using the proposed model, the trilinear behavior was observed

in all the sectional and the global responses. Even though the literature has several tension stiffening models, the authors believe that this new model is more objective since

1. The final degradation of cracked concrete is related to the yielding strain in steel rather than multiples of the cracking strain of the concrete.
2. The loss of energy due to cracking fracture is captured in a more pronounced way than earlier model.
3. The current model furnishes a single mathematical expression making it easier to implement in analytical formulations.

2.6 References

Almusallam, T.H. (1997). "Analytical Prediction of Flexural Behavior of Concrete Beams Reinforced by FRP Bars," Journal of Composite Materials, Vol. 31, No. 7, pp 640-657, 1997.

Arduini, M., Tommaso, A., and Nanni, A. (1997). "Brittle failure in FRP plate and sheet bonded beams", ACI structral Journal , 94(4), page 363–370.

Decker, R. A. (2007). "Method of Strengthening Monitored Deficient Bridge", Master Thesis, Department of Civil Engineering, Kansas State University.

Eurocode 2 Design of Concrete Structures (2004) – Part 1 "General Rules and Rules for Buildings", The European Standard EN1992-1-1.

Leonhardt, F. (1997). "Crack Control in Concrete Structures", IABSE Surveys, No.S4/77, International Association for Bridges and Structural Engineering, Zurich , pages 26.

Hillerborg, A., Modeer, M., and Peterson, P. E. (1976). "Analysis of crack formation and crack growth in concrete by means of fracture mechanics and finite elements" Cement and Concrete Research, 6(6), pages 773–782.

Rasheed, H. A. (1990) "Inelastic Behavior of Reinforced Concrete Frame Structures". M.Sc. Thesis, University of Baghdad, Iraq.

Rasheed, H. A., Larson, K. H. and Nayyeri Amiri, S. (2013)."Analytical Solution of Interface Shear Stresses in Externally Bonded FRP-Strengthened Concrete Beams", ASCE Journal of Engineering Mechanics, Vol. 139, Issue 1, pages 18-28.

Nayal, R. and Rasheed, H. A. (2006). “Tension stiffening model for concrete beams reinforced with steel and FRP bars” Journal of Materials in Civil Engineering, vol. 18, no. 6, pages 831–841.

Scanlon A., and Murray D. W. (1974). “Time dependent deflections of reinforced concrete slab deflections” Journal of the Structural Division, Vol. 100(9), pages 1911–1924.

Ahmad, S. H. and Barker, R. (1991). “Flexural Behavior of Reinforced High-Strength Lightweight Concrete Beams”, ACI Structural Journal, Vol. 88, No.1, pages 69-77.

Shuaib Ahmad H. and Jaime B. (1991), "Flexural behavior of doubly reinforced high-strength lightweight concrete beams with web reinforcement", ACI Structural Journal, 88(3), pages 351-358.

Spadea G., Bencardino, F., and Swamy, R. N. (1998). “Structural behavior of composite RC beams with externally bonded CFRP.” Journal of Composites for Construction, Vol. 2(3), pages 132–137.

BS 8110 Part 2 1997, Structural Use of Concrete, Part 2, Code of Practice for Special Circumstances, British Standard Institution, London.

Tavares D., Giongo J., and Paultre P. (2008). “Behavior of Reinforced Concrete Beams Reinforced with GFRP bars”, Ibracon Structures and Materials Journal, Vol. 1, pages 285-295.

Vebo A., and Ghali A. (1977). “Moment curvature relation of reinforced concrete slabs.” Journal of the Structural Division, Vol. 103(3), pages 515–531.

Chapter 3 - Shear Crack Prediction in Shallow RC Beams Using a Nonlinear Approach

This study is conducted because of the lack of an existing theory to accurately predict the diagonal tension cracking in shallow reinforced concrete beams. A rational approach is followed to numerically derive the shear stress profile across the depth of the beam in cracked beams based on the smeared crack approach. Furthermore, the determined shear stress distribution coupled with the normal axial stress distribution are used to predict the principal stress variation across the depth and along the shear span using standard Mohr's circle. Following a biaxial stress cracking criterion, the likely diagonal tension cracks along their orientation profile are predicted.

3.1 Introduction

Although many studies have been conducted to fully understand the shear behavior of reinforced concrete beams, the consensus regarding one explanation is missing. There is some sort of agreement regarding the parameters that affect the shear behavior, yet there is no agreement regarding the mechanics of shear behavior. Arch action and beam action are two main explanations which were introduced to represent the shear behavior in cracked reinforced concrete members. However, many researchers suggested a combination of these two approaches. These actions suggest three main mechanisms to transmit shear across the cracked beams without shear reinforcement the compression zone, aggregate interlock between cracks and dowel action of the longitudinal steel reinforcement. The main parameters that influence the beam behavior includes concrete behavior in tension and compression, beam size effect, aggregate size and shear span to depth ratio.

Among the first researchers to study the behavior of reinforced concrete beams under shear loads is Morsch (1903). He was the first to point out that the shear failure is nothing but a principal

tensile failure. Also, he suggested the similarity between web reinforcement behavior and the diagonal members in a truss. However, Talbot (1908-1909), after conducting a series of tests, noted that the stress calculated based on truss analogy is higher than the experimentally measured stresses, yet, he suggested a design modification to limit shear load carried by web reinforcement to two-thirds of the beam capacity. In addition, Talbot's tests showed that beam shear capacity is affected by the concrete characteristics as well as number of longitudinal bars and shear span to effective depth ratio. These findings were confirmed by Richart and Larson (1928). They also stated that stirrup stresses were small until shear cracks are developed and the point of intersection between the crack and web reinforcement produced the highest stress in the reinforcement. Hognestad (1951) described the concept of stress redistribution upon the commencement of the diagonal tensile cracks in restrained beams, where the original stress distribution is no longer valid around the cracked zone. After two years, Zwoyer (1954) observed the similarity between the diagonal tensile cracks and the flexural compression failure (concrete crushing). Using this observation, Moody et al. (1954) described the failure of reinforced concrete beams to compose of two stages; the first stage includes diagonal tension cracking followed by crushing as a second stage. However, the described failure mode was found to be controlled by (M/Vd) ratio. With smaller ratios, the described mode of failure occurs. Larger (M/Vd) ratio resulted in almost pure flexural failure.

In this study, the authors attempt to present a mechanics based approach to illustrate the behavior of shallow reinforced concrete beams under concentrated load, taking into account the different stages of loading; pre-cracking, post cracking and post yielding. Shear stresses are evaluated based on the shear differential equation and the smeared crack approach. These shear stresses coupled with the normal stress distribution are used to predict the principal stress variation across

the depth and along the shear span using standard Mohr's circle. Following a biaxial stress cracking criterion like that of Kupfer and Gerstle (1973), the likely diagonal tension cracks are predicted.

3.2 Nonlinear sectional Analysis

The stress-strain relationships for the concrete and the reinforcement steel are assumed to be independent of each other. The axial stress in steel would be only a result of the axial strain in the steel.

3.2.1 Concrete Behavior

The concrete stress-strain relationship is assumed to follow the Hognestad's curve, Equation 3.1, for compressive stresses (f_c) and a linear relationship with a slope equal to the concrete modulus of elasticity (E_c) up to cracking strain (ε_{cr}) in tension, see Figure 3-1. This linear relationship is then followed by a descending curve as a numerical function in (ε_{cr}) and the steel yielding strain (ε_y), Figure 3-4.

$$f_c = f_c' \left(2\frac{\varepsilon_c}{\varepsilon_{c'}} - \left(\frac{\varepsilon_c}{\varepsilon_c'}\right)^2\right) \qquad (3.1)$$

The concrete tensile rupture stress (f_r) is taken as a lower bound equivalent to $5 - 7.5\sqrt{f_c'}$, for light weight concrete this value is reduced by 25%. A linear relationship with a slope equal to the concrete modulus of elasticity (E_c) up to cracking strain (ε_{cr}) in tension is assumed.

The concrete behavior in tension after the cracking strain is described using Equation (3.2). The constants in the equation were calibrated against a large pool of four points bending tests on flexural beams.

$$\frac{f_t}{0.5fr} = 1 - \frac{1}{\ln\left(\frac{1.4\varepsilon_y}{\varepsilon_{cr}}\right)} \ln\left(\frac{\varepsilon_t}{\varepsilon_{cr}}\right) \qquad (3.2)$$

This proposed descending function on the domain ($\varepsilon_{cr} \leq \varepsilon_t \leq 1.4\varepsilon_y$) reaches its peak (0.5 f_r) at the cracking strain (ε_{cr}) and continues to descend till zero when the tensile strain reaches (1.4 ε_y), see Figure 3-2. This function is an average function between the tension softening which exist near the cracking strains and the tension stiffening that activates around the steel location.

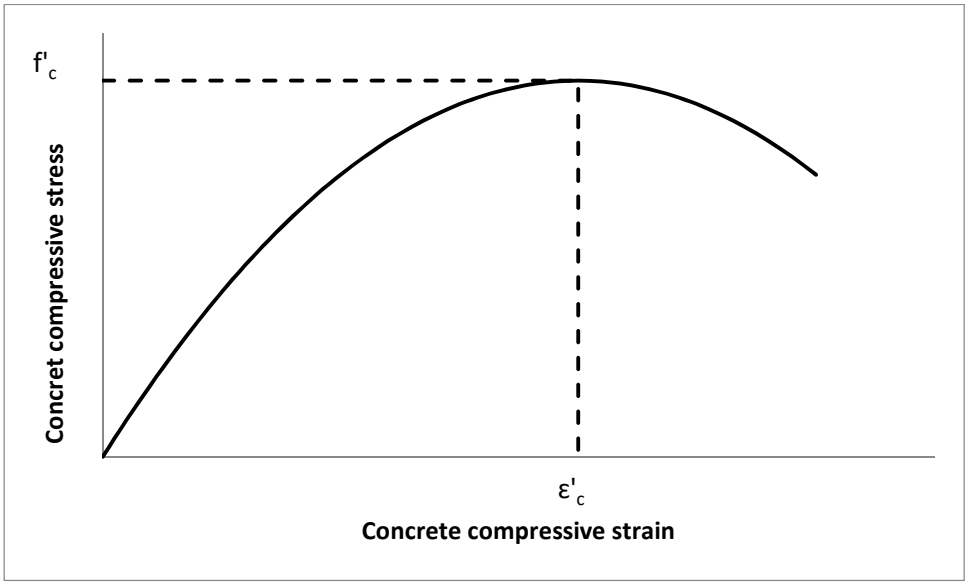

Figure 3-1 Concrete compressive stress-strain curve (Hognestad's Parabola)

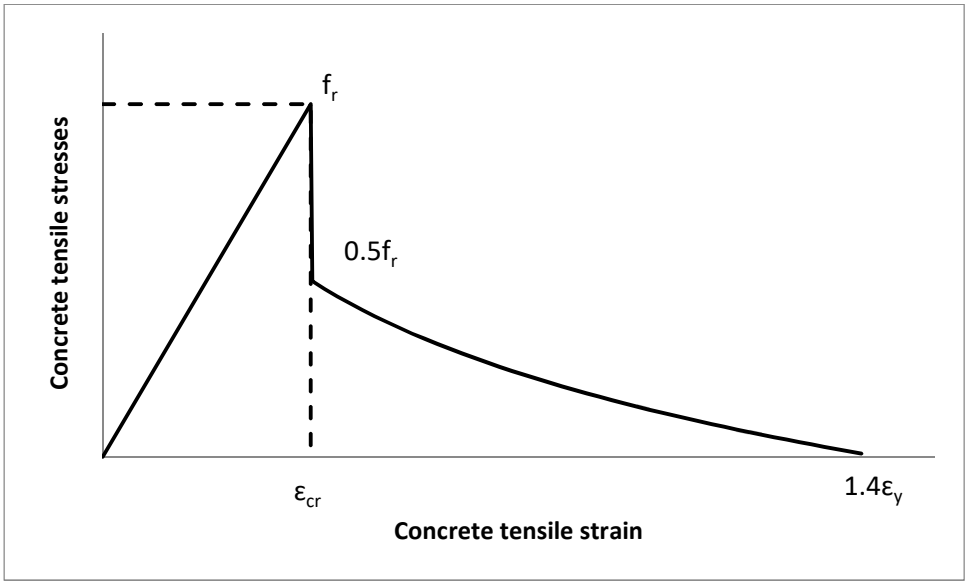

Figure 3-2 Concrete tensile stress-strain curve

3.2.2 Steel Behavior

Regarding the steel axial stress-axial strain relationship, a bilinear relationship is assumed in the compressive and the tensile analysis, see Figure 3-3.

$$f_s = E_s \varepsilon_s \leq f_y \quad (3.3)$$

$$f_y = E_s \varepsilon_y \quad (3.4)$$

Where (f_s) is the steel stress corresponding to the axial stress (ε_s), (E_s) is the modulus of elasticity of steel, (f_y) is the yielding stress in steel. The steel is assumed to start hardening after exceeding the yielding strain (f_y) according to the following equation

$$f_s = f_y + E'_s(\varepsilon_s - \varepsilon_y), when\ f_s > f_y \quad (3.5)$$

(E'_s) is the slope of steel hardening after yielding and it is determined based on the yielding strength (fy), Table 3-1 shows the relationship between the estimated (E'_s) and the corresponding (f_y) (Rasheed (1990)).

Table 3-1 The Relationship between the (E'_s) and the corresponding yielding stress (f_y)

f_y (ksi)	E'_s / E_s
40-45	0.3-0.7%
45-50	0.7-1.2%
50-63	1.2-2.5%

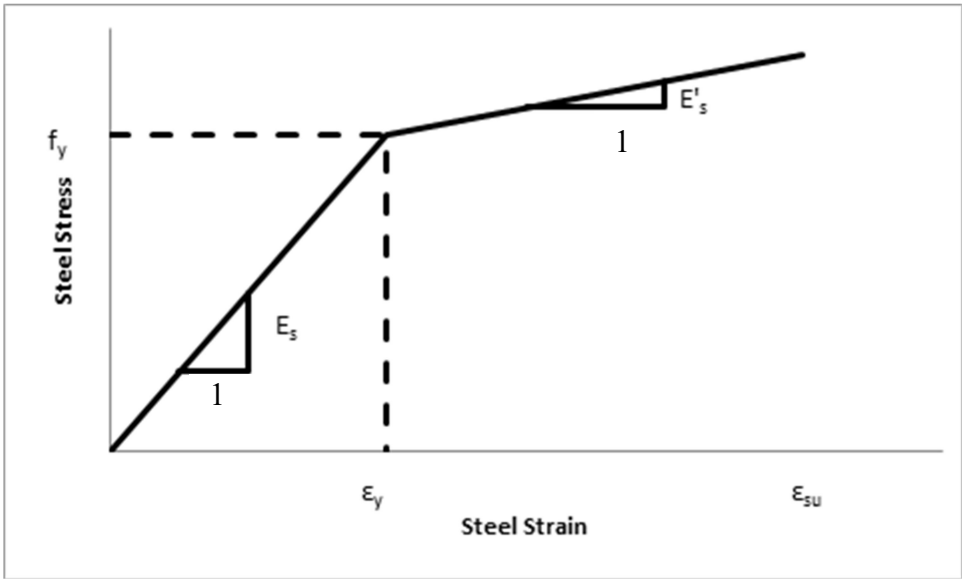

Figure 3-3 Steel billinear behavior in tension and compression

3.3 Sectional Analysis approach

3.3.1 Forces

3.3.1.1 Compressive Forces

Compressive concrete contribution

By integrating the Hognestad's profile over the area from the neutral axis up to the maximum compressive concrete fiber, the concrete compressive force (C_c) is derived for the section based on the following equations

$$C_c = \int_0^C f_c . b \, dy \qquad (3.6)$$

$$C_c = f_c' b.\frac{\Phi}{\varepsilon_c'}(c^2 - \frac{\Phi}{3}\frac{C^3}{\varepsilon' c}) \quad (3.7)$$

Compressive Steel Contribution

The compressive steel force (C_s) is a direct linear relationship with the corresponding steel strain (ε_s'). This relationship was driven based on the assumption of the bilinear behavior for the steel analysis.

$$C_s = A_s' f_s - A_s' f_c' ((2\frac{\varepsilon_s{}'}{\varepsilon_c{}'} - \_\left(\frac{\varepsilon_s{}'}{\varepsilon_c{}'}\right)^2) \quad (3.8)$$

3.3.1.2 Tensile Forces

Tensile steel Contribution

The tensile steel force (T_s) follows the same bilinear behavior based on the following equation

$$T_s = A_s E_s \varepsilon_s, when\ f_s \leq f_y \quad (3.9)$$

$$T_s = A_s(f_y + E_s'(\varepsilon_s - \varepsilon_y)), when\ f_s > f_y \quad (3.10)$$

Tensile Concrete contribution

The concrete tensile capacity is divided into two main profiles, Figure 3-2. The first profile is a linear relationship up to the cracking strain (ε_{cr}) with a slope equal to the concrete modulus of elasticity (E_c). This profile leads to a tensile force (T_{c1}) equals to

$$T_{c_1} = \int_0^{d_t} f_t . b\ dy \quad (3.11)$$

$$T_{c_1} = \frac{f_r^2}{2E_c\Phi} \quad (3.12)$$

The second profile is a descending curve which majorly contributes in the total concrete tensile capacity. This profile is a result of the concrete softening, concrete stiffening due to the steel bond as well as the residual stresses due to shrinkage effect. The tensile force due to this profile (T_{c2}) is calculated as follow

$$T_{c2} = \int_{d_{cr}}^{d_{ts}} bf_t dy = b\int_{d_{cr}}^{d_{ts}} 0.5f_r - \frac{0.5f_r}{\ln\left(\frac{1.4\varepsilon_y}{\varepsilon_{cr}}\right)} \ln\left(\frac{\varepsilon_t}{\varepsilon_{cr}}\right)\, dy \quad (3.13)$$

Where y is measured from the neutral axis

$$T_{c2} = \left[-\frac{0.5bf_r}{\ln\left(\frac{1.4\varepsilon_y}{\varepsilon_{cr}}\right)}\left(y\ln(\varphi) + yln(y) - y - yln(\varepsilon_{cr})\right) + 0.5f_r y\right]_{\varepsilon_{cr}/\varphi}^{1.4\varepsilon_y/\varphi} \quad (3.14)$$

Where,

$$d_{ts} = 1.4\varepsilon_y/\varphi \quad (3.15)$$

3.3.1.3 Moments

Compressive concrete contribution

The point of application of concrete compressive force is measured from the extreme compressive fiber (ɣ.c) based on volume centroid calculations. Where (C) is the depth of the compression zone and (ɣ) is a ratio between zero and one.

$$ɣ = 1 - \frac{\int_0^{\varepsilon_{cf}} \varepsilon_c . f_c . d\varepsilon_c}{\varepsilon_{cf} \int_0^{\varepsilon_{cf}} f_c . d\varepsilon_c} = \frac{\frac{1}{3} - \frac{\varepsilon_{cf}}{12e_c'}}{1 - \frac{\varepsilon_{cf}}{3e_c'}} \quad (3.16)$$

$$M_{cc} = (C - ɣ.C) * C_c \quad (3.17)$$

Compressive Steel Contribution

The compression steel moment is calculated according to the following equation.

$$M_{cs} = C_s(C - d') \quad (3.18)$$

Tensile Concrete contribution

(M_{tc1}) is the moment induced due to the concrete resistance up to the cracking point. While, (M_{tc2}) is the moment due to the constitutive tensile model.

$$M_{tc} = T_{c1} . \frac{2}{3} \frac{f_r}{E_c . \Phi} \quad (3.19)$$

$$M_{tc2} = \int_{d_{cr}}^{d_{ts}} bf_t y dy = b\int_{d_{cr}}^{d_{ts}} [0.5f_r - \frac{0.5f_r}{\ln\left(\frac{1.4\varepsilon_y}{\varepsilon_{cr}}\right)} \ln\left(\frac{\varepsilon_t}{\varepsilon_{cr}}\right)] y\, dy \quad (3.20)$$

Where, y is measured from the neutral axis.

$$M_{tc2} = [-\frac{0.5bf_r}{\ln\left(\frac{1.4\varepsilon_y}{\varepsilon_{cr}}\right)}\left(\frac{y^2}{2}\ln(\varphi) + \frac{y^2}{2}ln(y) - \frac{y^2}{4} - \frac{y^2}{2}ln(\varepsilon_{cr})\right) + 0.5f_r\frac{y^2}{2}]_{\varepsilon_{cr}/\varphi}^{1.4\varepsilon_y/\varphi} \quad (3.21)$$

Tensile steel Contribution

The contribution of the moment induced due to the steel reinforcement at any stage of loading is determined as follows

$$M_{ts} = T_s(d - C) \quad (3.22)$$

3.3.2 Moment-Curvature Calculations

A numerical procedure was followed to generate the moment-curvature curve. In this procedure, the maximum compressive fiber strain value (ε_{cf}) was gradually increased until reaching the concrete crushing strain of (0.003). In order to accurately calculate the strain profile under each step value of ε_{cf}, the correct depth of the compression zone (c) was necessary to define the strain profile and the corresponding stress profile and forces/moments. The sectional force equilibrium equation was then applied to validate the depth of the compression zone (c) by iterating for the correct depth of compression zone that makes the summation of forces equal to zero, equilibrium is maintained.

$$\varphi = \frac{\varepsilon_{cf}}{c} \quad (3.23)$$

$$\varepsilon_s = \varphi(d - c) \quad (3.24)$$

$$\varepsilon_s' = \varphi(c - d') \quad (3.25)$$

$$\varepsilon_{sf} = \varphi(h - c) \quad (3.26)$$

The summation of moments due to concrete and steel contributions then yielded to the total moment capacity of the section, and the moment-curvature curves were fullgenerated, see

Figure 3-4. The progressive moment-curvature calculation procedure is described in a flow chart up to steel yielding. However, the same procedure may be followed to generate the response of the post-yielding region, see Figure 3-5.

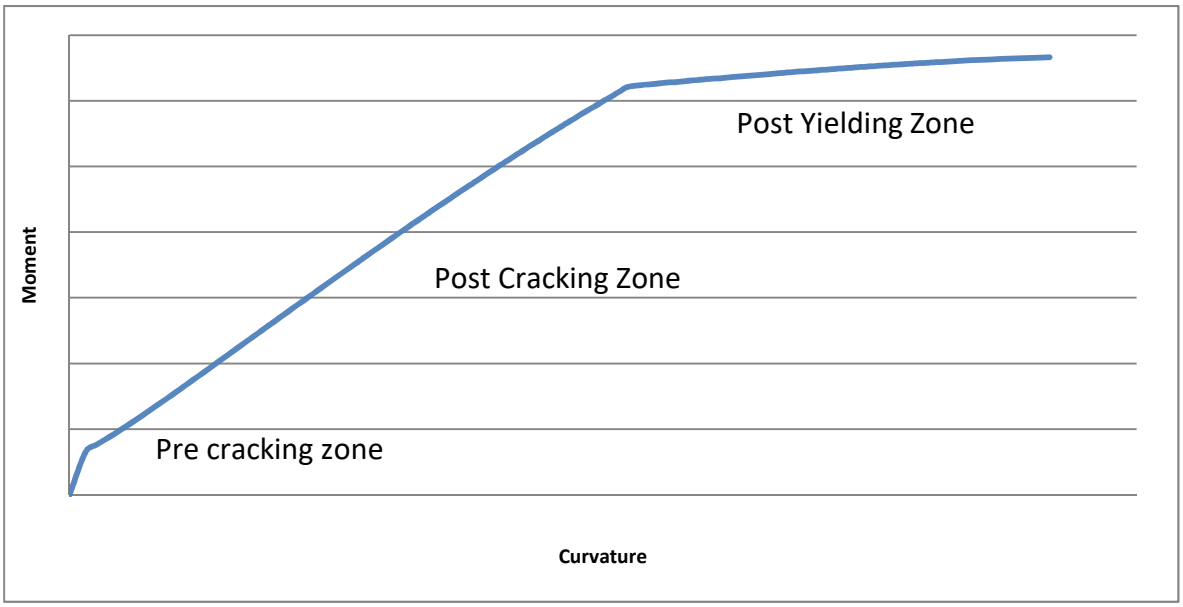

Figure 3-5 Typical beam moment vs. curvature sectional response

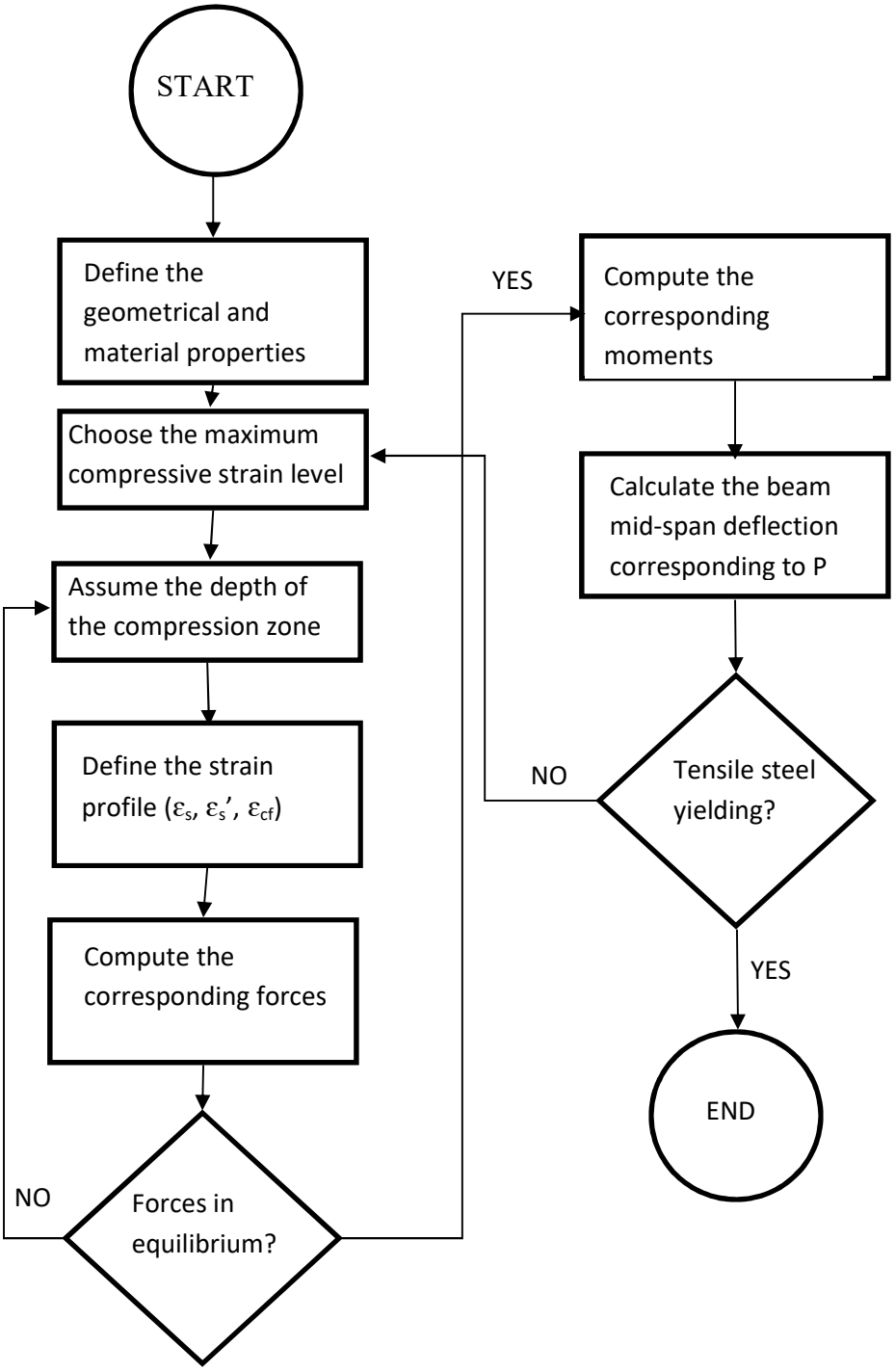

Figure 3-6 Flexural analysis flow chart up to the yielding point

3.4 Differential Sectional Analysis

3.4.1 Shear Stresses Differential Equation

Shear stresses distribution over a shallow beam depth is formulated through the axial forces acting on the beam cross section. Considering an infinitesimal element with length dx of the beam, the differential bending moment acting over dx is dM, Figure 3-6. At any given depth, the equilibrium of forces in the longitudinal direction is satisfied through the longitudinal shear τyx, Figure 3-7. Also from equilibrium, the longitudinal shear is equal to the transversal shear τxy.

$$\sum F_x = 0 \tag{3.27}$$

$$\int \sigma'.dA - \int \sigma''.dA - \tau(b.dx) = 0 \tag{3.28}$$

$$F' - F'' - \tau(b.dx) = 0 \tag{3.29}$$

$$dF - \tau(b.dx) = 0 \tag{3.30}$$

$$\tau = \frac{1}{b}\frac{F'-F''}{dx} = \frac{1}{b}\frac{dF(\varphi,\varepsilon)}{dx} \tag{3.31}$$

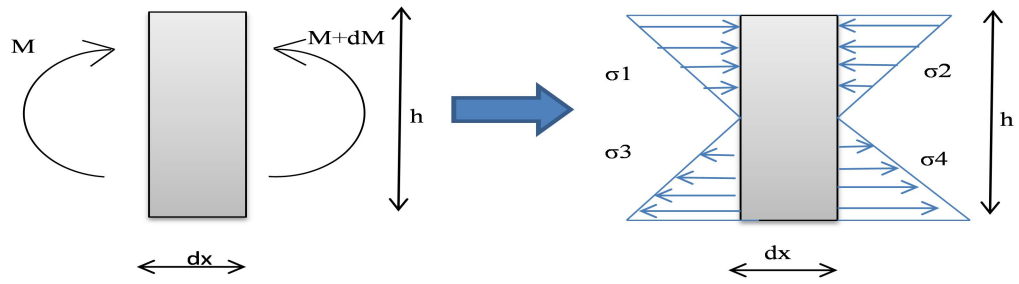

Figure 3-7 Axial stress distribution over an infinitesimal element dx

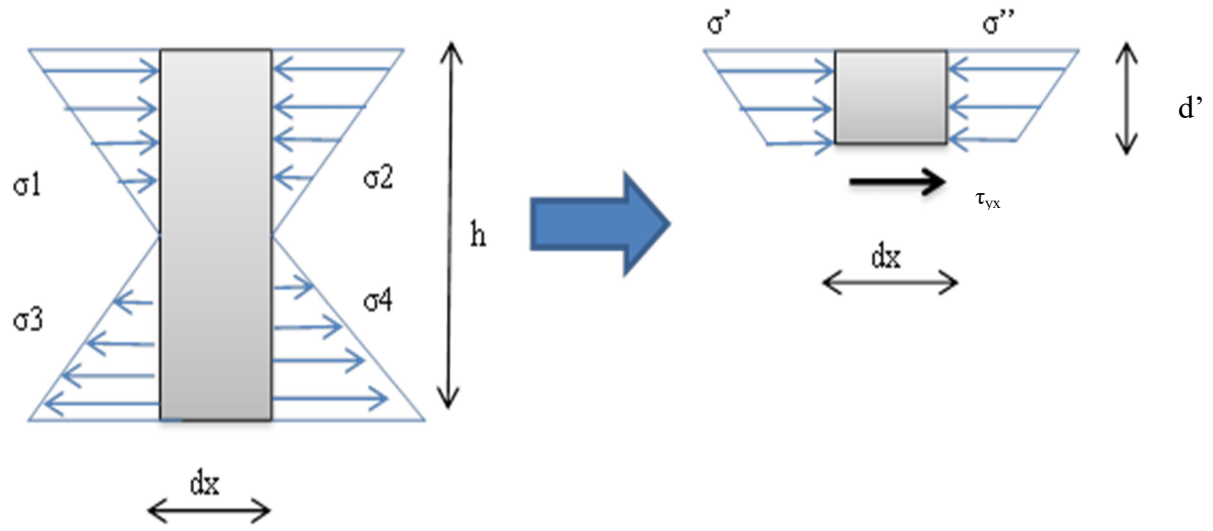

Figure 3-8 Axial stress distribution over an infinitesimal element dx and depth d'

3.4.2 Numerical Evaluation of Shear Stresses Distribution

For each load level, one hundred vertical sections were taken over the beam shear span length. For each vertical section, 25 equally spaced nodes were taken along the height of the section. At any given depth, the axial forces are calculated by integrating the axial stresses over the covered distance. By summing the axial forces above a given depth for two constitutive vertical sections, the shear stress at the given depth is evaluated, Equation (3.31).

3.4.2.1 Compressive concrete contribution

By integrating the Hognestad's profile over the area from the top of the section to the specific depth d_c, the concrete compressive force (C_c) is derived for the section based on the following equations

$$C_c = \int_{c-d_c}^{c} f_c . b\, dy = \int_{c-d_c}^{c} b f_c' \left(\frac{2\varepsilon_c}{\varepsilon_c'} - \left(\frac{2\varepsilon_c}{\varepsilon_c'}\right)^2\right) dy \quad (3.32)$$

where y is measured from the neutral axis

$$C_c = b f_c' \frac{\phi}{\varepsilon_c'} \left(y^2 - \frac{\phi}{3}\frac{y^3}{\varepsilon_c'}\right)_{c-d_c}^{c} \quad (3.33)$$

Where, d_c is measured from the top of the section

3.4.2.2 Compressive Steel Contribution

The compressive steel force (C_s) is a direct linear relationship with the corresponding steel strain (ε_s'). This relationship was driven based on the assumption of the bilinear behavior for the steel analysis.

$$C_s = A_s' f_s' - A_s' f_c' ((2\frac{\varepsilon_s'}{\varepsilon_c'} - -\left(\frac{\varepsilon_s'}{\varepsilon_c'}\right)^2) \quad (3.34)$$

3.4.2.3 Tensile Concrete contribution

The concrete tensile capacity is divided into two main profiles

$$T_{c_1} = \int_0^{d_t} f_t . b \, dy \quad (3.35)$$

Where y is measured from the neutral axis and d_t is measured from the neutral axis

$$T_{c_1} = \frac{bE_c \varphi d_t^2}{2} \quad (3.36)$$

$$T_{c2} = \int_{d_{cr}}^{d_t} bf_t dy = b\int_{d_{cr}}^{d_t} 0.5f_r - \frac{0.5f_r}{\ln(\frac{1.4\varepsilon_y}{\varepsilon_{cr}})} \ln\left(\frac{\varepsilon_t}{\varepsilon_{cr}}\right) dy \quad (3.37)$$

Where y is measured from the neutral axis

$$T_{c2} = [-\frac{0.5bf_r}{\ln(\frac{1.4\varepsilon_y}{\varepsilon_{cr}})}(y\ln(\varphi) + yln(y) - y - yln(\varepsilon_{cr})) + 0.5f_r y]_{\varepsilon_{cr}/\varphi}^{d_t} \quad (3.38)$$

3.4.2.4 Tensile steel Contribution

The tensile steel force (T_s) follows the same bilinear behavior based on the following equations

$$T_s = A_s E_s \varepsilon_s, \; when \; f_s \leq f_y \quad (3.39)$$

$$T_s = A_s(f_y + E_s'(\varepsilon_s - \varepsilon_y)), \; when \; f_s > f_y \quad (3.40)$$

3.4.2.5 Constructing shear stress distribution

Typical shear stress profiles are numerically generated using Equations (3.32)-(3.40) substituted into Equation (3.31). Figure 3-8 presents the shear stress distribution for un-cracked section. The stress profile is very similar to the classical parabolic shear stress distribution in linear beams

except for the effect of dowel action shown at the level of tensile reinforcement. Figure 3-9 shows the shear stress distribution for a post-cracked concrete section. It is interesting to observe the shear stress shifts from positive to small negative value which is offset to zero by the tension stiffening contribution, Figure 3-9. Figure 3-10 illustrates the shear stress distribution for post yielded section. It is evident that the shear stresses within the compression block start negative in value due to the descending part of Hognestad's parabola. Then these stresses shift to positive values. In addition, dowel action shift shear stresses to zero shear stress since tension stiffening is vanished at this stage of loading.

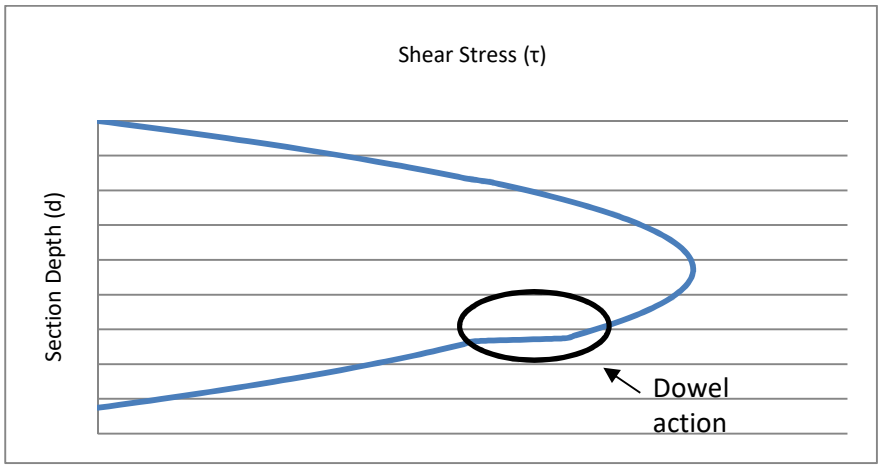

Figure 3-9 Typical pre-cracking shear stress distribution

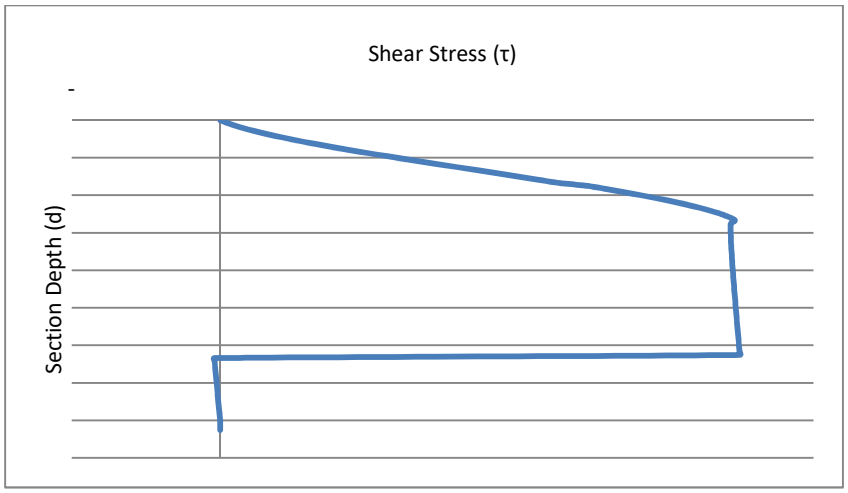

Figure 3-10 Typical post cracking shear stress distribution

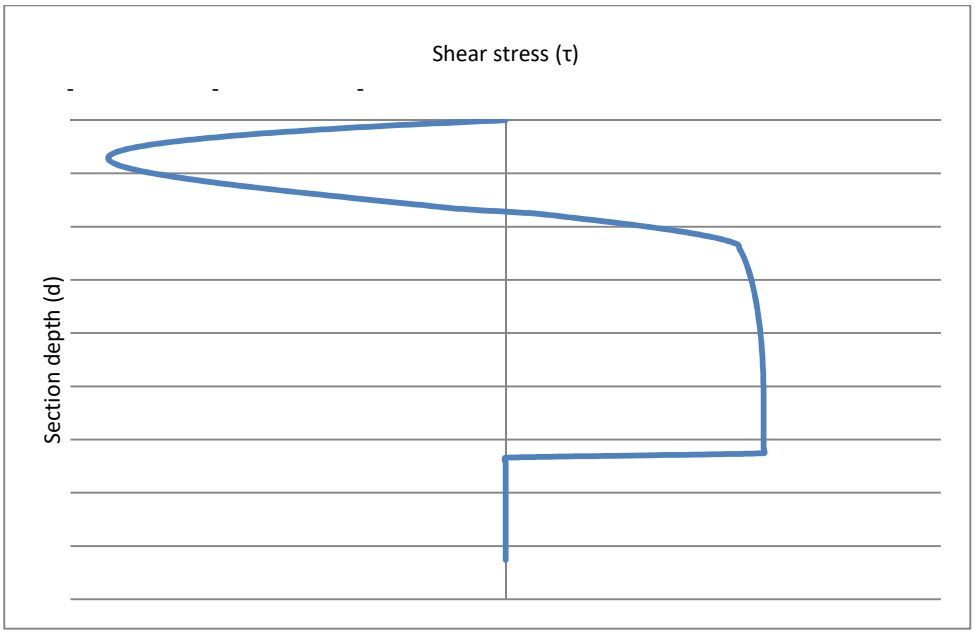

Figure 3-11 Typical post yielding shear stress distribution

Principal stress analysis

3.5 Principal stress by Mohr's circle

By applying Mohr's Circle for each numerical node, the principle stresses σ_1, σ_2 and their orientations are calculated.

$\sigma_{avg} = \frac{\sigma_x + \sigma_y}{2}$ Where, σy=0 (beam theory) (3.41)

$R = \sqrt{\left(\frac{\sigma_x - \sigma_y}{2}\right)^2 + \tau_{xy}^2}$ (3.42)

max $principle\ stress\ \sigma_1 = \sigma_{avg} + R$ (3.43)

min $principle\ stress\ \sigma_2 = \sigma_{avg} - R$ (3.44)

$Tan(2\theta) = \frac{2\tau_{xy}}{\sigma_x - \sigma_y}$ (3.45)

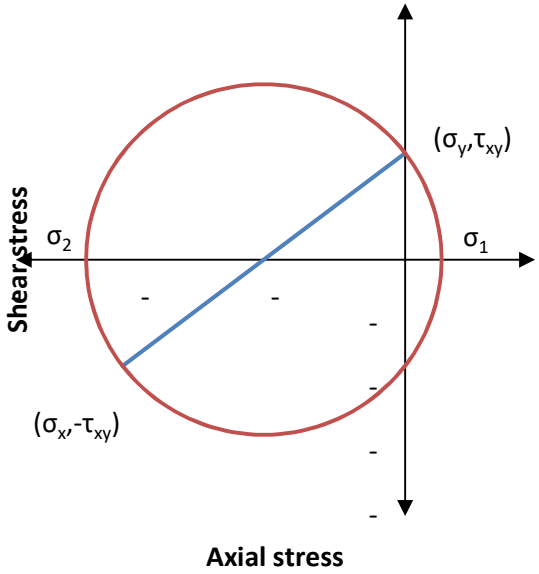

Figure 3-12 Mohr's circle

3.6 Kupfer and Gerstle biaxial cracking criterion

Kupfer and Gerstle (1973) have suggested an analytical maximum strength envelope for biaxial loading. Complying with this envelope, Kupfer and Gerstle also proposed simplified expressions of biaxial strength for different stress combinations. For tension-compression, Kupfer and Gerstle adopted a linear reduction of tensile strength in accordance with the increased compression

$$\sigma_{1t} = \left(1 - \frac{0.8\sigma_{2c}}{f'c}\right) f_r \qquad (3.46)$$

Where (σ_{1t}) is the principal tensile stress and (σ_{2c}) is the principal compressive stresses.

$if\ (\sigma_1(principal\ tensile\ stress) > \sigma_{1t})$ {"Cracked Concrete"}

3.7 Results

In this section, the formulation developed above is applied to retrieve the shear stress distribution of cracked concrete at various levels of load and at different sections along the shear span under the same load. Furthermore, Mohr's circle is used to extract the principal stresses across the beam depth while using Kupfer and Gerstle (1973) criterion to predict the shear-flexural cracks. Finally, crack maps are developed for one example along the shear span under eight different load levels and the cracked zone is shaded to indicate likely existence of cracks.

3.7.1 Example one

The purpose of this example is to confirm the accuracy of the non-linear numerical sectional analysis used in this study to predict the shear stress distributions in shallow beams. This beam was cast and tested by Decker (2007). The rectangular beam is a 305mm*153mm (6 in x 12) in cross section. It has a length of 4.88 m(16 ft) with a clear span of 4.72 m(15.5 ft) . The main flexural reinforcement consists of 2φ16 (2 No. 5) bars with 2φ10 (2 No. 3) bars used for the compression steel just to provide a caging framework for the shear reinforcement, Figure 3-12. The concrete that was used in casting the beam is ready mix with a mix design nominal compressive strength of 34.5 MPa (5000 psi). The material properties of the reinforcing steel were provided by the manufacturer to have a modulus of 200,000 MPa(29000 ksi) and yield strength of 482.3 MPa(70 ksi).

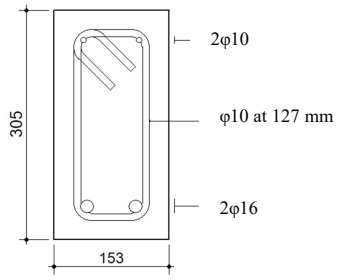

Figure 3-13 Decker (2007) control beam R1 cross section

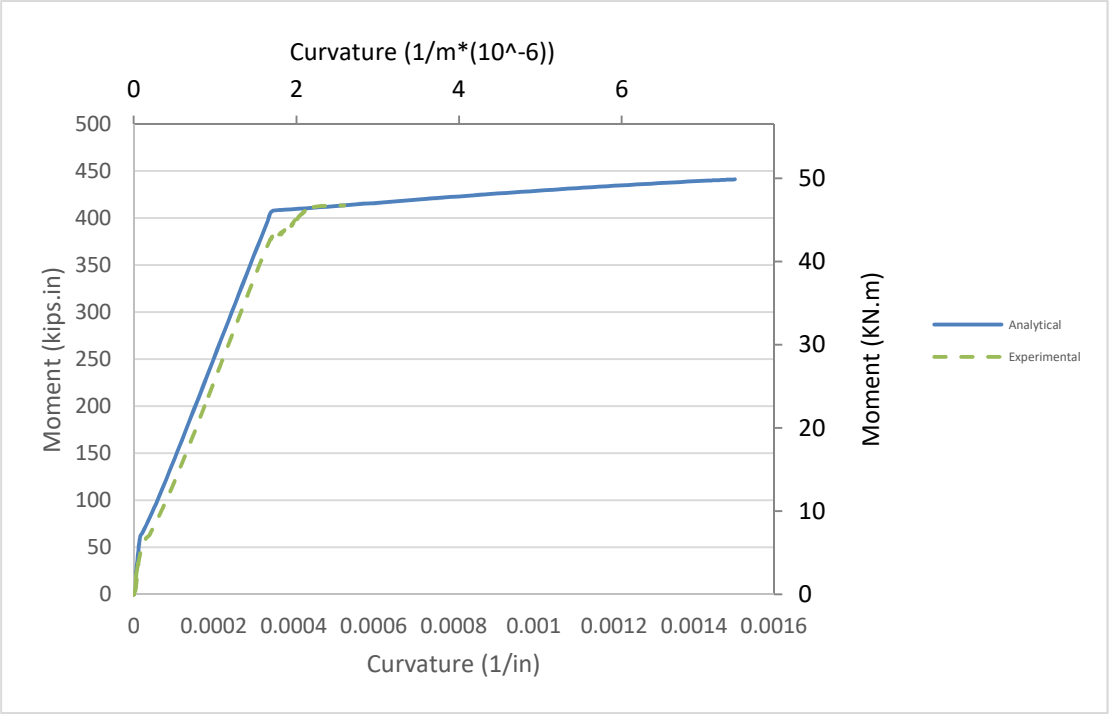

Figure 3-14 Decker (2007) control beam R1 moment vs. curvature

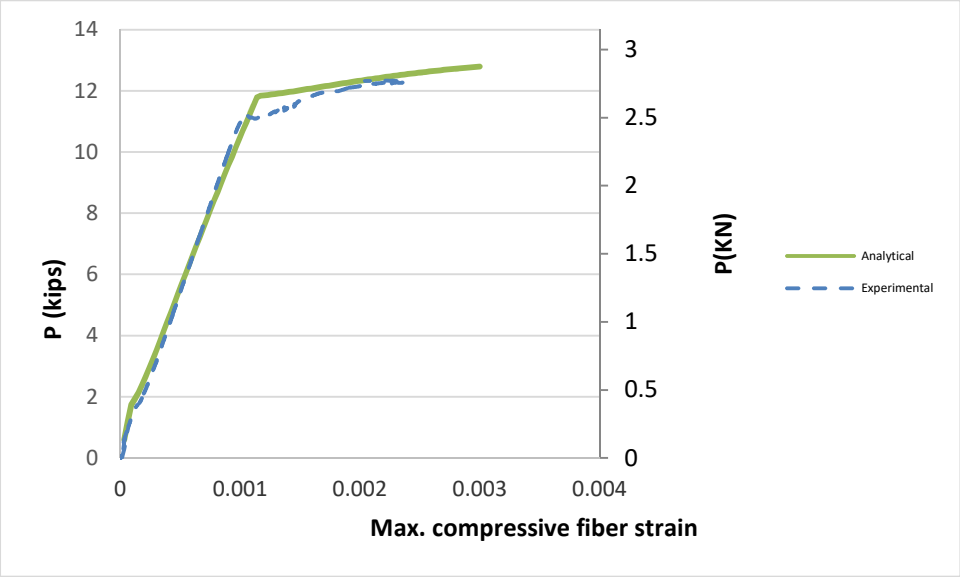

Figure 3-15 Decker (2007) control beam R1 Load vs. Max. compressive fiber strain

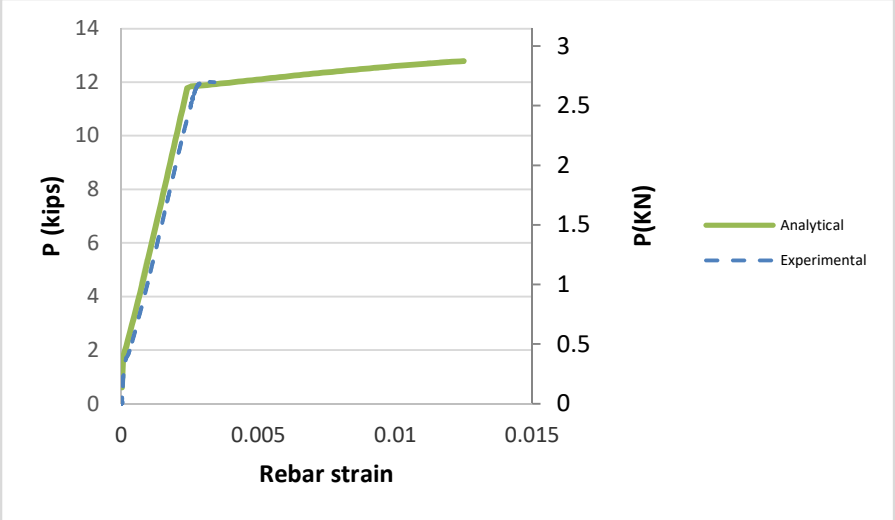

Figure 3-16 Decker (2007) control beam R1 Load vs. rebar strain

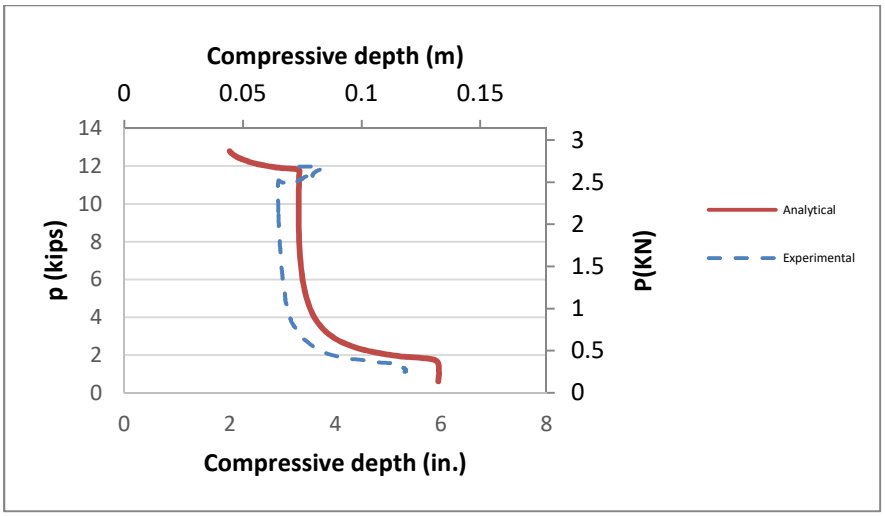

Figure 3-17 Decker (2007) control beam R1 Load vs. neutral axis depth

A very good agreement of the reported experimental results is observed against the proposed numerical approach. Decker (2007) tested this control beam under four points bending with shear span of 175.3 mm (5.75 ft). Two strain gauges were installed on the top surface of the beam to report the maximum compressive strain. Another two strain gauges were installed on the reinforcing flexural rebar to report the rebar strain. Figure 3-14 and Figure 3-15 present a comparison between the numerical and the experimental results of the maximum compressive strain and the rebar strain. These two graphs show a good agreement in the post cracking zone and the post yielding zone up to the failure of the strain gauges. The numerical variation of the neutral axis and the experimentally evaluated neutral axis comparison is given in Figure 3-16. A generally good comparison is observed as well.

These comparisons are presented to illustrate the accuracy of the proposed method in predicting the sectional response of the beam. The bending moment vs. beam curvature comparison shows an excellent agreement of the sectional response of the beam.

3.7.2 Example two

The second beam was tested by Almusallam (1997). The tested rectangular beam has a 200 mm*210 mm (7.87 in x 8.26) in cross section. It has a length of 2.7 m (106.3 in). The main flexural reinforcement consists of 3 φ 14 mm bars with 1 φ 6.25 mm bars used for the compression steel just to provide a caging framework for the shear reinforcement. The beam has shear reinforcement consisting of φ 8 mm stirrups at 120 inches spacing.

The concrete nominal strength is 31.3 MPa (4540 psi). The reinforcing steel has a yielding strength of 552.6 MPa (80.2 ksi) and a modulus of elasticity of 200000 MPa(29000 ksi).

In this second example, the axial stress distribution and the shear stress distribution as well as the principal stress distribution are calculated across the height of the beam at three different location over the shear span. The first location (section one) is after the cracked section and the second location (section two) is positioned just before the yielding section, these two sections were analyzed under 75% of the failure load. The third location (section three) is positioned just under the load at the failure of the beam.

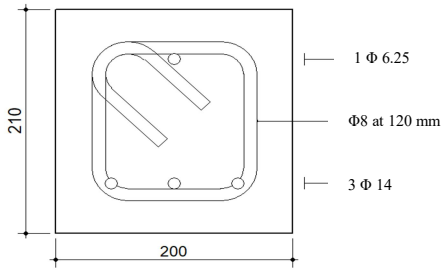

Figure 3-18 Almusallam 1997 control beam cross section

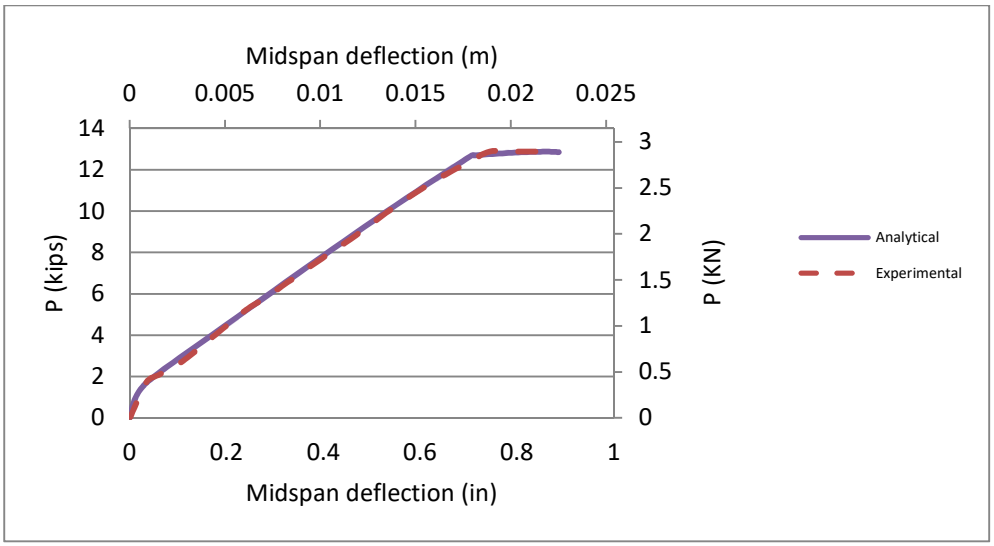

Figure 3-19 Almusallam 1997 control beam Load vs. mid-span deflection

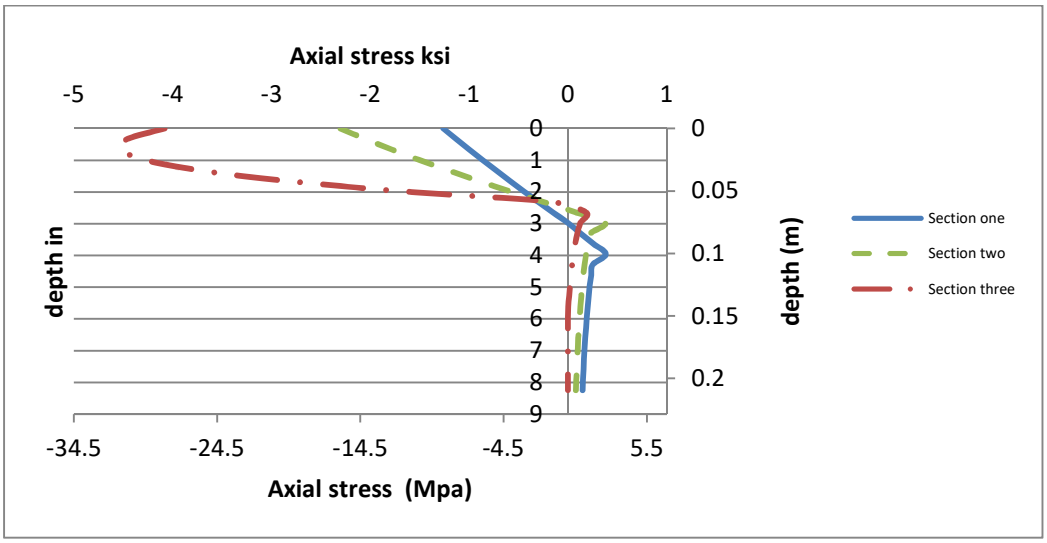

Figure 3-20 Almusallam 1997 axial stresses of the three sections

The axial stresses over the height of the beam is calculated in accordance to the concrete material properties defined earlier. Where Hognestad's parabola describes the concrete behavior in compression up to the neutral axis, followed by a linear tensile model till the cracking strain and a descending curve for the tension stiffening till 1.4 steel yielding strain. In section one and section two, in the post cracking zone, maximum compressive stresses at the top of the beam

didn't exceed 50% of f'c, while section three, under the failure load at the load location, did generate the full Hognestad's parabola.

To continue with the analysis, shear stresses were then evaluated for the same sections using the numerical differential sectional analysis. For each given section, a preceding section at a differential distance was taken to be analyzed. In order to compute the shear stress at any given depth d, the axial forces within the depth d for the two successive sections are calculated. Then, the shear stress is found by numerically applying Equation (3.31). The shear stress distribution varies depending on the section location. A section within the pre-cracking zone follows the well-known symmetrical second degree parabola, where it peaks around the mid-height of the section. However, for the sections located in the post cracking and the post yielding zone, it was found that the shear distribution is no longer symmetric due to the different concrete behavior in tension and compression as well as the existence of the steel, known as dowel action. There are few locations over the height of the section, at which the shear distribution changes. The shear stress distribution over the compressive depth tends to be parabolic with a slight constant change at the compressive steel (Zone A), see Figure 3-20. This change is clearer with more compressive steel area. Just after the cracking, the shear stress distribution changes the slope drastically. This change of slope indicates the beginning of the tension stiffening model. The rapid increase of the shear stress at the beginning of the tension stiffening zone tends to be more pronounced at the beginning of the post cracking zone (Zone B), see Figure 3-20, and it becomes less pronounced towards the yielding section, Figure 3-21. Within the tension stiffening model, the shear stress distribution had a linear slope (Zone C). A clear dowel action effect is observed at the flexural steel depth. This effect is a constant drop in shear stresses which could reach a small negative shear stress value that indicates a change in the shear stress direction. This

negative change in shear stress direction is understandable due to the decrease in the tension stiffening forces as you move toward the location of applied load (i.e. later stages of the post cracking zone). Finally, as expected, the shear stress converges to zero at the soffit of the beam (Zone D).

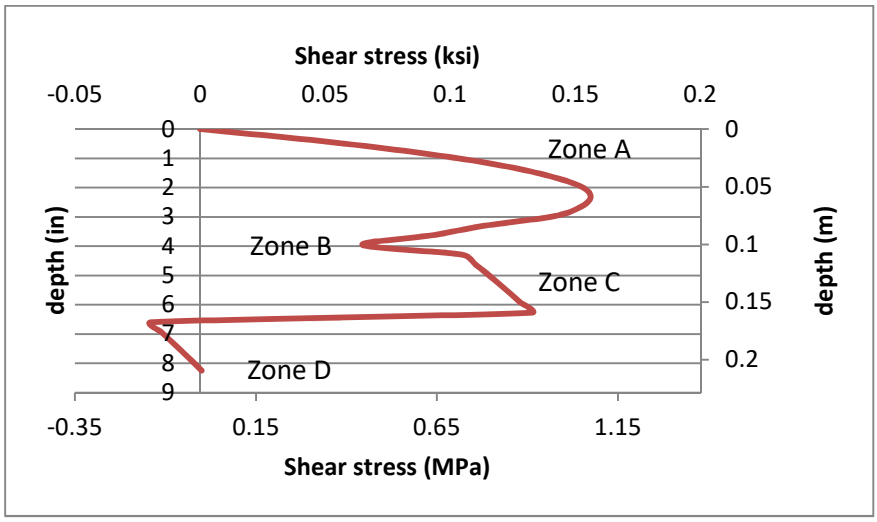

Figure 3-21 Almusallam 1997 shear stress distribution of section one

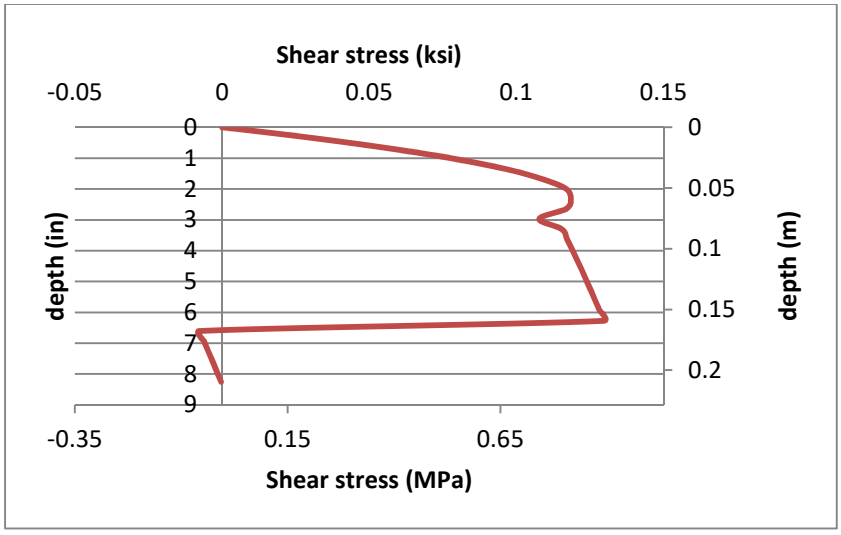

Figure 3-22 Almusallam 1997 shear stress distribution of section two

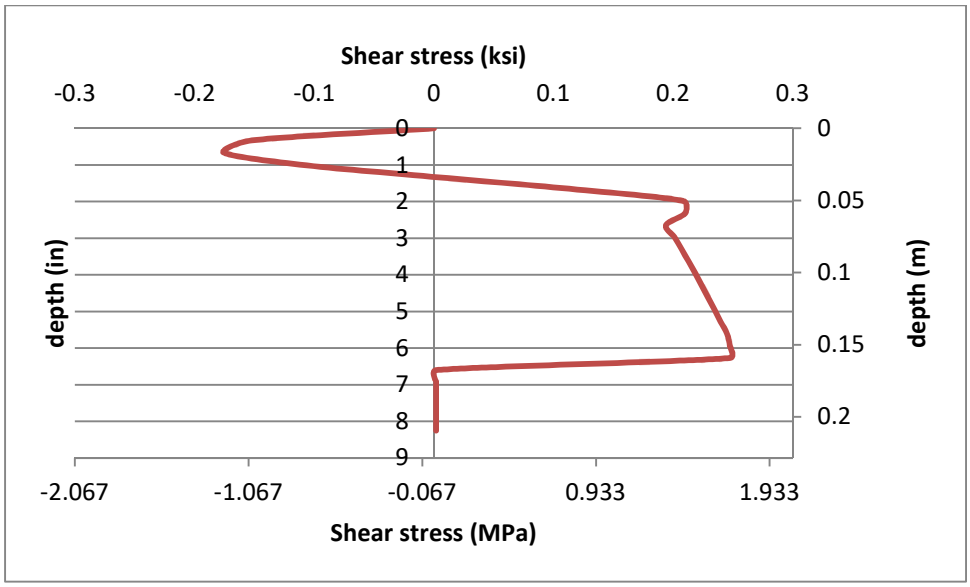

Figure 3-23 Almusallam 1997 shear stress distribution of section three

In section three at the failure load just under the load point, Figure 3-22, it is interesting to observe the opposite change in direction of the shear stresses within the compressive depth. This change is a result of the descending branch of the Hognestad's parabola. Furthermore, the shear stress shows a constant zero region over the bottom end of the beam's height as the tension stiffening model ends at 1.4 times the yielding strain of the steel.

Using Mohr's circle and the calculated axial and shear stresses, the principal stresses were found. Figure 3-23 shows the variation in the maximum/tensile principal stresses for the three given sections. On the other hand, Figure 3-24 presents the variation of the minimum/compressive principal stresses. The two principal stresses were then applied to Kupfer and Gerstle biaxial concrete failure criterion to predict the location of the cracked concrete.

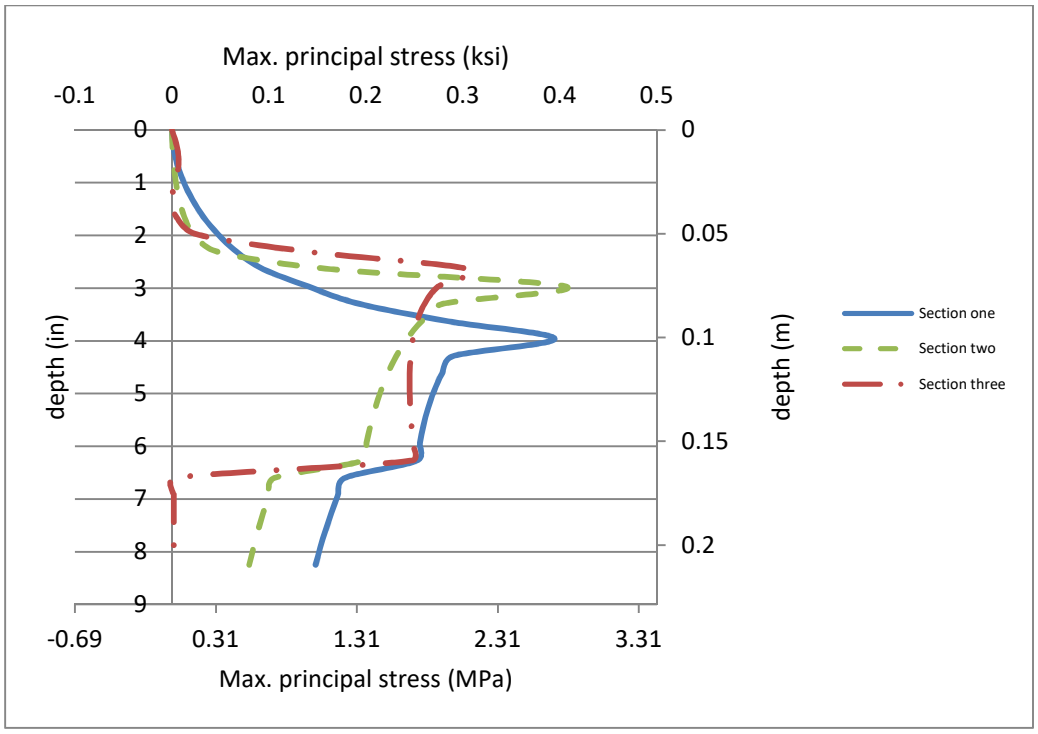

Figure 3-24 Almusallam 1997 tensile principal stresses of the three sections

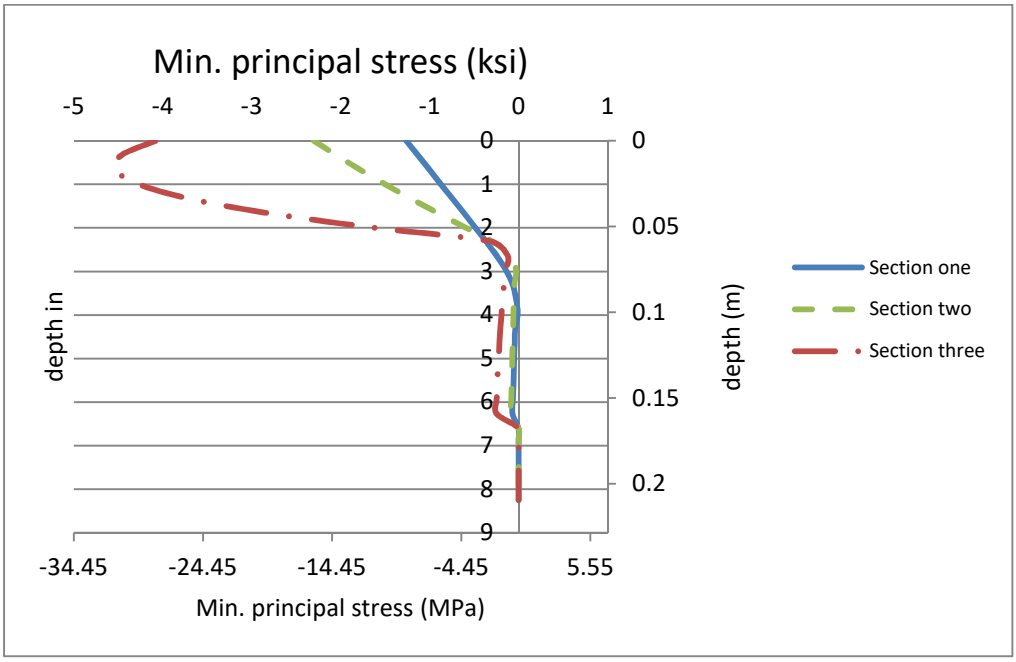

Figure 3-25 Almusallam 1997 compressive principal stresses of the three sections

3.7.2.1 Formation of shear cracks

For each load level, the shear span was divided into a number of sections. Each section was divided into a number of nodes at equal spaces. The proposed analysis was applied on each node to determine if it was cracked. In Figure 3-25, the cracked concrete map was generated using the proposed approach at different load stages. The general directions of the diagonal tension cracks were also compared against the simplified modified compression field theory. The SMCFT predicts the shear crack angle θ as a function of the longitudinal axial strain at the centroid of tensile steel (ε_s).

$$\theta = 29(degree) + 3500\varepsilon_s \leq 75^{\circ} \quad (3.47)$$

Longitudinal axial strain (ε_s) is calculated based on the superimposed effect of the forces in the tension side of the section, as follow

$$\varepsilon_s = \frac{\frac{|M|}{d_v} + 0.5N + V}{A_s E_s} \quad \text{..... (AASHTO 5.8.3.4.2-4)} \quad (3.48)$$

Where

M = moment in k.in

V = shear force in kip

N = axial force, taken as positive if tensile and negative if compressive in kip

A_s = area of non-prestressed steel on the flexural tension side of the section in in.^{2} (mm^2). This is considered to be the area of flexural reinforcement under the original geometric centroid of the section.

d_v = effective shear depth taken as the distance, measured perpendicular to the neutral axis, between the tensile resultant and compressive resultant force due to flexure. It needs not be taken to be less than the greater of $0.9d_e$ or 0.72h in in. (mm).

The SMCFT assumes an average distribution of shear stresses over an area of depth d_v and width b_v. That means the direction of principal stresses doesn't change over the depth. Furthermore, from Figure 3-25, the SMCFT overestimate the angle of the inclination of the cracks at the early stages of the load and underestimates the angle of the diagonal cracks while approaching the ultimate load capacity.

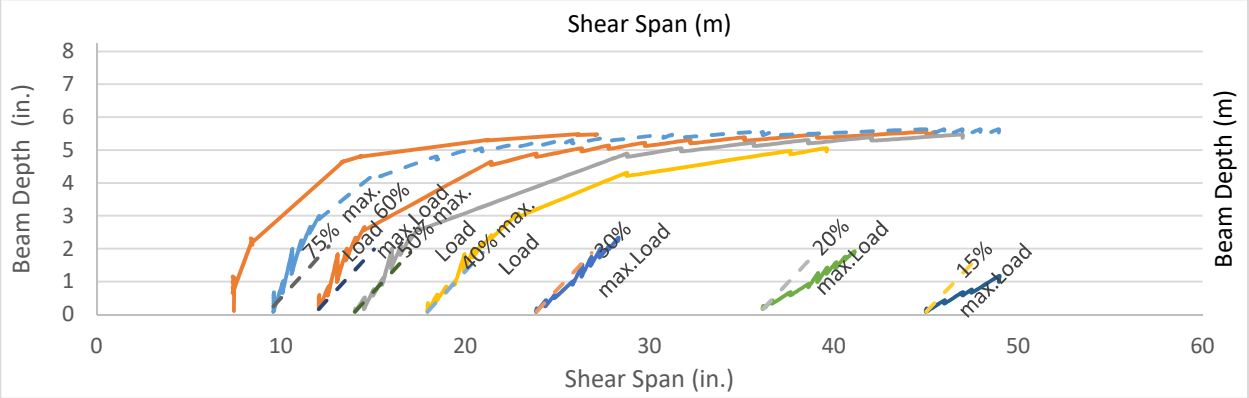

Figure 3-26 Cracks map of different load levels. (SMCFT is presented as dotted line for each load)

3.8 Conclusion

In this study, a novel non-linear formulation was developed using the smeared crack approach. It is used to predict the shear stress profile along the shear span of shallow beams in flexural cracked concrete at all stages of loading up to flexural failure. These shear stress profiles are coupled with the nonlinear axial stress profiles to obtain the principal stress distribution along the shear span. Kupfer and Gerstle failure criterion is used to predict the likely occurrence of new shear-flexural cracks by setting the major principal stress equal to the limit provided by the Kupfer criterion.

It is interesting to observe the prediction of diagonal tension cracks along a curved path, which is expected to be much more accurate than other shear theories that assume a constant shear crack orientation.

3.9 References

AASHTO LRFD Bridge Design Specifications. Washington, D.C. , American Association of State Highway and Transportation Officials, 2014.

Almusallam, T.H., (1997). "Analytical Prediction of Flexural Behavior of Concrete Beams Reinforced by FRP Bars," Journal of Composite Materials, Vol. 31, No. 7, pp 640-657.

Decker, R. A., (2007). "Method of Strengthening Monitored Deficient Bridge". Master Thesis. Department of Civil Engineering, Kansas State University.

Hognestad, E., (1952) "What Do We Know About Diagonal Tension and Web Reinforcement in Concrete? " University of Illinois Engineering Experiment Station, Circular Series No. 64.

Moody,K.G., Viest, I.M., Elstner, R.c., and Hognestad,E. (1954) "Shear Strength of Reinforced Concrete Beams, Part-1 Tests of Simple Beams ". ACI Journal, proceedings Vol. 51, pp. 317-332.

Morsch, E., (1903) "Versuche Uber Schubspannugen in Betoneisentragern," Beton und Eisen Berlin, Vol. 2, No. 4, pp. 269-274.

Rasheed H. A., (1990) "Inelastic Behavior of Reinforced Concrete Frame Structures". M.Sc. Thesis, University of Baghdad, Iraq.

Richart, Frank E., and Larson, L.J., (1928) "An Investigation of Web Stresses in Concrete Beams, Part II, Restrained Beams", University of Illinois Engineering Experiment Station, Bulletin 175.

Talbot, A.N., (1908)" A Test of Three Large Reinforced Concrete Beams" University of Illinois Engineering Experiment Station, Bulletin No. 28.

Talbot, A.N., (1909)" Tests of Reinforced Concrete Beams Resistance to Web Stresses". University of Illinois Engineering Experiment Station, Bulletin No. 30, 1909.

Zwoyer, E.N., and Siess, C.P., (1954) "Ultimate Strength in Shear of Simply-Supported Prestressed Concrete Beams Without Web Reinforcement". ACI Journal, Proceedings Vol. 51, pp. 181-200.

Chapter 4 - Analytical Formulation of Shear Stress Distribution in Cracked Reinforced Concrete Flexural Members

This study is conducted to provide a mechanics-based understanding of the shear stress distribution in cracked reinforced concrete. A rational approach is followed to analytically derive the shear stress profile in shallow reinforced concrete beams based on the smeared crack approach. This approach utilizes the transversal shear differential equation to evaluate the shear stress at any given depth by the variation of the axial stress distribution within an infinitesimal beam segment at that depth. In addition, this study presents a more accurate representation of the change in the strain profile parameters with respect to the sectional applied moment. Furthermore, the dowel action effect is derived to illustrate its significance on the shear stress distribution at various stages of loading.

4.1 Introduction

During the last 50 years, there have been many attempts to predict the shear strength mainly based on experimental results to produce simplified empirical formulas. However, by comparing these different results, significant inconsistencies are realized due to the differences in testing protocols and examined parameters. Therefore, it is vital to present a well-defined mechanics-based approach to accurately predict the shear behavior of flexural members.

The shear failure in reinforced concrete beams stems from a principal tensile stress failure (Morsch 1903). This fact was ignored for many years due to the difficulty in determining the diagonal tension stress in cracked concrete. Mphonde and Frantz (1984) concluded, based on their tests in beams without stirrups, that the ratio of the shear at inclined cracking to the measured shear strength ranges between 0.74-0.97. Therefore, it is difficult to determine the value of the diagonal tensile stress. Also, Bazant and Kazemi (1991) showed that the crack

initiation load is not proportional to the failure load due to the size effect. Moody et al. (1954) described the failure of reinforced concrete beams, subjected to shear, to be composed of two stages. The first stage includes diagonal tension cracking and the second stage terminates at concrete crushing. This shear dominant failure mode was found to be controlled by a smaller (M/Vd) ratio. On the other hand, larger (M/Vd) ratios results in almost pure flexural failure.

The lack of agreement between the researchers on defining a shear failure criterion of reinforced concrete beams rises from the complexity of the mechanics and the number of parameters involved. The diagonal tension or the principal tension stress state is a combination of direct axial stresses and shear stresses in cracked reinforced concrete. The axial stresses in flexural beams are well-defined through the application of basic beam theory and well-known constitutive models. However, the shear stress distribution in cracked concrete is not clearly developed in the literature. There have been some attempts to estimate this shear distribution as an average shear stress over a redefined cross sectional area, which may be known as the modified compression field theory.

A very important deficiency in the literature is the common assumption that the derivative of curvature with respect to x or the derivative of the compression depth with respect to x is taken as a constant. Even though this is done in applications other than shear like moment-curvature analysis and bond slip mechanisms, it is found here that these parameters ($d\varphi/dx$ or $d\varphi/dM$) are nonlinear in nature. Using constant derivatives of curvature from the assumption of trilinear sectional response, for example, yields poor representation of shear stresses in cracked concrete.

In this study, the shear stress profile calculation is introduced, for the first time, in reinforced concrete beams throughout all its stages; pre-cracking, post-cracking and post yielding. The transversal shear differential equation is used to analytically calculate the shear stress at any

given depth based on the smeared crack approach, taking into account the effect of the longitudinal steel and an accurate estimation of the derivatives of the strain profile parameters with respect to the applied moment.

4.2 Sectional Analysis

4.2.1 Materials Constitutive Models

The stress-strain relationships for the concrete and the reinforcement steel are assumed to be independent of each other. The axial stress in steel would be only a result of the axial strain in the steel.

4.2.1.1 Concrete Behavior

The concrete stress-strain relationship is assumed to follow the Hognestad's curve, Equation (4.1), for compressive stresses (f_c) and a linear relationship with a slope equal to the concrete modulus of elasticity (E_c) up to cracking strain (ε_{cr}) in tension, see Figure 4-1. This linear relationship is then followed by a descending curve as a numerical function in (ε_{cr}) and the steel yielding strain (ε_y), Figure 4-1.

$$f_c = f_c' \left(\frac{2\varepsilon_c}{\varepsilon_{c'}} - \left(\frac{\varepsilon_c}{\varepsilon_c'}\right)^2\right) \quad (4\text{-}1)$$

The concrete tensile rupture stress (f_r) is taken as a lower bound equivalent to $5 - 7.5\sqrt{f_c'}$, for light weight concrete this value is reduced by 25%. A linear relationship with a slope equal to the concrete modulus of elasticity (E_c) up to cracking strain (ε_{cr}) in tension is assumed.

The concrete behavior in tension after the cracking strain is described using Equation (4.2). The constants in the equation were calibrated against a large pool of four points bending tests on flexural beams.

$$\frac{f_t}{0.5fr} = 1 - \frac{1}{\ln\left(\frac{1.4\varepsilon_y}{\varepsilon_{cr}}\right)} \ln\left(\frac{\varepsilon_t}{\varepsilon_{cr}}\right) \quad (4\text{-}2)$$

This proposed descending function on the domain ($\varepsilon_{cr} \leq \varepsilon_t \leq 1.4\varepsilon_y$) reaches its peak (0.5 f_r) at the cracking strain (ε_{cr}) and continues to descend till zero when the tensile strain reaches (1.4 ε_y), see Figure 4-2. This function is an average function between the tension softening which exist near the cracking strains and the tension stiffening that activates around the steel location.

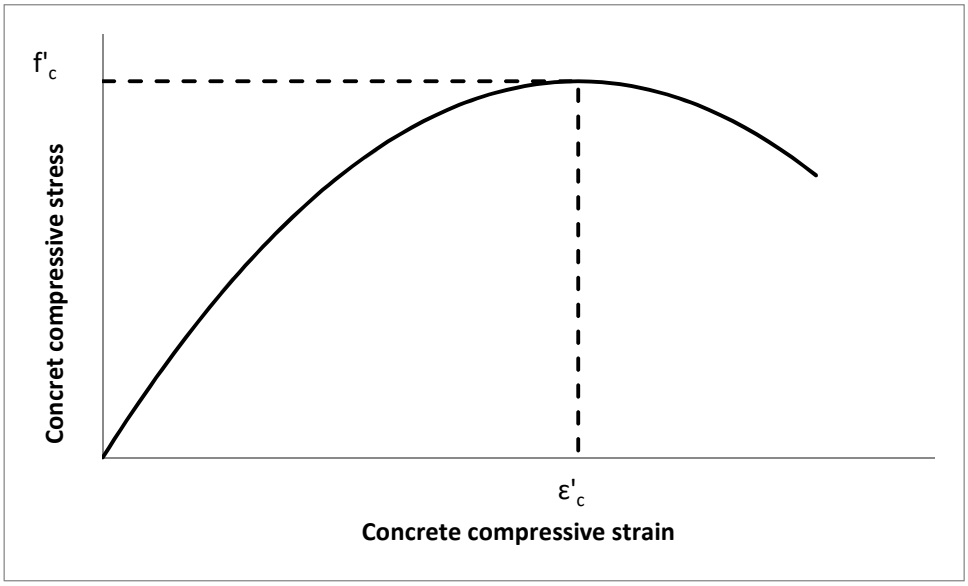

Figure 4-1 Concrete compressive stress-strain curve (Hognestad's Parabola)

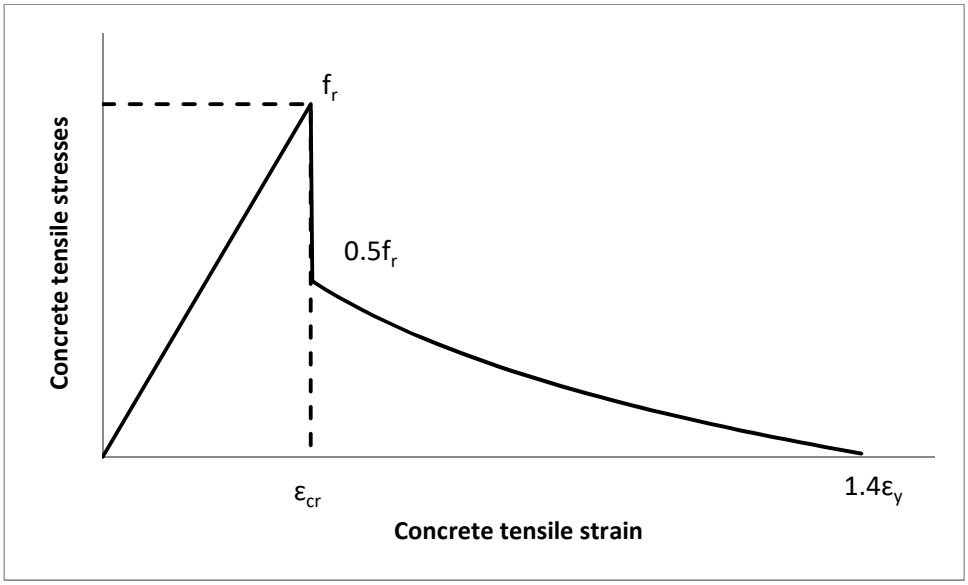

Figure 4-2 Concrete tensile stress-strain curve

4.2.1.2 Steel Behavior

Regarding the steel axial stress-axial strain relationship, a bilinear relationship is assumed in the compressive and the tensile analysis, see Figure 4-3.

$$f_s = E_s \varepsilon_s \leq f_y \quad (4\text{-}3)$$

Where (f_s) is the steel stress corresponding to the axial stress (ε_s), (E_s) is the modulus of elasticity of steel, (f_y) is the yielding stress in steel. The steel is assumed to start hardening after exceeding the yielding strain (f_y) according to the following equation

$$f_s = f_y + E'_s(\varepsilon_s - \varepsilon_y), when\ f_s > f_y \quad (4\text{-}4)$$

(E'_s) is the slope of steel hardening after yielding and it is determined based on the yielding strength (f_y),

Table 4-1 shows the relationship between the estimated (E'_s) and the corresponding (f_y) (Rasheed (1990)).

Table 4-1 The Relationship between the estimated (E'_s) and the corresponding (f_y)

f_y (ksi)	E'_s / E_s
40-45	0.3-0.7%
45-50	0.7-1.2%
50-63	1.2-2.5%

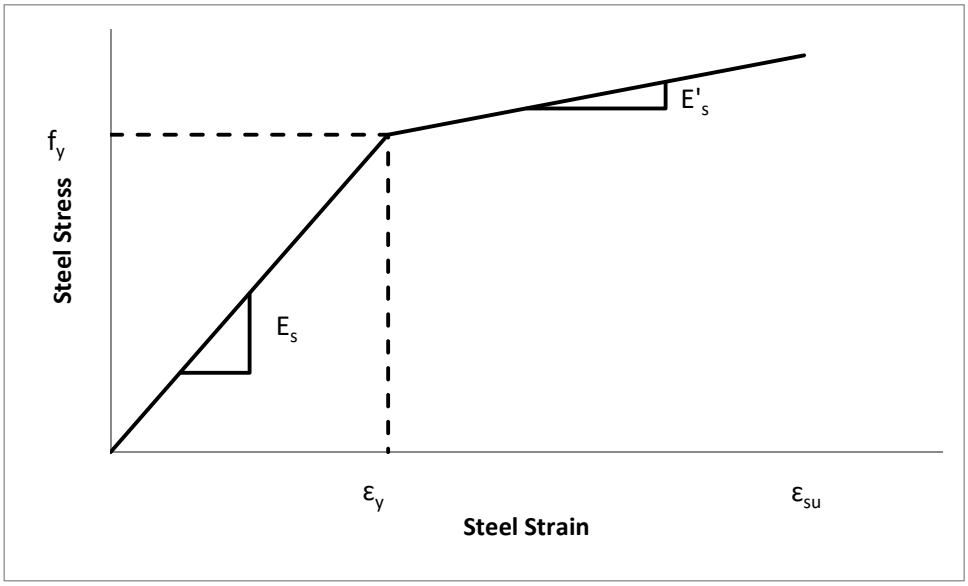

Figure 4-3 Steel stress-strain curve

4.3 Trilinear Approach

The moment-curvature (M vs. φ) response and the moment-extreme compression fiber strain (M vs. ε_{cf}) response could be estimated as a trilinear relationship when analyzing the overall sectional behavior (Rasheed et al. 2013), see Figure 4-4 . The first linear part is the pre-cracking zone, where the maximum tensile strain doesn't exceed the cracking strain of the concrete (ε_{cr}).

The second linear region starts with the appearance of the first crack and extends till the yielding of the tensile steel. Finally, the third linear region continues until the crushing of concrete at a maximum compressive strain equals 0.003. Three well-defined boundary points are used to fully generate the sectional response of the beam; the cracking limit $(M, \varphi, \varepsilon_{cf})_{cr}$, the yielding limit $(M, \varphi, \varepsilon_{cf})_{y}$ and the failure point $(M, \varphi, \varepsilon_{cf})_{n}$. The cracking limit is straight forward using the linear distribution of stresses, Equation (4.5).

$$M_{cr} = \frac{f_r I_{gt}}{\bar{y}} \tag{4-5}$$

Where, (I_{gt}) is the gross transformed moment of inertia of the section and ($\bar{y}$) is the uncracked neutral axis location measured from the maximum tensile fiber. The curvature of the section at first cracking (φ_{cr}) is then calculated as follow

$$\varphi_{cr} = \frac{M_{cr}}{EI_{gt}} \tag{4-6}$$

The yielding limit considers the nonlinear behavior of the Hognestad's parabola. The Concrete compressive force is expressed in terms of (α), which is used to transform the nonlinear relationship into an equivalent rectangular block.

$$\alpha = \frac{\int_0^{\varepsilon_{cf}} \sigma_c d\varepsilon_c}{f_c' \varepsilon_{cf}} = \frac{\int_0^{\varepsilon_{cf}} f_c' \left(2\frac{\varepsilon_c}{\varepsilon_c'} - \left(\frac{\varepsilon_c}{\varepsilon_c'}\right)^2\right) d\varepsilon_c}{f_c' \varepsilon_{cf}} = \frac{\varepsilon_{cf}}{\varepsilon_c'} - \frac{\varepsilon_{cf}^2}{3{\varepsilon_c'}^2} \tag{4-7}$$

From the equilibrium of forces on the cross section, the compression depth at the yielding point (cy) is computed.

$$\sum F_x = 0 \rightarrow \alpha f_c' b c_y + A_s' f_s' = A_s f_y \tag{4-8}$$

$$\varphi_y = \frac{\varepsilon_y}{d - c_y} \tag{4-9}$$

$$\varepsilon_{cf_y} = \varphi_y c_y \tag{4-10}$$

The point of action of the concrete compressive force, measured from the maximum compressive fiber, could be calculated as a fraction of the compression depth ($\gamma\, c_y$).

$$\gamma = 1 - \frac{\int_0^{\varepsilon_{cf}} \varepsilon_c . f_c . d\varepsilon_c}{\varepsilon_{cf} \int_0^{\varepsilon_{cf}} f_c . d\varepsilon_c} = \frac{\frac{1}{3} - \frac{\varepsilon_{cf}}{12\,\varepsilon_c'}}{1 - \frac{\varepsilon_{cf}}{3\varepsilon_c'}} \quad (4\text{-}11)$$

The yielding moment (M_y) is then computed by summing the moments about the point of concrete compression resultant force.

$$M_y = A_s f_y \left(d - \gamma c_y\right) + A_s' f_s' (\gamma c_y - d') \quad (4\text{-}12)$$

Similarly, the failure point limit $(M, \varphi, \varepsilon cf)_n$ is calculated.

The strain profile parameters, at any section namely the curvature (φ) and the maximum compressive strain (ε_{cf}), are retrieved from the trilinear approach through linear interpolation based on the applied moment

$$if\ M_{cr} < M < M_y$$

$$\varphi = \frac{M - M_{cr}}{M_y - M_{cr}} \left(\varphi_y - \varphi_{cr}\right) + \varphi_{cr} \quad (4\text{-}13)$$

$$if\ M_y < M < M_n$$

$$\varphi = \frac{M - M_y}{M_n - M_y} \left(\varphi_n - \varphi_y\right) + \varphi_y \quad (4\text{-}14)$$

Similarly, the maximum compressive strain (ε_{cf}) is computed

$$if\ M_{cr} < M < M_y$$

$$\varepsilon_{\mathrm{cf}} = \frac{M - M_{cr}}{M_y - M_{cr}} \left(\varepsilon_{\mathrm{cf}_y} - \varepsilon_{\mathrm{cf}_{cr}}\right) + \varepsilon_{\mathrm{cf}_{cr}} \quad (4\text{-}15)$$

$$if\ M_y < M < M_n$$

$$\varepsilon_{\mathrm{cf}} = \frac{M - M_y}{M_n - M_y} \left(\varepsilon_{\mathrm{cf}_n} - \varepsilon_{\mathrm{cf}_y}\right) + \varepsilon_{\mathrm{cf}_y} \quad (4\text{-}16)$$

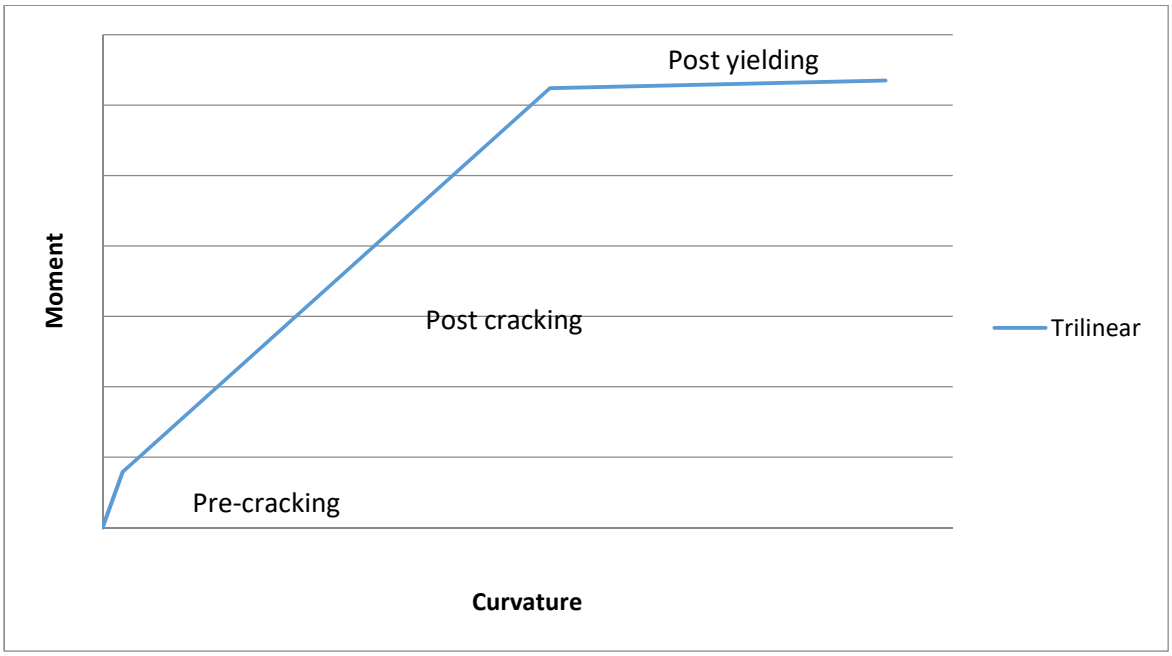

Figure 4-4 Typical moment vs. curvature trilinear approach

4.4 Sectional Forces

In this Section, the axial forces generated at any given depth are calculated using the material constitutive models for both concrete and steel under compressive or tensile stresses. The axial forces are found by integrating the material stress profile over the given area. This step is necessary to develop the stresses distribution at any point along the height of the beam.

4.4.1 Compressive Concrete Force

The force induced in concrete within the compression depth of the beam (C_c) is computed by integrating Hognestad's parabola over the depth from the top of the beam's section to the specific depth (d_c).

$$C_c = \int_{c-d_c}^{c} f_c . b\, dy = \int_{c-d_c}^{c} b f_c' \left(\frac{2\varepsilon_c}{\varepsilon_c'} - \left(\frac{2\varepsilon_c}{\varepsilon_c'} \right)^2 \right) dy \quad (4\text{-}17)$$

Where, (y) is measured from the top of the section and (ε_c) is the compressive concrete strain.

$$C_c = b f_c' \frac{\varphi}{\varepsilon_c'} \left(y^2 - \frac{\varphi}{3} \frac{y^3}{\varepsilon_c'} \right) \Big|_{c-d_c}^{c} \quad (4\text{-}18)$$

4.4.2 Compressive Steel Force

The compressive steel force (C_s) is a direct linear relationship with the corresponding compressive steel strain (ε_s'). This relationship was driven based on the assumption of the bilinear behavior of the steel analysis taking into account the concrete compressive stress deducted due to the existence of the steel rebar .

$$C_s = A_s' f_s' - A_s' f_c' \left(\left(2\frac{\varepsilon_s'}{\varepsilon_c'} - \left(\frac{\varepsilon_s'}{\varepsilon_c'}\right)^2\right)\right) \quad (4\text{-}19)$$

4.4.3 Tensile Concrete Forces

The concrete tensile stresses are divided into two main profiles. The first profile is a linear function up to the concrete cracking strain (ε_{cr}) with a slope equal to the concrete modulus of elasticity (E_c). The tensile force within this range (T_{c1}) at a given depth (d_t) measured from the neutral axis is calculated as follow

$$T_{c_1} = \int_0^{d_t} f_t . b \, dy \quad (4\text{-}20)$$

Where, (y) and (d_t) are measured from the neutral axis.

$$T_{c_1} = \frac{bE_c \varphi d_t^2}{2} \quad (4\text{-}21)$$

The second concrete tensile stress profile starts at the concrete cracking strain (ε_{cr}) and extends up to 1.4 times the steel yielding strain ($1.4\varepsilon_y$). At any depth (d_t) measured from the neutral axis, The second concrete tensile force (T_{c2}) is measured as follow

$$T_{c2} = \int_{d_{cr}}^{d_t} b f_t dy \quad (4\text{-}22)$$

$$T_{c2} = b \int_{d_{cr}}^{d_t} 0.5 f_r - \frac{0.5 f_r}{\ln\left(\frac{1.4\varepsilon_y}{\varepsilon_{cr}}\right)} \ln\left(\frac{\varepsilon_t}{\varepsilon_{cr}}\right) dy \quad (4\text{-}23)$$

Where, (y) is measured from the neutral axis.

$$T_{c2} = b\left[\frac{-0.5 f_r}{\ln\left(\frac{1.4\varepsilon_y}{\varepsilon_{cr}}\right)} \left(y\ln(\varphi) + y ln(y) - y - y ln(\varepsilon_{cr})\right) + 0.5 f_r y\right] \Big|_{\varepsilon_{cr}/\varphi}^{d_t} \quad (4\text{-}24)$$

4.4.4 Tensile Steel Force

The tensile steel force (T_s), calculated at the tensile reinforcement level, is evaluated according to the following equations

$$T_s = A_s E_s \varepsilon_s - A_s f_{ct} \, , when \; f_s \leq f_y \tag{4-25}$$

$$T_s = A_s(f_y + E'_s(\varepsilon_s - \varepsilon_y)) - A_s f_{ct} when \; f_s > f_y \tag{4-26}$$

Where, f_{ct} is a function of the tensile steel strain (ε_s) and is taken from the un-cracked or post-cracked parts of the concrete tensile constitutive functions. Note that $f_{ct}(\varepsilon_s) = 0, \text{when } \varepsilon_s \geq \varepsilon_{tu}$.

4.5 Differential Sectional Analysis

4.5.1 Shear Stress Differential Equation

Shear stress distribution over a shallow beam depth is formulated through the change of axial forces acting on the beam cross section. Considering an infinitesimal element with length dx of the beam, the differential bending moment acting over dx is dM, Figure 4-5. At any given depth, the equilibrium of forces in the longitudinal direction is satisfied through the longitudinal shear τ_{yx} at that depth, Figure 4-6. Also from equilibrium, the longitudinal shear is equal to the transversal shear τ_{xy}.

$$\sum F_x = 0 \tag{4-27}$$

$$\int \sigma' . dA - \int \sigma'' . dA - \tau(b . dx) = 0 \tag{4-28}$$

$$F' - F'' - \tau(b . dx) = 0 \tag{4-29}$$

$$dF - \tau(b . dx) = 0 \tag{4-30}$$

$$\tau = \frac{1}{b} \frac{dF(\varphi,\varepsilon)}{dx} \tag{4-31}$$

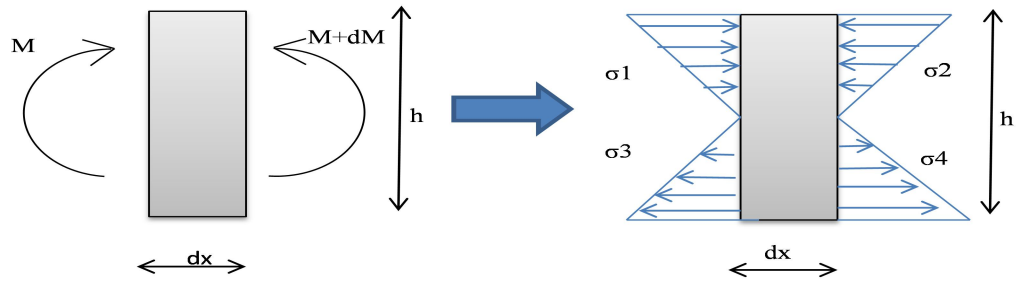

Figure 4-5 Axial stress distribution over an infinitesimal element dx

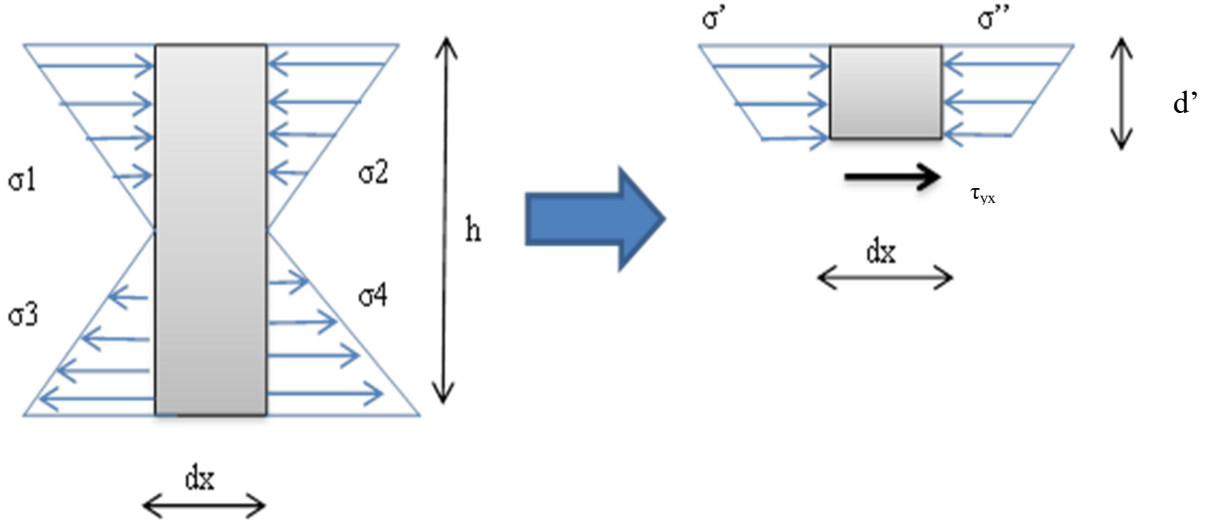

Figure 4-6 Axial stress distribution over an infinitesimal element dx and depth d'

4.5.2 Shear Stress evaluation at any depth

For each load level and a specific section along the shear span, the shear stress at any given depth is the summation of the shear stress contribution of the concrete and steel above the desired depth. For example, the shear stress at the neutral axis would be the sum of the shear stress due to the compressive concrete contribution within the compression zone plus the the shear stress due to the compressive steel contribution if any. In this section, shear stresses

induced by compressive or tensile concrete as well as compressive or tensile steel is analytically derived for each individual one. Using Equation (4.31), the shear stress is the derivative of the axial forces above its depth with respect of x (beam length direction) divided by the width of the cross section.

4.5.2.1 Compressive concrete contribution

The shear stresses induced by the compressive concrete (τ_{cc}) is the derivative of Equation (4.18).

$$\tau_{cc} = \frac{1}{b}\frac{d(C_c)}{dx} = \frac{1}{b}\frac{d}{dx}\left[bf_c'\frac{\varphi}{\varepsilon_c'}\left(y^2 - \frac{\varphi}{3}\frac{y^3}{\varepsilon_c'}\right)\ \Big|_{c-d_c}^{c}\right] \quad (4\text{-}32)$$

Where, (y) is measured from the neutral axis, and dc is measured from the top of the section.

$$\tau_{cc} = f_c'\left(\frac{2d_c}{\varepsilon_c'}\frac{d\varepsilon_{cf}}{dx} - \frac{d_c^2}{\varepsilon_c'}\frac{d\varphi}{dx} - \frac{3d_c}{3\varepsilon_c'^2}\frac{d\varepsilon_{cf}^2}{dx} + \frac{3d_c^2}{3\varepsilon_c'^2}\frac{d(\varphi\varepsilon_{cf})}{dx} - \frac{d_c^3}{3\varepsilon_c'^2}\frac{d(\varphi)^2}{dx}\right) \quad (4\text{-}33)$$

This equation above indicates that the shear stress due to compressive concrete forces is a function of the material properties, strain profile parameters at a specific section and the derivative of these strain profile parameters with respect to x.

4.5.2.2 Compressive Steel Contribution

In a similar manner, the shear stress contribution for the compressive steel (τ_{cs}) is the derivative of the compressive force in the compression reinforcement. Using Equation (4.19), the shear stress is calculated as follow

$$\tau_{cs} = \frac{1}{b}\frac{d(C_s)}{dx} = \frac{1}{b}\frac{d}{dx}\left[A_s'f_s' - A_s'f_c'\left(2\frac{\varepsilon_s'}{\varepsilon_c'} - \left(\frac{\varepsilon_s'}{\varepsilon_c'}\right)^2\right)\right] \quad (4\text{-}34)$$

$$\tau_{cs} = A_s'\left(E_s\frac{d\varepsilon_{cf}}{dx} - E_s\frac{d\varphi}{dx}d' - \frac{f_c'}{\varepsilon_c'}\left(2\frac{d\varepsilon_{cf}}{dx} - 2\frac{d\varphi}{dx}d' - \frac{2\varepsilon_{cf}}{\varepsilon_c'}\frac{d\varepsilon_{cf}}{dx} + \frac{2d'}{\varepsilon_c'}\frac{d(\varphi\varepsilon_{cf})}{dx} - \frac{\varphi d'^2}{\varepsilon_c'}\frac{d\varphi}{dx}\right)\right) \quad (4\text{-}35)$$

4.5.2.3 Tensile concrete contribution

The shear stress due to the tensile concrete is divided into two main profiles as described in the material constitutive models. The shear stress in the first profile (τ_{tc1}) which covers a range up to

concrete cracking strain is calculated using this equation

$$\tau_{tc1} = \frac{1}{b}\frac{d(T_{c1})}{dx} = \frac{1}{b}\frac{d}{dx}\left[\frac{bE_c\varphi d_t^2}{2}\right] \quad (4\text{-}36)$$

Where, d_t is measured from the neutral axis downwards.

$$\tau_{tc1} = E_c\left((d_t\varphi)\left(-\frac{d\varepsilon_{cf}}{dx}\frac{1}{\varphi} + \frac{\varepsilon_{cf}}{\varphi^2}\frac{d\varphi}{dx}\right) + \left(\frac{d_t^2}{2}\right)\frac{d\varphi}{dx}\right) \quad (4\text{-}37)$$

The shear stress due to the second tensile concrete profile (τ_{tc2}) is the derivative of Equation (4.24)

$$\tau_{tc2} = \frac{1}{b}\frac{d(T_{c2})}{dx} = \frac{1}{b}\frac{d}{dx}\left[b\left[\frac{-0.5f_r}{\ln\left(\frac{1.4\varepsilon_y}{\varepsilon_{cr}}\right)}\left(y\ln(\varphi) + y\ln(y) - y - y\ln(\varepsilon_{cr})\right) + 0.5f_r y\right]\Big|_{\varepsilon_{cr}/\varphi}^{d_t}\right] \quad (4\text{-}38)$$

Let, $k = \frac{0.5f_r}{\ln\left(\frac{1.4\varepsilon_y}{\varepsilon_{cr}}\right)}$ (4-39)

$$\tau_{tc2} = \left[\left(R\frac{\varepsilon_{cf}}{\varphi^2} + R\frac{\varepsilon_{cr}}{\varphi^2} - k\frac{\varepsilon_{cf}}{\varphi^2}(\ln(d_t\varphi) + 1) - \frac{k(d_t)}{\varphi} - k\frac{\varepsilon_{cr}}{\varphi^2}\ln(\varepsilon_{cr})\right)\frac{d\varphi}{dx} + \left(-\frac{R}{\varphi} + \frac{k}{\varphi}(\ln(d_t\varphi) + 1)\right)\frac{d\varepsilon_{cf}}{dx}\right] \quad (4\text{-}40)$$

Where, $R = \left(0.5f_r + k + k\ln(\varepsilon_{cr})\right)$ (4-41)

4.5.2.4 Tension Steel Contribution

Similarly, The shear stress (τ_{ts}) generated due to the change in the steel tensile forces is calculated as follow

$$\tau_{ts} = \frac{1}{b}\frac{d(T_s)}{dx} = \frac{1}{b}\frac{d}{dx}\left[A_s E_s \varepsilon_s - A_s f_{ct}\right] \quad (4\text{-}42)$$

Where, f_{ct} is the tensile axial stress that must be subtracted from the concrete contribution due to the bar hole. It is defined below as a function of the tensile steel strain (ε_s) and is taken from the un-cracked (linear variation) or post-cracked (tension stiffening) parts of the concrete tensile

constitutive functions due to the perfect bond assumption. Note that $f_{ct}(\varepsilon_s) = 0, \text{when } \varepsilon_s \geq 1.4\varepsilon_y$.

For pre-yielding condition $f_s \leq f_y$

$$\tau_{ts} = A_s\left(-E_s\frac{d\varepsilon_{cf}}{dx} + E_s\frac{d\varphi}{dx}d\right) \tag{4-43}$$

For post-yielding condition $f_s > f_y$

$$\tau_{ts} = A_s\left(-(E_s + E_s')\frac{d\varepsilon_{cf}}{dx} + (E_s + E_s')\frac{d\varphi}{dx}d\right) \tag{4-44}$$

The subtracted concrete stress f_{ct} due to the existence of steel rebar has three main cases. The first case occurs when the steel bars are located within the first zone of tensile concrete $\varepsilon_s < \varepsilon_{cr}$ .The Second case happens when the steel bars are located within the second tensile concrete zone $\varepsilon_{cr} < \varepsilon_s \leq 1.4\varepsilon_y$. After that, $f_{ct} = 0$.

The shear stress in equation (4.42), when the bars are within the uncracked zone, has the following term

$$\frac{d(f_{ct})}{dx} = \frac{d}{dx}[A_sE_c\varepsilon_s] = AsE_c(-E_s\frac{d\varepsilon_{cf}}{dx} + E_s\frac{d\varphi}{dx}d) \tag{4-45}$$

While the shear stress in equation (4.42), when the bars are within the tension stiffening zone, has the following term

$$\frac{d(f_{ct})}{dx} = \frac{d}{dx}\left[0.5f_r - \frac{0.5f_r}{\ln(\frac{1.4\varepsilon_y}{\varepsilon_{cr}})}\ln\left(\frac{\varepsilon_t}{\varepsilon_{cr}}\right)\right] = A_s\frac{k}{\varphi d - \varepsilon_{cf}}(\frac{d\varepsilon_{cf}}{dx} - \frac{d\varphi}{dx}d) \tag{4-46}$$

In order to evaluate the shear stress at any given depth measured from the top of the section, all shear stress contributions from concrete and steel have to be considered. In general, the shear stress at a location just above the tensile steel level is equal to the superposition of the compressive concrete contribution, compressive steel contribution and tensile concrete

contribution, taking into account a positive sign for the compressive contribution and a negative sign for tensile contribution.

$$\tau\,(d) = \tau_{cc} + \tau_{cs} - \tau_{tc1} - \tau_{tc2} \quad (4\text{-}47)$$

4.5.3 The derivative of strain profile parameters with respect to distance along the shear span

Equations (4.32)-(4.47) share the same four main categories of parameters. The first category involves the material properties (e.g. f'_c, ε'_c, f_y, …etc.), the second category includes the geometrical properties (e.g. h, d and d'). The third category contains the parameters that define the strain profile at a given section (e.g. the curvature φ, the maximum compressive strain ε_{cf} , and the compression depth c), which could be evaluated using a nonlinear sectional analysis or a trilinear sectional approach as shown in this study. The fourth category encompasses the derivative of the strain profile parameters with respect to x (e.g. $\frac{d\varphi}{dx}$ and $\frac{d\varepsilon_{cf}}{dx}$). It is important to note that these derivatives can be made independent of x using the chain rule (e.g. $\frac{d\varphi}{dx} = \frac{d\varphi}{dM}\frac{dM}{dx} = \frac{d\varphi}{dM}V$ and $\frac{d\varepsilon_{cf}}{dx} = \frac{d\varepsilon_{cf}}{dM}\frac{dM}{dx} = \frac{d\varepsilon_{cf}}{dM}V$). These two parameters appear as a result of using the shear differential equation, Equation (4.31). Furthermore and unlike many previous, assuming a constant derivative of the strain profile parameters for this application proves not accurate, See Figure 7 and 8. These two figures show the derivatives of the curvature (φ) and the maximum compressive strain (ε_{cf}) with respect to x computed numerically.

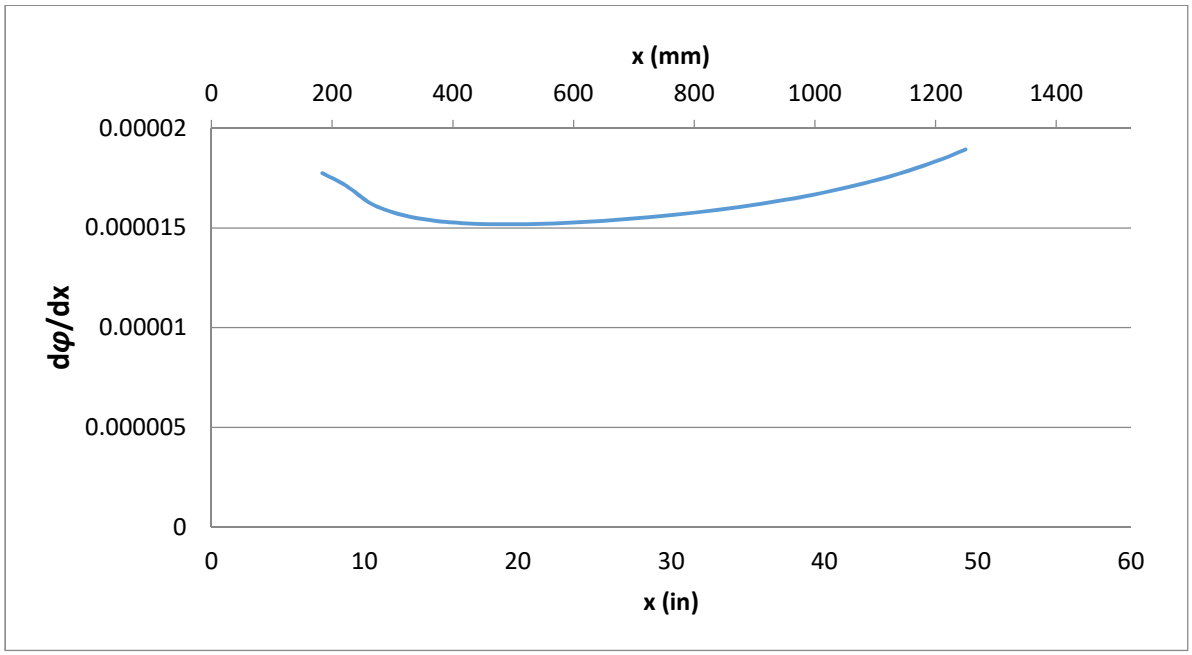

Figure 4-7 The numerical derivative of the cross section curvature with respect to x using example one below (post cracking zone)

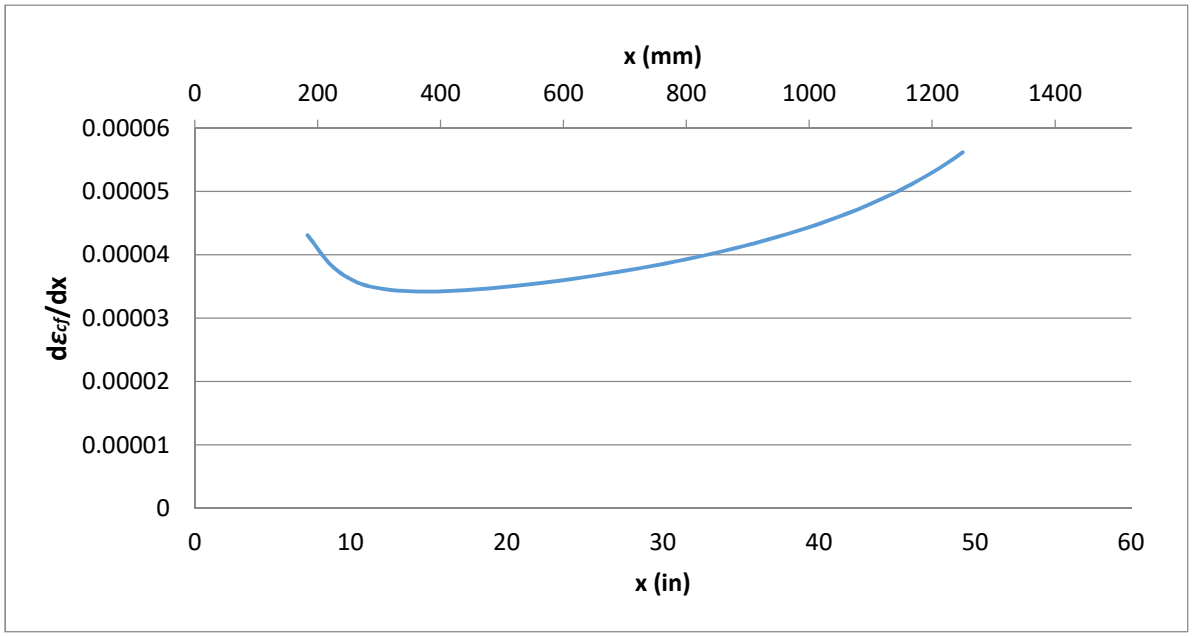

Figure 4-8 The numerical derivative of maximum compressive strain with respect to x using example one below (post cracking zone)

Thus, it was vital to accurately calculate these derivatives. Two mathematical conditions were considered to accurately predict the derivatives $\frac{d\varphi}{dx}$ and $\frac{d\varepsilon_{cf}}{dx}$. The first condition was derived using

the zero shear boundary condition at the soffit of the beam, $\tau\,(\text{at}\,d = h) = 0$. The second condition comes from the fact that the integral of the shear stresses over the cross sectional area has to equal the internally applied shear force $\int_A \tau\,.\,dA = V$.

4.5.3.1 Condition One The zero shear boundary condition at the soffit of the beam

Using Equations (4.32)-(4.47), the shear stress, at the soffit of the beam, may be calculated by considering the full contributions for concrete and steel in tension and compression.

Compressive concrete contribution

The shear stress induced by the compressive concrete (τ_{cc}) at depth equal to the height of the beam would consider the full capacity of the compression zone and is calculated as follow

$$\tau_{cc} = \frac{1}{b}\frac{d(C_c)}{dx} = \frac{1}{b}\frac{d}{dx}\left[bf'_c\frac{\varphi}{\varepsilon'_c}\left(y^2 - \frac{\varphi}{3}\frac{y^3}{\varepsilon'_c}\right)\Big|_0^c\right] \tag{4-48}$$

Where, (y) is measured from the neutral axis.

$$\tau_{cc} = f'_c\left(\frac{2c}{\varepsilon'_c}\frac{d\varepsilon_{cf}}{dx} - \frac{c^2}{\varepsilon'_c}\frac{d\varphi}{dx} - \frac{3c}{3\varepsilon'^2_c}\frac{d\varepsilon^2_{cf}}{dx} + \frac{3c^2}{3\varepsilon'^2_c}\frac{d(\varphi\varepsilon_{cf})}{dx} - \frac{c^3}{3\varepsilon'^2_c}\frac{d(\varphi)^2}{dx}\right) \tag{4-49}$$

Compressive Steel Contribution

The shear stress from the compressive steel contribution (τ_{cs}) is taken directly from Equations (4.34) and (4.35).

Tensile concrete contribution

The shear stress due to the tensile concrete is divided into two main zone contributions as described earlier. The shear stress in the first zone (τ_{tc1}) which covers a range up to concrete cracking strain is calculated using these equations

$$\tau_{tc1} = \frac{1}{b}\frac{d(T_{c1})}{dx} = \frac{1}{b}\frac{d}{dx}\left[\frac{bE_c\varphi y^2}{2}\Big|_0^{d_t}\right] \tag{4-50}$$

Where, d_t is measured from the neutral axis and equal to $d_t = d_{cr} = \frac{\varepsilon_{cr}}{\varphi}$.

$$\tau_{tc1} = E_c\left((d_{cr}\varphi)(-\frac{d\varepsilon_{cf}}{dx}\frac{1}{\varphi} + \frac{\varepsilon_{cf}}{\varphi^2}\frac{d\varphi}{dx}) + \left(\frac{d_{cr}^2}{2}\right)\frac{d\varphi}{dx}\right) \quad (4\text{-}51)$$

The shear stress due to the tension stiffening concrete zone (τ_{tc2}) is found as follow

$$\tau_{tc2} = \frac{1}{b}\frac{d(T_{c2})}{dx} = \frac{1}{b}\frac{d}{dx}[b[\frac{-0.5f_r}{\ln\left(\frac{1.4\varepsilon_y}{\varepsilon_{cr}}\right)}\left(y\ln(\varphi) + y\ln(y) - y - y\ln(\varepsilon_{cr})\right) + 0.5f_r y]\Big|_{\varepsilon_{cr}/\varphi}^{d_t}] \quad (4\text{-}52)$$

Let, $k = \frac{0.5f_r}{\ln\left(\frac{1.4\varepsilon_y}{\varepsilon_{cr}}\right)}$

$$\tau_{tc2} = [\left(R\frac{\varepsilon_{cf}}{\varphi^2} + R\frac{\varepsilon_{cr}}{\varphi^2} - k\frac{\varepsilon_{cf}}{\varphi^2}(\ln(d_t\varphi) + 1) - \frac{k(d_t)}{\varphi} - k\frac{\varepsilon_{cr}}{\varphi^2}\ln(\varepsilon_{cr})\right)\frac{d\varphi}{dx} + \left(-\frac{R}{\varphi} + \frac{k}{\varphi}(\ln(d_t\varphi) + 1)\right)\frac{d\varepsilon_{cf}}{dx}] \quad (4\text{-}53)$$

Where ,$R = \left(0.5f_r + k + k\ln(\varepsilon_{cr})\right)$, and d_t is measured from the neutral axis and equals to $d_t = h - c$ if the concrete tensile constitutive model extends beyond the full depth of the section (i.e. $h - c \leq \frac{1.4\varepsilon_y}{\varphi}$), otherwise $d_t = \frac{1.4\varepsilon_y}{\varphi}$.

Tension Steel Contribution

The shear stress (τ_{ts}) generated due to the steel tensile forces is taken directly from Equations (43) and (46).

Summing all concrete and steel contributions yields to the shear stress at the soffit of the beam and it is equated to zero at the free surface.

$$\tau\,(d = h) = \tau_{cc} + \tau_{cs} - \tau_{tc1} - \tau_{tc2} - \tau_{ts} = 0 \quad (4\text{-}54)$$

The previous equation could be simplified into the following form

$$\tau\,(d = h) = q_{11}\frac{d\varphi}{dx} + q_{12}\frac{d\varepsilon_{cf}}{dx} = 0 \quad (4\text{-}55)$$

Where q_{11} and q_{12} are constants multiplying the derivatives in equation (4.54).

4.5.3.2 Condition Two Equating the integral of shear stresses across the section to shear force

By integrating the shear stress distribution over the depth of the section, a second equation/condition is found in terms of $\frac{d\varphi}{dx}$ and $\frac{d\varepsilon_{cf}}{dx}$. The integral was computed using the superposition technique. The shear stress profile for each contribution (concrete /steel-tension/compression) is determined using the set of Equations (4.32)-(4.47) and then the integral of these contributions is calculated for the whole height of the beam. The summation of these integrals equals to the shear force divided by the beam width (b).

Compressive Concrete Contribution

Figure 4-9 shows a typical shear stress distribution induced by the forces in the compressive concrete. The first part of this distribution is variable over the compression zone, which represents Equation (4.32). The second part is constant and equals to the shear stress at a depth equals to the compression depth. This part extends from the end of the compression zone till the soffit of the beam. The integral of this full profile, Figure 4-9, (A_{cc}) is calculated as follow

$$A_{cc} = \int_0^c \text{part 1}.\,dy + \int_c^h \text{part 2}.\,dy \tag{4-56}$$

$$A_{cc} = \int_0^c [f'_c \left(\frac{2d_c}{\varepsilon'_c}\left(\frac{d\varepsilon_{cf}}{dx}\right) - \frac{d_c^2}{\varepsilon'_c}\left(\frac{d\varphi}{dx}\right) - \frac{3d_c}{3\varepsilon_c'^2}\left(2\varepsilon_{cf}\,\frac{d\varepsilon_{cf}}{dx}\right) + \frac{3d_c^2}{3\varepsilon_c'^2}\left(\varepsilon_{cf}.\frac{d\varphi}{dx} + \varphi.\frac{d\varepsilon_{cf}}{dx}\right) - \frac{d_c^3}{3\varepsilon_c'^2}\left(2\varphi\,\frac{d\varphi}{dx}\right)\right)].\,dy + \int_c^{h-c} [f'_c \left(\frac{2c}{\varepsilon'_c}\left(\frac{d\varepsilon_{cf}}{dx}\right) - \frac{c^2}{\varepsilon'_c}\left(\frac{d\varphi}{dx}\right) - \frac{3c}{3\varepsilon_c'^2}\left(2\varepsilon_{cf}\,\frac{d\varepsilon_{cf}}{dx}\right) + \frac{3c^2}{3\varepsilon_c'^2}\left(\varepsilon_{cf}.\frac{d\varphi}{dx} + \varphi.\frac{d\varepsilon_{cf}}{dx}\right) - \frac{c^3}{3\varepsilon_c'^2}\left(2\varphi\,\frac{d\varphi}{dx}\right)\right)].\,dy \tag{4-57}$$

$$A_{cc} = f'_c[\left(\frac{c^2}{\varepsilon'_c} - \frac{c^2}{\varepsilon_c'^2}\varepsilon_{cf} + \frac{c^3}{3\varepsilon_c'^2}\varphi\right)\frac{d\varepsilon_{cf}}{dx} + (-\frac{c^3}{3\varepsilon'_c} + \frac{c^3}{3\varepsilon_c'^2}\varepsilon_{cf} - \frac{c^4}{6\varepsilon_c'^2}\varphi)\frac{d\varphi}{dx}] + f'_c\left(\frac{2c}{\varepsilon'_c}\left(\frac{d\varepsilon_{cf}}{dx}\right) - \frac{c^2}{\varepsilon'_c}\left(\frac{d\varphi}{dx}\right) - \frac{3c}{3\varepsilon_c'^2}\left(2\varepsilon_{cf}\,\frac{d\varepsilon_{cf}}{dx}\right) + \frac{3c^2}{3\varepsilon_c'^2}\left(\varepsilon_{cf}.\frac{d\varphi}{dx} + \varphi.\frac{d\varepsilon_{cf}}{dx}\right) - \frac{c^3}{3\varepsilon_c'^2}\left(2\varphi\,\frac{d\varphi}{dx}\right)\right)(h-c) \tag{4-58}$$

$$A_{cc} = \text{constant } a_1 \frac{d\varphi}{dx} + \text{constant } b_1 \frac{d\varepsilon_{cf}}{dx} \quad (4\text{-}59)$$

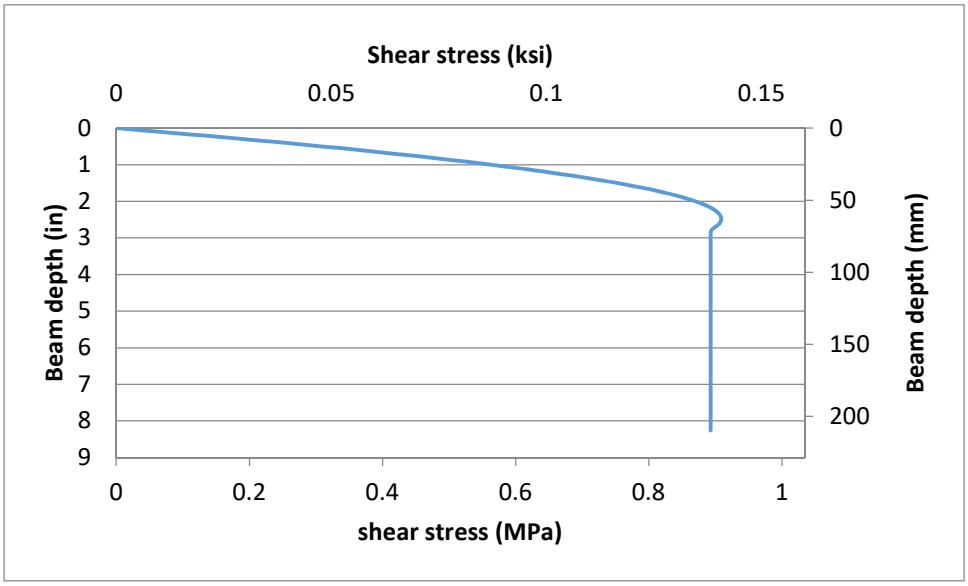

Figure 4-9 Shear stress profile due the compressive concrete

Compressive steel Contribution

The shear stress distribution generated due to the compression steel is constant through the region from the location of the compression steel (d') to the full height of the beam (h), Figure 4-10.

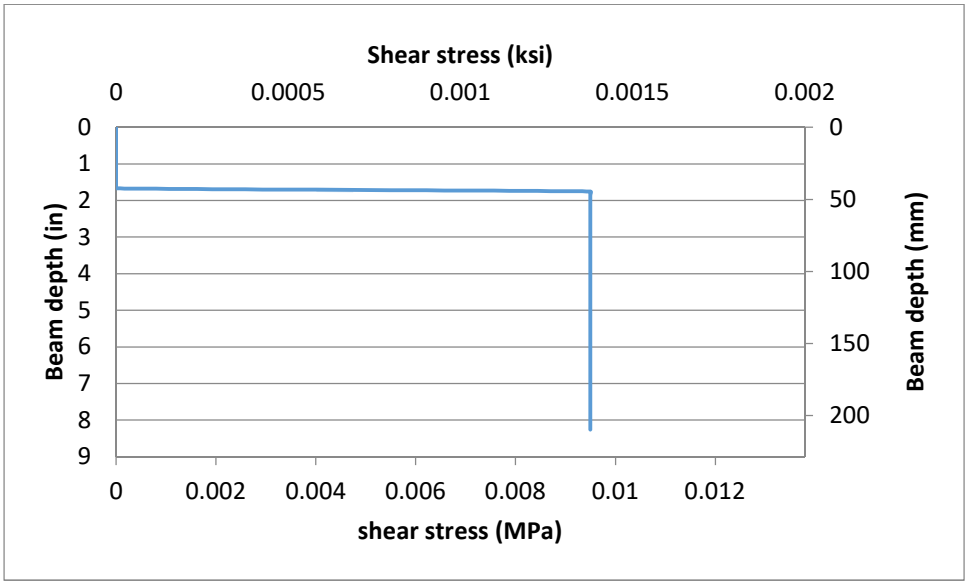

Figure 4-10 Shear stress profile due the compressive steel

The integral due to the compressive steel contribution (A_{cs}) is found by integrating Equation (4.34) as follow

$$A_{cs} = \int_{d'}^{h} A_s' \left(E_s \frac{d\varepsilon_{cf}}{dx} - E_s \frac{d\varphi}{dx} d' - \frac{f_c'}{\varepsilon_c'} \left(2 \frac{d\varepsilon_{cf}}{dx} - 2 \frac{d\varphi}{dx} d' - \frac{2\varepsilon_{cf}}{\varepsilon_c'} \frac{d\varepsilon_{cf}}{dx} + \frac{2d'}{\varepsilon_c'} \frac{d(\varphi\varepsilon_{cf})}{dx} - \frac{\varphi d'^2}{\varepsilon_c'} \frac{d\varphi}{dx} \right) \right) . dy \quad (4\text{-}60)$$

$$A_{cs} = A_s' \left(E_s \frac{d\varepsilon_{cf}}{dx} - E_s \frac{d\varphi}{dx} d' - \frac{f_c'}{\varepsilon_c'} \left(2 \frac{d\varepsilon_{cf}}{dx} - 2 \frac{d\varphi}{dx} d' - \frac{2\varepsilon_{cf}}{\varepsilon_c'} \frac{d\varepsilon_{cf}}{dx} + \frac{2d'}{\varepsilon_c'} \frac{d(\varphi\varepsilon_{cf})}{dx} - \frac{\varphi d'^2}{\varepsilon_c'} \frac{d\varphi}{dx} \right) \right) (h - d') \quad (4\text{-}61)$$

Similarly, the equation could be simplified into

$$A_{cs} = \text{constant } a_2 \frac{d\varphi}{dx} + \text{constant } b_2 \frac{d\varepsilon_{cf}}{dx} \quad (4\text{-}62)$$

Tensile concrete Contribution

As described above, the tensile concrete contribution is divided into two main zones. The first zone generates a shear stress profile as show in Figure 4-11. The integral of this profile (Atc1) is shown in the following equations

$$A_{tc1} = \int_0^{d_{cr}=\frac{\varepsilon_{cr}}{\varphi}} E_c\left((d_t\varphi)(-\frac{d\varepsilon_{cf}}{dx}\frac{1}{\varphi}+\frac{\varepsilon_{cf}}{\varphi^2}\frac{d\varphi}{dx}) + \left(\frac{d_t^2}{2}\right)\frac{d\varphi}{dx}\right).dy + \int_{d_{cr}=\frac{\varepsilon_{cr}}{\varphi}}^{h} E_c\left((d_{cr}\varphi)(-\frac{d\varepsilon_{cf}}{dx}\frac{1}{\varphi}+\frac{\varepsilon_{cf}}{\varphi^2}\frac{d\varphi}{dx}) + \left(\frac{d_{cr}^2}{2}\right)\frac{d\varphi}{dx}\right)dy \quad (4\text{-}63)$$

Where, d_t is measured from the neutral axis and $d_{cr} = \frac{\varepsilon_{cr}}{\varphi}$.

$$A_{tc1} = E_c\left(\left(-\frac{d_t^2}{2}\right)\frac{d\varepsilon_{cf}}{dx} + (\frac{d_t^2\varepsilon_{cf}}{2\varphi}+\frac{d_t^3}{6})\frac{d\varphi}{dx}\right)\Bigg|_0^{\frac{\varepsilon_{cr}}{\varphi}} + E_c\left((d_{cr}\varphi)\left(-\frac{d\varepsilon_{cf}}{dx}\frac{1}{\varphi}+\frac{\varepsilon_{cf}}{\varphi^2}\frac{d\varphi}{dx}\right) + \left(\frac{d_{cr}^2}{2}\right)\frac{d\varphi}{dx}\right)(h - d_{cr}) \quad (4\text{-}64)$$

$$A_{tc1} = E_c\left(\left(-\frac{\varepsilon_{cr}^2}{2\varphi^2}\right)\frac{d\varepsilon_{cf}}{dx} + (\frac{\varepsilon_{cr}^2\varepsilon_{cf}}{2\varphi^3}+\frac{\varepsilon_{cr}^3}{6\varphi^3})\frac{d\varphi}{dx}\right) + E_c\left((d_{cr}\varphi)\left(-\frac{d\varepsilon_{cf}}{dx}\frac{1}{\varphi}+\frac{\varepsilon_{cf}}{\varphi^2}\frac{d\varphi}{dx}\right) + \left(\frac{d_{cr}^2}{2}\right)\frac{d\varphi}{dx}\right)(h - d_{cr}) \quad (4\text{-}65)$$

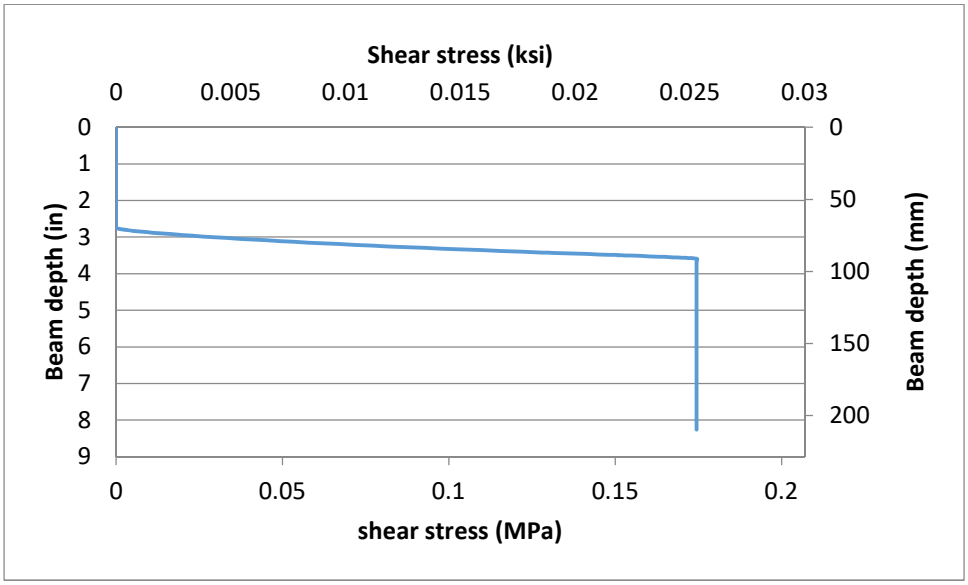

Figure 4-11 Shear stress profile due the tensile concrete (zone 1)

A typical shear stress induced by the second profile of the constitutive concrete tensile model is shown in Figure 4-12.

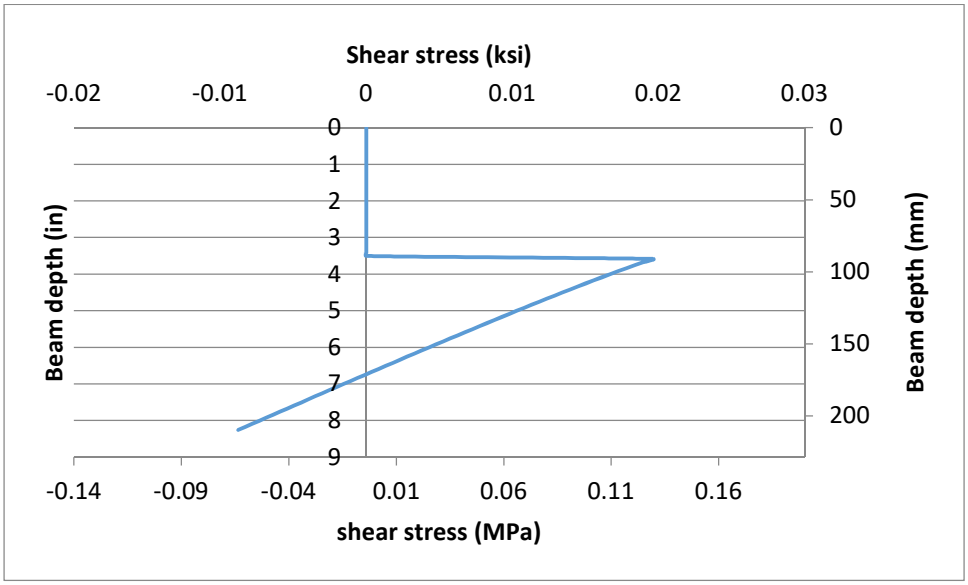

Figure 4-12 Shear stress profile due the tensile concrete (zone 2)

The integral of this profile (A_{tc2}) is calculated by integrating Equation (4.40). The procedure is described in the next set of equations.

$$A_{tc2} = \int_{\frac{f_r}{E_c\varphi}}^{d_t} \tau \, dy \qquad (4\text{-}66)$$

Where, (d_t) is measured downwards from the neutral axis.

$$A_{tc2} = \int_{\frac{f_r}{E_c\varphi}}^{d_t} \left[\left(R\frac{\varepsilon_{cf}}{\varphi^2} + R\frac{\varepsilon_{cr}}{\varphi^2} - k\frac{\varepsilon_{cf}}{\varphi^2}(\ln(d_t\varphi)+1) - \frac{k(d_t)}{\varphi} - k\frac{\varepsilon_{cr}}{\varphi^2}\ln(\varepsilon_{cr}) \right)\frac{d\varphi}{dx} + \left(-\frac{R}{\varphi} + \frac{k}{\varphi}(\ln(d_t\varphi)+1) \right)\frac{d\varepsilon_{cf}}{dx} \right] dy \quad (4\text{-}67)$$

Where, $k = \frac{0.5f_r}{\ln\left(\frac{1.4\varepsilon_y}{\varepsilon_{cr}}\right)}$ and $R = \left(0.5f_r + k + k\ln(\varepsilon_{cr})\right)$

$$A_{tc2} = \left(R\frac{\varepsilon_{cf}}{\varphi^2}(d_t) - k(d_t^2)\frac{1}{2\varphi} - k((d_t)\ln(\varphi d_t))\frac{\varepsilon_{cf}}{\varphi^2} - (Rd_t - k\ln(\varepsilon_{cr})d_t)\left(\frac{-f_r}{E_c\varphi^2}\right) \right)\frac{d\varphi}{dx} +$$

$$\left(R\frac{-1}{\varphi}d_t + k(d_t\ln(\varphi d_t))\frac{1}{\varphi} \right)\frac{d\varepsilon_{cf}}{dx} - \left(R\frac{\varepsilon_{cf}}{\varphi^2}\frac{\varepsilon_{cr}}{\varphi} - k\left(\frac{\varepsilon_{cr^2}}{\varphi^2}\right)\frac{1}{2\varphi} - k(\frac{\varepsilon_{cr}}{\varphi}\ln(\varepsilon_{cr}))\frac{\varepsilon_{cf}}{\varphi^2} - (R\frac{\varepsilon_{cr}}{\varphi} - k\ln(\varepsilon_{cr})\frac{\varepsilon_{cr}}{\varphi}) \left(\frac{-f_r}{E_c\varphi^2}\right) \right)\frac{d\varphi}{dx} - \left(R\frac{-1}{\varphi}\frac{\varepsilon_{cr}}{\varphi} + k(\frac{\varepsilon_{cr}}{\varphi}\ln(\varepsilon_{cr}))\frac{1}{\varphi} \right)\frac{d\varepsilon_{cf}}{dx} \quad (4\text{-}68)$$

This could be simplified into

$$A_{cs} = \text{constant } a_3\frac{d\varphi}{dx} + \text{constant } b_3\frac{d\varepsilon_{cf}}{dx} \quad (4\text{-}69)$$

Tensile Steel Contribution

Similar to the compressive steel contribution, the shear stress profile due to the variation in the steel tensile force is shown in Figure 4-13. The integral due to this profile (Ats) is derived from Equations (4.43)-(4.44).

For pre-yielding condition $f_s \leq f_y$

$$A'_{ts} = \int_d^h A_s\left(-E_s\frac{d\varepsilon_{cf}}{dx} + E_s\frac{d\varphi}{dx}d\right) dy \quad (4\text{-}70)$$

$$A'_{ts} = A_s\left(-E_s\frac{d\varepsilon_{cf}}{dx} + E_s\frac{d\varphi}{dx}d\right)(h-d) \quad (4\text{-}71)$$

For post-yielding condition $f_s > f_y$

$$A'_{ts} = \int_d^h A_s \left(-(E_s + E'_s)\frac{d\varepsilon_{cf}}{dx} + (E_s + E'_s)\frac{d\varphi}{dx}d\right) dy \quad (4\text{-}72)$$

$$A'_{ts} = A_s \left(-(E_s + E'_s)\frac{d\varepsilon_{cf}}{dx} + (E_s + E'_s)\frac{d\varphi}{dx}d\right)(h - d) \quad (4\text{-}73)$$

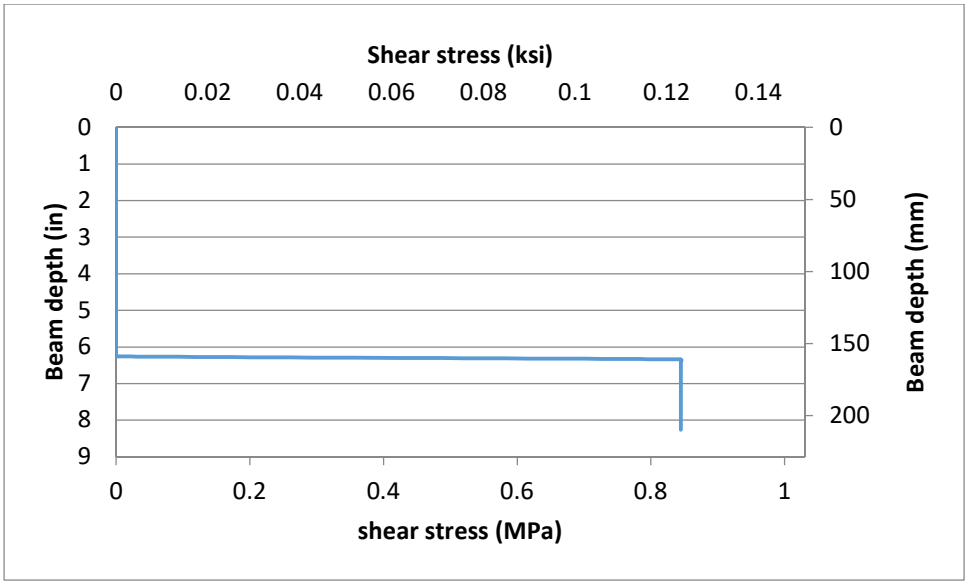

Figure 4-13 Shear stress profile due the tensile steel

The contribution of the steel bar holes must be subtracted from the tensile steel equations (4.71) or (4.73), as shown in equations (4.45) or (4.46), which still needs to be integrated with respect to y measured from the tensile steel level (d) to (h). The latter contribution must be subtracted from A'_{ts} to yield A_{ts}.

From Equations (4.56)-(4.73), the second condition equation is formulated

$$\frac{V}{b} = A_{cc} + A_{cs} - A_{tc1} - A_{tc2} - A_{ts} \quad (4\text{-}74)$$

$$\frac{V}{b} = q_{12}\frac{d\varphi}{dx} + q_{22}\frac{d\varepsilon_{cf}}{dx} \quad (4\text{-}75)$$

Where, q_{12} and q_{22} are functions of the geometrical and material properties as well as the strain profile parameters.

4.5.4 Evaluating the derivative of the strain profile parameters

The only unknowns in Equations (4.55) and (4.75) are $\frac{d\varphi}{dx}$ and $\frac{d\varepsilon_{cf}}{dx}$. This set of equations could be presented in a matrix form, see Equation (4.76). By considering the inverse of a 2x2 matrix, $\frac{d\varphi}{dx}$ and $\frac{d\varepsilon_{cf}}{dx}$ could be calculated.

$$\begin{bmatrix} q_{11} & q_{12} \\ q_{21} & q_{22} \end{bmatrix} \begin{bmatrix} \frac{d\varphi}{dx} \\ \frac{d\varepsilon_{cf}}{dx} \end{bmatrix} = \begin{bmatrix} 0 \\ V/b \end{bmatrix} \tag{4-76}$$

$$\begin{bmatrix} \frac{d\varphi}{dx} \\ \frac{d\varepsilon_{cf}}{dx} \end{bmatrix} = \begin{bmatrix} q_{11} & q_{12} \\ q_{21} & q_{22} \end{bmatrix}^{-1} \begin{bmatrix} 0 \\ V/b \end{bmatrix} \tag{4-77}$$

Figure 4-14 and Figure 4-15 show a numerical evaluation of the two derivatives at hand versus the analytical values from equation (4.77) along the shear span. These comparisons show the accuracy of the proposed method and support the claim that the change of the curvature along the shear span is not constant. Although, a trilinear model is a good approach to represent the sectional behavior, a differential application requires an accurate estimation of the derivatives of the strain profile parameters along the shear span.

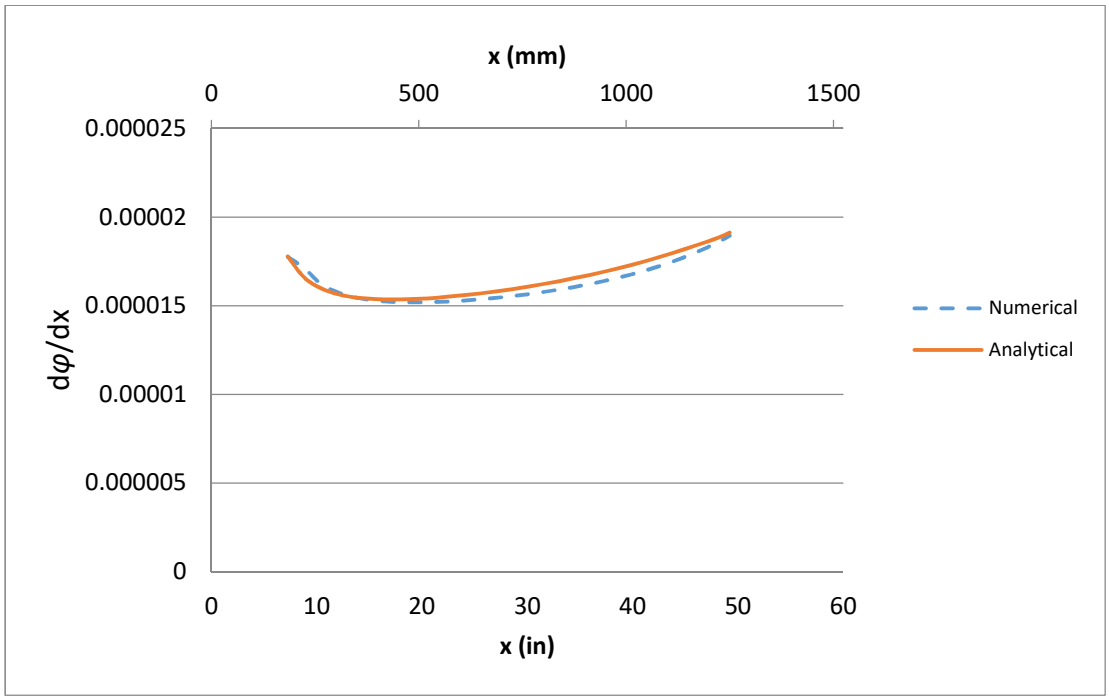

Figure 4-14 The derivative of section curvature along the shear span dφ/dx vs. the shear span using example one below (post cracking zone)

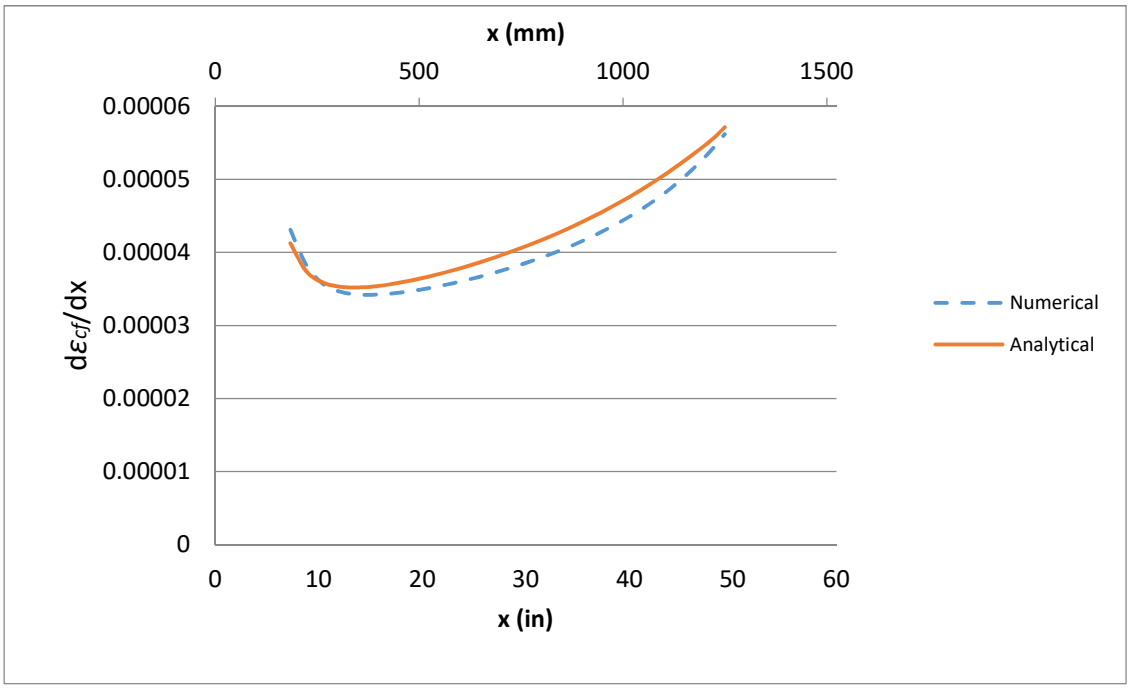

Figure 4-15 The derivative of the maximum compressive strain along the shear span dε_{cf} /dx vs. the shear span using example one below (post cracking zone)

4.6 Results

In this section, the proposed analytical formulation is applied to generate the shear stresses at different sections and load levels. A detailed example is presented to illustrate the proposed procedure. First, the trilinear analytical approach is compared to the experimental results of Almusallam (1997), see Figure 4-16.

The tested rectangular beam has a 200 mm*210 mm (7.87 in x 8.26 in) in cross section. It has a length of 2.700 m (106.3 in) with a shear span of 1.252 m (49.3 in). The main flexural reinforcement consists of 3 φ 14 mm bars with 1 φ 6.25 mm bars used for the compression steel just to provide a caging framework for the shear reinforcement. The beam has shear reinforcement consisting of φ 8 mm stirrups at 120 mm (4.7 in) spacing.

The concrete nominal strength is 31.3 MPa (4540 psi). The reinforcing steel has a yielding strength of 552.6 MPa (80.2 ksi) and a modulus of elasticity of 200,000 MPa (29000 ksi).

The shear stresses are then retrieved at three different cross sections. The first location (section one) is at an early stage of the post-cracking zone and the second location (section two) is positioned just prior to the section where yielding of tensile steel first occurs. These two sections were analyzed under 75% of the failure load. The third location (section three) is positioned just under the concentrated force at the failure load of the beam in the post-yielding zone.

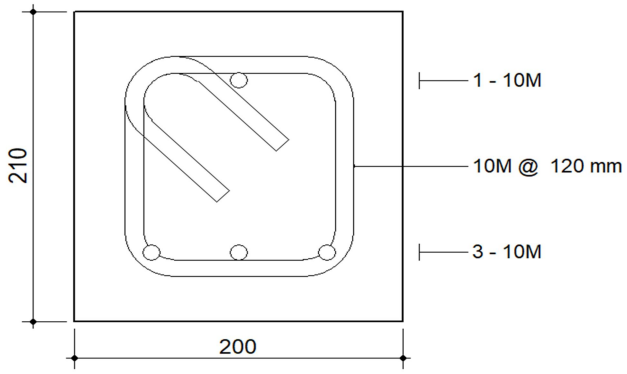

Figure 4-16 Almusallam (1997) cross section (SI units)

For a given applied load and a cross section location, the shear force (V) and the moment (M) are calculated at a distance x from the support as follow, see Figure 4-17.

$$V = \frac{P}{2} \tag{4-78}$$

$$M = \frac{P}{2}x \tag{4-79}$$

To continue with the analysis, the strain profile parameters, namely the curvature (φ) and the maximum compressive strain (ε_{cf}) are retrieved from the trilinear approach

$$\varphi = \frac{M-M_{cr}}{M_y-M_{cr}}\left(\varphi_y - \varphi_{cr}\right) + \varphi_{cr} \tag{4-80}$$

if $M_{cr} < M < M_y$, as in sections one or two.

$$\varphi = \frac{M-M_y}{M_n-M_y}\left(\varphi_n - \varphi_y\right) + \varphi_y \tag{4-81}$$

if $M_y < M < M_n$, as in section three.

Similarly, the maximum compressive strain (ε_{cf}) is computed

$$\varepsilon_{cf} = \frac{M-M_{cr}}{M_y-M_{cr}}\left(\varepsilon_{cf_y} - \varepsilon_{cf_{cr}}\right) + \varepsilon_{cf_{cr}} \tag{4-82}$$

if $M_{cr} < M < M_y$, as in sections one or two.

$$\varepsilon_{cf} = \frac{M-M_y}{M_n-M_y}\left(\varepsilon_{cf_n} - \varepsilon_{cf_y}\right) + \varepsilon_{cf_y} \tag{4-83}$$

if $M_y < M < M_n$, as in section three.

The next step of the analysis is to estimate the derivative magnitudes $\frac{d\varphi}{dx}$ and $\frac{d\varepsilon_{cf}}{dx}$. Condition one, Equations (4.48)-(4.55) and condition two, Equations (4.56)-(4.75) were applied to determine $\frac{d\varphi}{dx}$ and $\frac{d\varepsilon_{cf}}{dx}$.

$$\begin{bmatrix} q_{11} & q_{12} \\ q_{21} & q_{22} \end{bmatrix} \begin{bmatrix} \frac{d\varphi}{dx} \\ \frac{d\varepsilon_{cf}}{dx} \end{bmatrix} = \begin{bmatrix} 0 \\ V/b \end{bmatrix} \tag{4-84}$$

$$\begin{bmatrix} \frac{d\varphi}{dx} \\ \frac{d\varepsilon_{cf}}{dx} \end{bmatrix} = \begin{bmatrix} q_{11} & q_{12} \\ q_{21} & q_{22} \end{bmatrix}^{-1} \begin{bmatrix} 0 \\ V/b \end{bmatrix} \quad (4\text{-}85)$$

Upon finding the derivatives $\frac{d\varphi}{dx}$ and $\frac{d\varepsilon_{cf}}{dx}$, for example section one results are shown in Figure 4-14 and Figure 4-15, Equations (4.32) to (4.47) are applied to accurately calculate the shear stress distribution at any given depth.

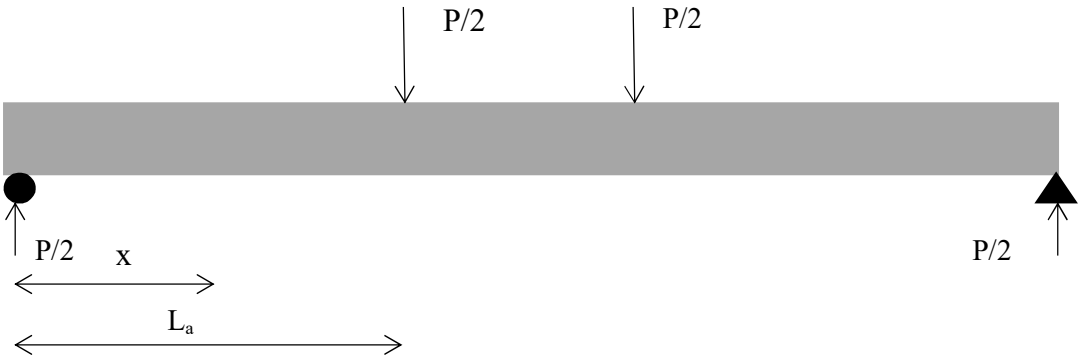

Figure 4-17 Profile of imply supported beam under four-point bending tested by Almusallam (1997)

Table 4-2 shows the location of each examined section as well as the corresponding shear force (V) and bending moment (M). In addition, it shows the computed curvature (φ) and maximum compressive strain (ε_{cf}) based on the trilinear approach, Figure 4-18.

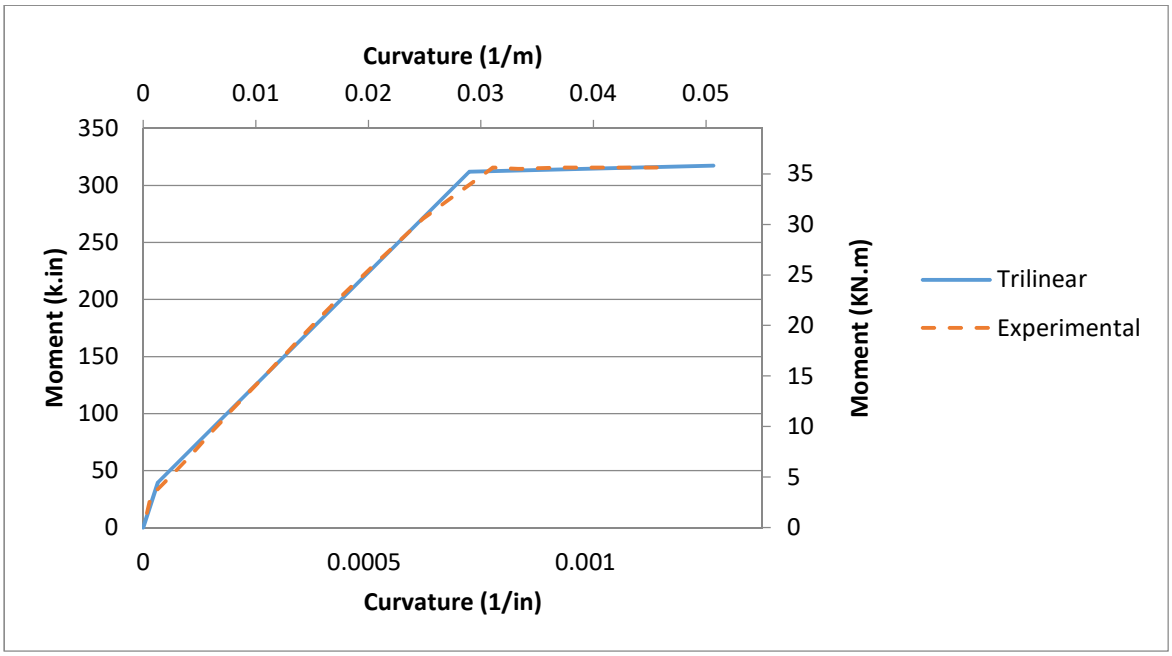

Figure 4-18 Trilinear response vs. experimental moment-curvature graph for beam tested by Almusallam (1997)

Table 4-2 Parameters for the three sections analyzed to compute their shear stress distribution.

	V (KN)	x (mm)	M (KN.m)	ϕ	ε_{cf}
Section one	22.55	508.00	11.46	0.00662	0.00047
Section two	22.55	1102.36	24.86	0.02246	0.00146
Section three	30.16	1252.22	37.76	0.05076	0.003

As shown in Figure 4-19, Figure 4-20 and Figure 4-21, the shear stress distribution varies depending on the loading and section location. Also unlike the symmetrical second-degree parabola (i.e. shear stress distribution of un-cracked cross section) sections in the post-cracking and post yielding zones are no longer symmetrical due to the change in concrete behavior in tension and compression in addition to the existence of the steel. However, there are key locations where the shear stress distribution changes its behavior. By following the shear stress profile from the top of the section to its soffit, these key locations are defined. The first region (zone A), see Figure 4-19, shows the effect of the compressive concrete contribution. This region starts with a shear stress equal to zero at the top of the cross section as it is a free surface, and it

terminates at the neutral axis depth. Zone B is the region that has the effect of the first part of the tensile concrete constitutive model. The third region is zone C and it is nearly linear due to the effect of the second tensile zone (tension stiffening) until reaching the level of the tensile steel (Dowel action). Dowel action causes a drop in the shear stress profile to a small negative value. However due to the effect of the remainder of tension stiffening contribution in the concrete cover, the shear stress comes back to zero as expected (free surface at the beam soffit) (Zone D).

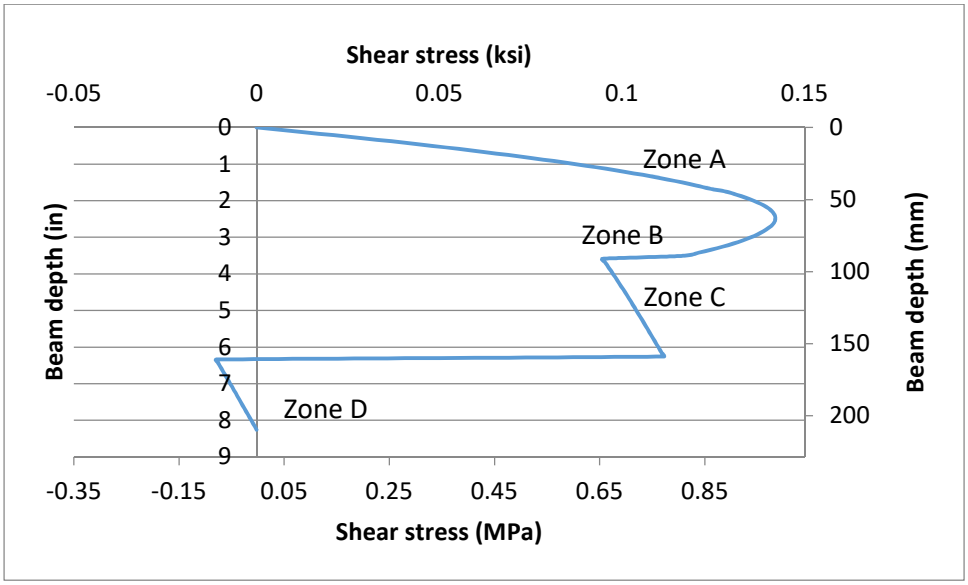

Figure 4-19 Shear stress distribution of section one for the beam tested by Almusallam 1997.

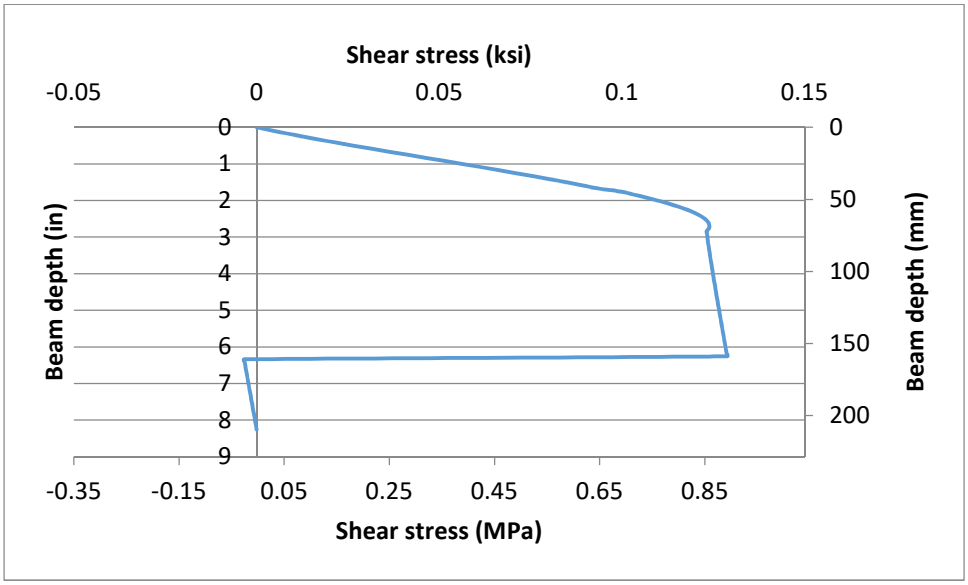

Figure 4-20 Shear stress distribution of section two for the beam tested by Almusallam 1997

.

In section three at the failure load just under the concentrated force point, Figure 4-21, it is interesting to observe the opposite change in direction of the shear stresses within the compressive depth. This change is a result of the descending branch of the Hognestad's parabola. Furthermore, the shear stress shows a constant zero region across the concrete cover depth as the tension-stiffening model vanishes at 1.4 times the yielding strain of the steel.

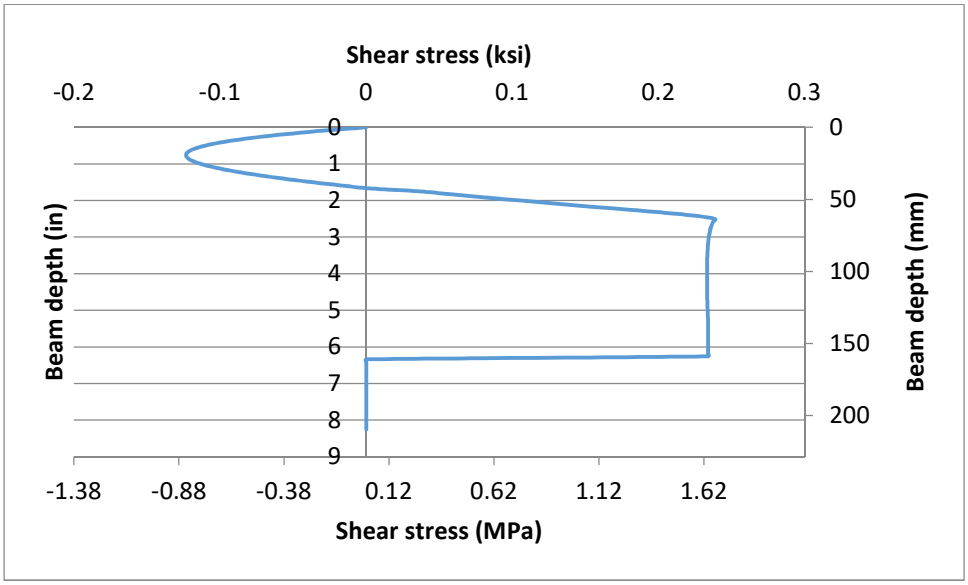

Figure 4-21 Shear stress distribution of section three for the beam tested by Almusallam 1997.

4.7 Conclusions

In this study, the authors intend to provide a mechanics-based understanding of the shear behavior in reinforced concrete flexural beams. An analytical formulation of shear stress distribution in cracked reinforced concrete, throughout its stages of post-cracking and post yielding, is presented using the smeared crack approach. This formulation uses the transverse shear differential equation to compute the shear stress at any given depth across the height of the beam through the derivative of axial forces acting above that desired depth. While the axial forces are found in accordance with the corresponding strain profile, which is computed by idealizing the sectional response of the beam to trilinear sectional relationships. Furthermore, the effect of the longitudinal steel on shear stress distribution, known as dowel action, is computed for the first time and found to be significant enough not to be ignored as typically done in design codes. In addition, the study provided a detailed evaluation of the variation of the strain profile parameters (φ, ε_{cf}) with respect to shear span or the corresponding moment, which is

found to be non-linear compared to other studies that assume it as a constant. This analytical formulation was then applied to an experimental study to retrieve the shear stresses at three different cross sections under different applied loads. It is interesting to observe for the first time from the generated shear profiles certain key features of the behavior that may prove to be very useful in interpreting shear failures, which are beyond the scope of this study.

4.8 References

Almusallam, T.H., (1997) "Analytical Prediction of Flexural Behavior of Concrete Beams Reinforced by FRP Bars," Journal of Composite Materials, Vol. 31, No. 7, pp 640-657.

Bazant, Z. P., Kazemi, M. T., (1991) “Size effect on diagonal shear failure of beams without stirrups”, ACI structural journal, Vol. 88(3), pp 268-276.

Mphonde, A. G., Frantz, G. C. (1984) “Shear tests of high and low-strength concrete beams without stirrups”. ACI journal, Vol. 81(4), pp 350-357.

Moody,K.G., Viest, I.M., Elstner, R.c., and Hognestad,E. (1954) ”Shear Strength of Reinforced Concrete Beams, Part-1 Tests of Simple Beams ". ACI Journal, proceedings Vol. 51, pp. 317-332.

Morsch, E., (1903) "Versuche Uber Schubspannugen in Betoneisentragern," Beton und Eisen Berlin, Vol. 2, No. 4, pp. 269-274.

Rasheed, H. A., (1990) “Inelastic Behavior of Reinforced Concrete Frame Structures”. M.Sc. Thesis, University of Baghdad, Iraq.

Rasheed, H.A., Larson, K.H., and Nayyeri Amiri, S. (2013)”Analytical Solution of Interface Shear Stresses in Externally Bonded FRP-Strengthened Concrete Beams”. Journal of Engineering Mechanics, Vol.139, pp. 18–28.

Chapter 5 - Mathematical Characterization of Crushing Failure Mode in Flexural Reinforced Concrete Beams

Concrete crushing failure mode in reinforced concrete flexural beams, for the most part, is thought-out to be independent of concrete cracking. Accordingly, it was specified to occur at a constant compressive strain selected by ACI 318 to be 0.003 and by Euro code at 0.0035. In this study, a new approach is developed to predict this failure mode numerically by considering concrete cracking produced at crushing failure mechanism. The combination of axial compressive stresses and shear stresses within the compression zone were used to explain the occurrence of concrete cracking at the crushing point slightly below the top surface through a dish –like crack that develops at the location of maximum moment. The calculation of shear stress profile after yielding is performed using an innovative smeared crack approach. This shear stress distribution combined with axial compressive stresses yields tensile-compressive principal stress state that captures tensile cracking when a biaxial concrete failure criterion is invoked. Applications of shallow beams tested in flexure up to concrete crushing failure mode are examined. The presented numerical results are, thus, experimentally qualified.

5.1 Introduction

Concrete crushing is one of the most desirable failure criteria of reinforced concrete if it takes place after steel yielding. Yet, it lacks a complete agreement among the researchers. According to many reinforced concrete design codes, concrete crushing is a phenomenon that is only related to the compressive stresses in concrete. Although ACI 318-14 adopted the value of 0.003 to represent the maximum useful concrete strain (crushing strain), ACI 318 commentary states that the maximum compressive strain in concrete at crushing has been observed in tests to range

between 0.003-0.008. Furthermore, PCA Notes (2013) presents a collection of compressive failure strains from beam and column tests in a graph showing a scatter in the range of 0.0028-0.0058. In 1955, Hognestad et al. developed a concrete stress distribution in compression. This model follows an ascending parabolic curve up to the maximum compressive strength and then starts to descend until reaching a maximum compressive strain. Also Hognestad et al. built a C-shaped specimen to study the concrete compressive behavior.

This approach, of limiting the concrete compressive strain, did not manage to answer Gonnerman (1925) question of; why does the ratio of the compressive failure stress to the compressive strength decreases according to the size effect? While this question motivated Bazant (1984) to derive the size effect law, which uses the principle of energy balance of cracks to explain the behavior of geometrically similar structures with different sizes. From a different perspective, Zwoyer (1954) observed the similarity between the diagonal tensile cracks and the flexural compression failure (concrete crushing). Using this observation, Moody et al. (1954) described the failure of reinforced concrete beams to be composed of two stages; the first stage includes diagonal tension cracking followed by crushing as a second stage. However, the described failure mode was said to be controlled by (M/Vd) ratio. With smaller ratios, the described diagonal tension mode of failure occurs. Larger (M/Vd) ratio results in almost pure flexural crushing failure.

In this study, the authors utilized to the actual stress state in cracked reinforced concrete beams to present a numerical demonstration of concrete crushing as a cracking failure mode. The combination of axial compressive stresses and shear stresses within the compression zone were used to explain the occurrence of concrete cracking at the crushing point through a dish –like crack that develops at the section of maximum moment. The calculation of shear stress profile

after yielding is performed using the transversal shear differential equation under the smeared crack assumption. The biaxial stress state within the compression zone was compared to a biaxial failure criterion to determine the concrete state. This study emphasizes that the concrete crushing is nothing but an oriented concrete principal tensile stress failure in the compression zone.

5.2 Nonlinear sectional Analysis

A fully independent stress-strain relationship is assumed between the concrete and the reinforcing steel. The axial stress in steel would be a result of the axial strain in the steel only.

5.2.1 Concrete Behavior

The concrete stress-strain relationship is assumed to follow the Hognestad's curve, Equation (5.1), for compressive stresses (f_c) and a linear relationship with a slope equal to the concrete modulus of elasticity (E_c) up to cracking strain (ε_{cr}) in tension, Figure 5-1. This linear relationship is then followed by a descending curve as a numerical function in (ε_{cr}) and the steel yielding strain (ε_y), see Figure 5-4.

$$f_c = f_c' \left(2\frac{\varepsilon_c}{\varepsilon_{c'}} - \left(\frac{\varepsilon_c}{\varepsilon_c'}\right)^2\right) \quad (5\text{-}1)$$

The concrete tensile rupture stress (f_r) is taken as a lower bound equivalent to $5 - 7.5\sqrt{f_c'}$, for light weight concrete this value is reduced by 25%. A linear relationship with a slope equal to the concrete modulus of elasticity (E_c) up to cracking strain (ε_{cr}) in tension is assumed.

The concrete behavior in tension after the cracking strain is described using Equation (5.2). The constants in the developed equation were calibrated against a large pool of four points bending tests on shallow beams.

$$\frac{f_t}{0.5fr} = 1 - \frac{1}{\ln\left(\frac{1.4\varepsilon_y}{\varepsilon_{cr}}\right)} \ln\left(\frac{\varepsilon_t}{\varepsilon_{cr}}\right) \quad (5\text{-}2)$$

This proposed descending function on the domain ($\varepsilon_{cr} \leq \varepsilon_t \leq 1.4\varepsilon_y$) starts by a sudden drop from its peak (f_r) to (0.5 f_r) at the cracking strain (ε_{cr}) and continues to descend till zero when the tensile strain reaches (1.4 ε_y), see Figure 5-2. This function is an average function between the tension softening which exist near the cracking strains and the tension stiffening that activates around the steel bar locations.

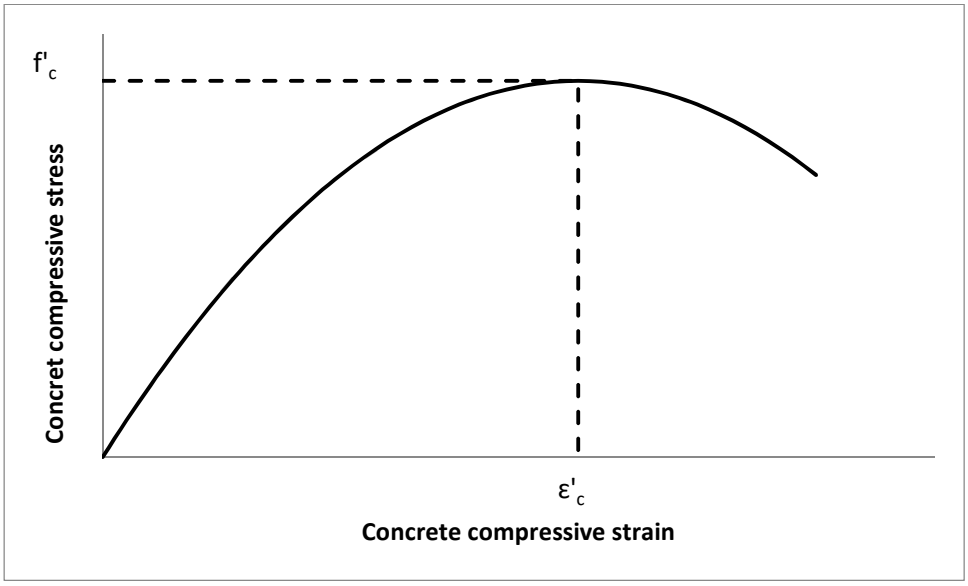

Figure 5-1 Concrete compressive stress-strain curve (Hognestad's Equation)

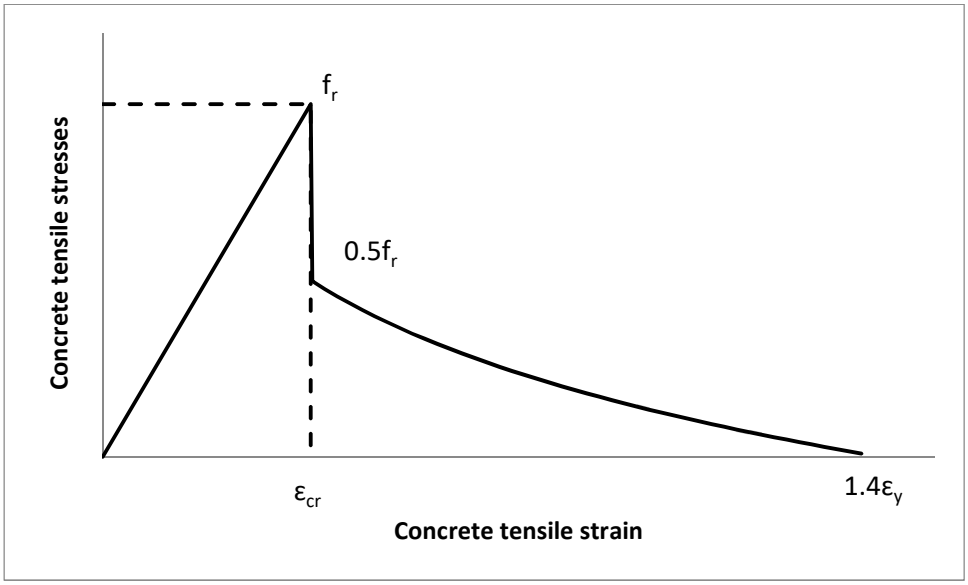

Figure 5-2 Concrete tensile stress-strain relationship

5.2.2 Steel Behavior

Regarding the steel axial stress-axial strain relationship, a bilinear relationship is assumed in both the compressive and the tensile analysis, Figure 5-3.

$$f_s = E_s \varepsilon_s \leq f_y \tag{5-3}$$

Where (f_s) is the steel stress corresponding to the axial strain (ε_s), (E_s) is the modulus of elasticity of steel, (f_y) is the steel yielding stress. The steel is assumed to start hardening after exceeding the yielding stress (f_y) according to the following equation

$$f_s = f_y + E'_s(\varepsilon_s - \varepsilon_y), when\ f_s > f_y \tag{5-4}$$

(E'_s) is the slope of steel hardening after yielding and it is determined based on the yielding strength (f_y), Table 5-1 shows the relationship between the estimated (E'_s) and the corresponding (f_y) (Rasheed (1990)).

Table 5-1 The estimated modulus of elasticity (E'_s) and the corresponding (f_y) relationship

f_y (ksi)	E'_s / E_s
40-45	0.3-0.7%
45-50	0.7-1.2%
50-63	1.2-2.5%

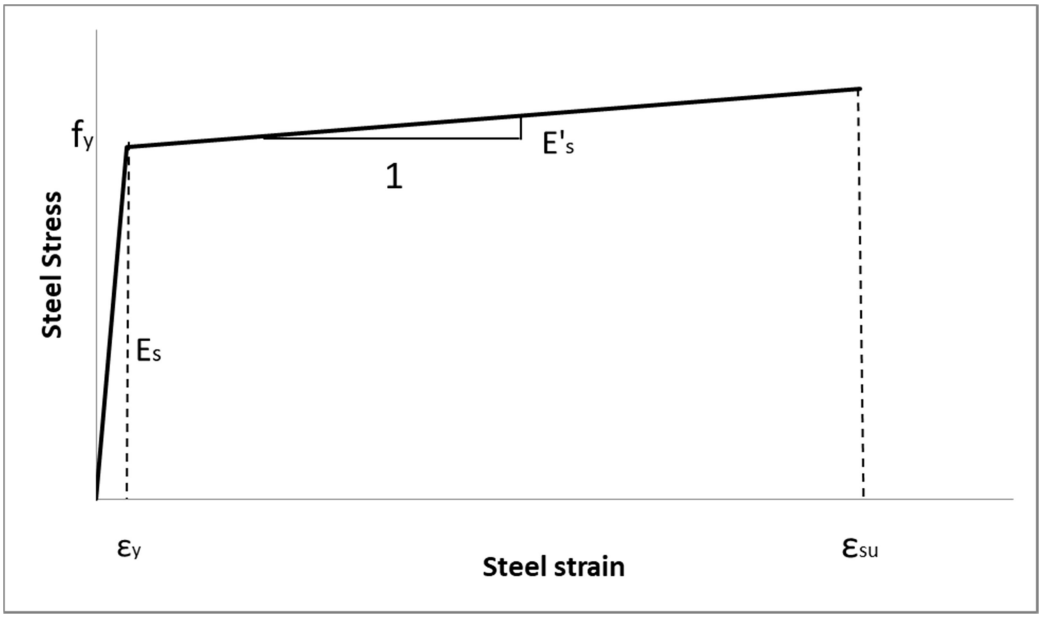

Figure 5-3 Steel stress-strain relationship

5.3 Sectional Analysis approach

5.3.1 Forces

5.3.1.1 Compressive Forces

Compressive concrete contribution

By integrating the Hognestad's profile over the region from the neutral axis up to the maximum compressive concrete fiber, the concrete compressive force (C_c) is derived for the section based on the following equations

$$C_c = \int_0^C f_c . b \, dy \qquad (5\text{-}5)$$

$$C_c = f_c' b . \frac{\Phi}{\varepsilon_c'} (c^2 - \frac{\Phi}{3} \frac{C^3}{\varepsilon' c}) \quad (5\text{-}6)$$

Compressive Steel Contribution

The compressive steel force (C_s) is a linear relationship with the corresponding steel strain (ε_s'). This relationship was driven based on the assumption of the bilinear behavior for the steel analysis.

$$C_s = A_s' f_s - A_s' f_c' ((2 \frac{\varepsilon_s'}{\varepsilon_c'} - \_ \left(\frac{\varepsilon_s'}{\varepsilon_c'}\right)^2) \quad (5\text{-}7)$$

5.3.1.2 Tensile Forces

Tensile steel Contribution

The tensile steel force (T_s) follows the same bilinear behavior based on the following equation

$$T_s = A_s E_s \varepsilon_s, when\ f_s \leq f_y \quad (5\text{-}8)$$

$$T_s = A_s (f_y + E_s' (\varepsilon_s - \varepsilon_y)), when\ f_s > f_y \quad (5\text{-}9)$$

Tensile Concrete contribution

The concrete tensile capacity is divided into two main profiles, Figure 5-2. The first profile is a linear relationship up to the cracking strain (ε_{cr}) with a slope equal to the concrete modulus of elasticity (E_c). This profile leads to a tensile force (T_{c1}) equals to

$$T_{c_1} = \int_0^{d_t} f_t . b\ dy \quad (5\text{-}10)$$

$$T_{c_1} = \frac{f_r^2}{2 E_c \Phi} \quad (5\text{-}11)$$

The second profile is a descending curve which majorly contributes in the total concrete tensile capacity. This profile is a result of the concrete softening, concrete stiffening due to the steel

bond as well as the residual stresses due to shrinkage effect. The tensile force due to this profile (T_{c2}) is calculated as follow

$$T_{c2} = \int_{d_{cr}}^{d_{ts}} bf_t dy = b\int_{d_{cr}}^{d_{ts}} 0.5f_r - \frac{0.5f_r}{\ln(\frac{1.4\varepsilon_y}{\varepsilon_{cr}})} \ln\left(\frac{\varepsilon_t}{\varepsilon_{cr}}\right) dy \quad (5\text{-}12)$$

Where y is measured from the neutral axis

$$T_{c2} = [-\frac{0.5bf_r}{\ln(\frac{1.4\varepsilon_y}{\varepsilon_{cr}})}(y\ln(\varphi) + yln(y) - y - yln(\varepsilon_{cr})) + 0.5f_r y]_{\varepsilon_{cr}/\varphi}^{1.4\varepsilon_y/\varphi} \quad (5\text{-}13)$$

Where,

$$d_{ts} = 1.4\varepsilon_y/\varphi \quad (5\text{-}14)$$

5.3.2 Moments

5.3.2.1 Compressive concrete contribution

The point of application of concrete compressive force is measured from the extreme compressive fiber ($\gamma\ c_y$) based on volume centroid calculations. Where (c) is the depth of the compression zone and (γ) is a ratio between zero and one.

$$\gamma = 1 - \frac{\int_0^{\varepsilon_{cf}} \varepsilon_c . f_c . d\varepsilon_c}{\varepsilon_{cf} \int_0^{\varepsilon_{cf}} f_c . d\varepsilon_c} = \frac{\frac{1}{3} - \frac{\varepsilon_{cf}}{12\ f'_c}}{1 - \frac{\varepsilon_{cf}}{3e'_c}} \quad (5\text{-}15)$$

$$M_{cc} = (C - \gamma . C) * C_c \quad (5\text{-}16)$$

5.3.2.2 Compressive Steel Contribution

The compression steel moment is calculated according to the following equation.

$$M_{cs} = C_s(C - d') \quad (5\text{-}17)$$

5.3.2.3 Tensile Concrete contribution

(M_{tc1}) is the moment induced due to the concrete resistance up to the cracking point. While, (M_{tc2}) is the moment due to the constitutive tensile model.

$$M_{tc} = T_{c1}.\frac{2}{3}\frac{f_r}{E_c.\phi} \quad (5\text{-}18)$$

$$M_{tc} = \int_{d_{cr}}^{d_{ts}} bf_t y dy = b\int_{d_{cr}}^{d_{ts}} [0.5f_r - \frac{0.5f_r}{\ln(\frac{1.4\varepsilon_y}{\varepsilon_{cr}})}\ln\left(\frac{\varepsilon_t}{\varepsilon_{cr}}\right)]y\ dy \quad (5\text{-}19)$$

Where, y is measured from the neutral axis.

$$M_{tc} = [-\frac{0.5bf_r}{\ln\left(\frac{1.4\varepsilon_y}{\varepsilon_{cr}}\right)}\left(\frac{y^2}{2}\ln(\varphi) + \frac{y^2}{2}ln(y) - \frac{y^2}{4} - \frac{y^2}{2}ln(\varepsilon_{cr})\right) + 0.5f_r\frac{y^2}{2}]_{\varepsilon_{cr}/\varphi}^{1.4\varepsilon_y/\varphi} \quad (5\text{-}20)$$

5.3.2.4 Tensile steel Contribution

The contribution of the moment induced due to the steel reinforcement at any stage of loading is determined as follows

$$M_{ts} = T_s(d - C) \quad (5\text{-}21)$$

5.3.3 Moment-Curvature Calculations

A numerical procedure was followed to generate the moment-curvature curve. In this procedure, the maximum compressive fiber strain value (ε_{cf}) was gradually increased until reaching the concrete crushing strain of (0.003). In order to accurately calculate the strain profile under each step value of εcf, the correct depth of the compression zone (c) was necessary to define the strain profile and the corresponding stress profile and forces/moments. The sectional force equilibrium equation was then applied to validate the depth of the compression zone (c) by iterating for the correct depth of compression zone that makes the summation of forces equal to zero, equilibrium is maintained.

$$\varphi = \frac{\varepsilon_{cf}}{c} \quad (5\text{-}22)$$

$$\varepsilon_s = \varphi(d - c) \quad (5\text{-}23)$$

$$\varepsilon_s' = \varphi(c - d') \quad (5\text{-}24)$$

$$\varepsilon_{sf} = \varphi(h - c) \quad (5\text{-}25)$$

The summation of moments due to concrete and steel contributions then yielded the applied internal moment of the section, and the moment-curvature curves were fully generated, see Figure 5-4. The progressive moment-curvature calculation procedure is described in a flow chart, see Figure 5-5.

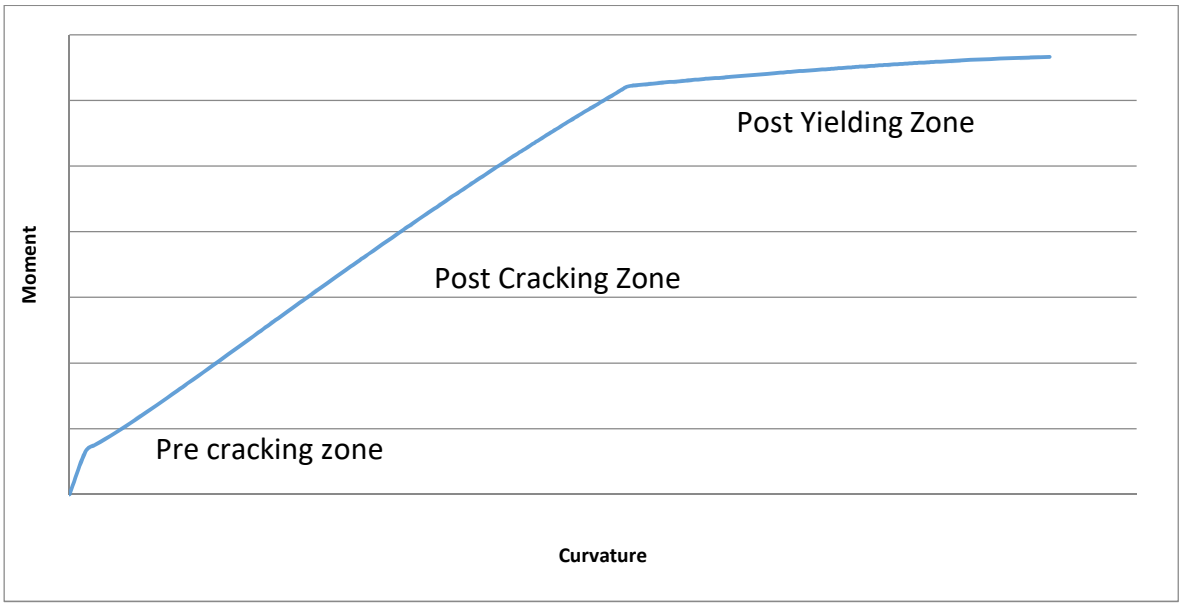

Figure 5-4 Typical beam moment vs. curvature sectional response

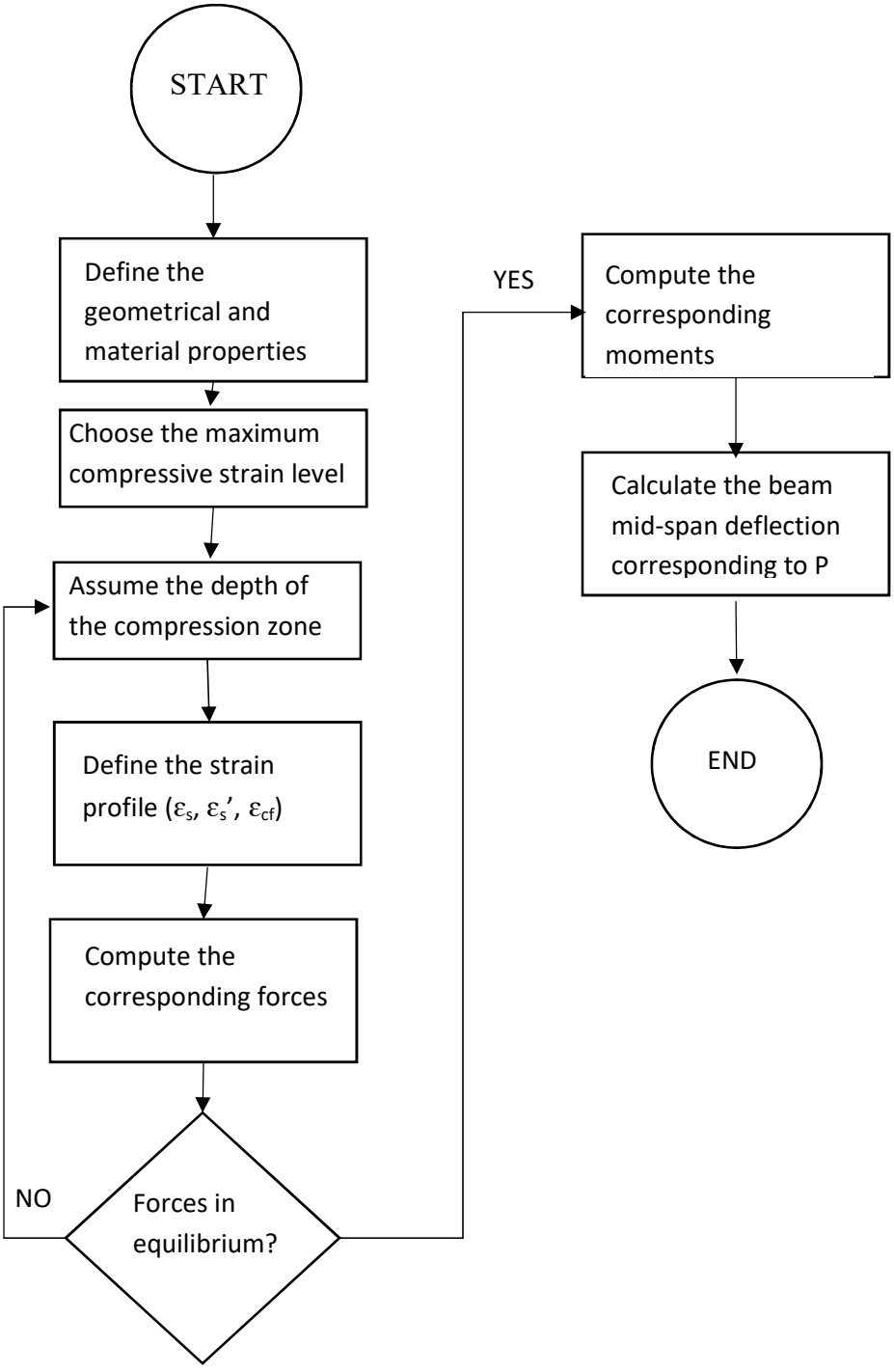

Figure 5-5 Sectional analysis flow chart

5.4 Differential Sectional Analysis

5.4.1 Shear Stresses Differential Equation

Shear stresses distribution over a shallow beam depth is formulated through the axial forces acting on the beam cross section. Considering an infinitesimal element with length dx of the beam, the differential bending moment acting over dx is dM, Figure 5-6. At any given depth, the equilibrium of forces in the longitudinal direction is satisfied through the longitudinal shear τ_{yx}, Figure 5-7. Also from equilibrium, the longitudinal shear is equal to the transversal shear τ_{xy}.

$$\sum F_x = 0 \tag{5-26}$$

$$\int \sigma'.dA - \int \sigma''.dA - \tau(b.dx) = 0 \tag{5-27}$$

$$F' - F'' - \tau(b.dx) = 0 \tag{5-28}$$

$$dF - \tau(b.dx) = 0 \tag{5-29}$$

$$\tau = \frac{1}{b}\frac{F'-F''}{dx} = \frac{1}{b}\frac{dF(\varphi,\varepsilon)}{dx} \tag{5-30}$$

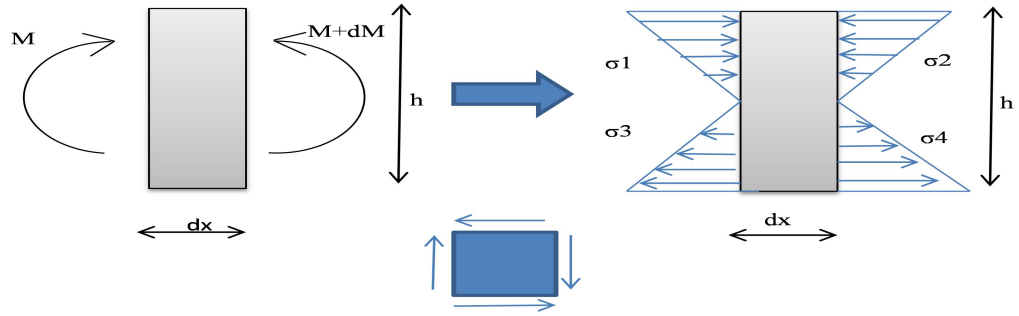

Figure 5-6 Axial stress distribution over an infinitesimal element dx

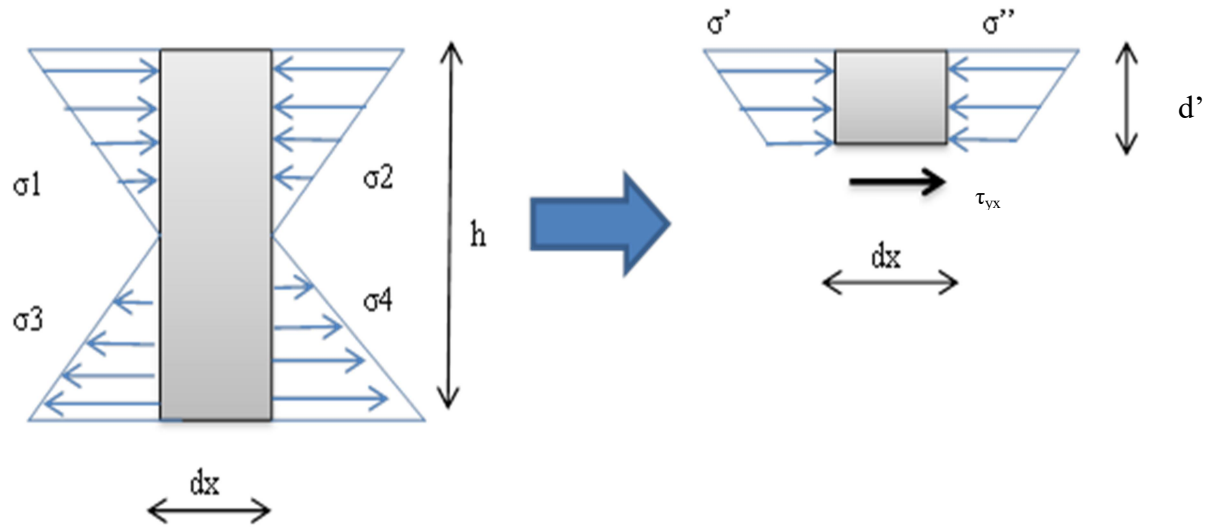

Figure 5-7 Axial stress distribution over an infinitesimal element dx and depth d'

5.4.2 Numerical Evaluation of Shear Stress Distribution

For each load level, one hundred vertical sections were taken over the beam shear span length. For each vertical section, 50 equally spaced nodes were taken along the height of the section. At any given depth, the axial forces are calculated by integrating the axial stresses over the covered distance. By summing the axial forces above a given depth for two constitutive vertical sections, the shear stress at the given depth is evaluated, Equation (5.31).

5.4.2.1 Compressive concrete contribution

By integrating the Hognestad's profile over the area from the top of the section to the specific depth dc, the concrete compressive force (Cc) is derived for the section based on the following equations

$$C_c = \int_{c-d_c}^{C} f_c . b\, dy = \int_{c-d_c}^{c} b f_c' \left(\frac{2\varepsilon_c}{\varepsilon_c'} - \left(\frac{2\varepsilon_c}{\varepsilon_c'} \right)^2 \right) dy \qquad (5\text{-}31)$$

where, y is measured from the neutral axis

$$C_c = b f_c' \frac{\Phi}{\varepsilon_c'} \left(y^2 - \frac{\Phi}{3} \frac{y^3}{\varepsilon_c'} \right)_{c-d_c}^{c} \qquad (5\text{-}32)$$

Where, d_c is measured from the top of the section

5.4.2.2 Compressive Steel Contribution

The compressive steel force (C_s) is a direct linear relationship with the corresponding steel strain (ε_s'). This relationship was driven based on the assumption of the bilinear behavior for the steel analysis.

$$C_s = A_s' f_s' - A_s' f_c' ((2\frac{\varepsilon_s'}{\varepsilon_c'} - -\left(\frac{\varepsilon_s'}{\varepsilon_c'}\right)^2) \quad (5\text{-}33)$$

5.4.2.3 Tensile Concrete contribution

The concrete tensile capacity is divided into two main profiles

$$T_{c_1} = \int_0^{d_t} f_t . b \, dy \quad (5\text{-}34)$$

Where y is measured from the neutral axis and d_t is measured from the neutral axis

$$T_{c_1} = \frac{bE_c \varphi d_t^2}{2} \quad (5\text{-}35)$$

$$T_{c2} = \int_{d_{cr}}^{d_t} bf_t dy = b\int_{d_{cr}}^{d_t} 0.5f_r - \frac{0.5f_r}{\ln(\frac{1.4\varepsilon y}{\varepsilon_{cr}})} \ln\left(\frac{\varepsilon_t}{\varepsilon_{cr}}\right) dy \quad (5\text{-}36)$$

Where y is measured from the neutral axis

$$T_{c2} = [-\frac{0.5bf_r}{\ln(\frac{1.4\varepsilon y}{\varepsilon_{cr}})}(y\ln(\varphi) + yln(y) - y - yln(\varepsilon_{cr})) + 0.5f_r y]_{\varepsilon_{cr}/\varphi}^{d_t} \quad (5\text{-}37)$$

5.4.2.4 Tensile steel Contribution

The tensile steel force (T_s) follows the same bilinear behavior based on the following equations

$$T_s = A_s E_s \varepsilon_s, \; when \; f_s \leq f_y \quad (5\text{-}38)$$

$$T_s = A_s(f_y + E_s'(\varepsilon_s - \varepsilon_y)), \; when \; f_s > f_y \quad (5\text{-}39)$$

5.5 Constructing shear stress distribution

Typical shear stress profiles are numerically generated using Equations (5.32)-(5.40) substituted into Equation (5.31). Figure 5-8 presents the shear stress distribution for un-cracked section. The

stress profile is very similar to the classical parabolic shear stress distribution in linear beams except for the effect of dowel action shown at the level of tensile reinforcement. Figure 5-9 shows the shear stress distribution for a post-cracked concrete section. Figure 5-10 illustrates the shear stress distribution for post yielded section. It is evident that the shear stresses within the compression block start negative in value due to the descending part of Hognestad's parabola. Then these stresses shift to positive values. In addition, dowel action shift shear stresses to zero shear stress since tension stiffening is vanished at this stage of loading.

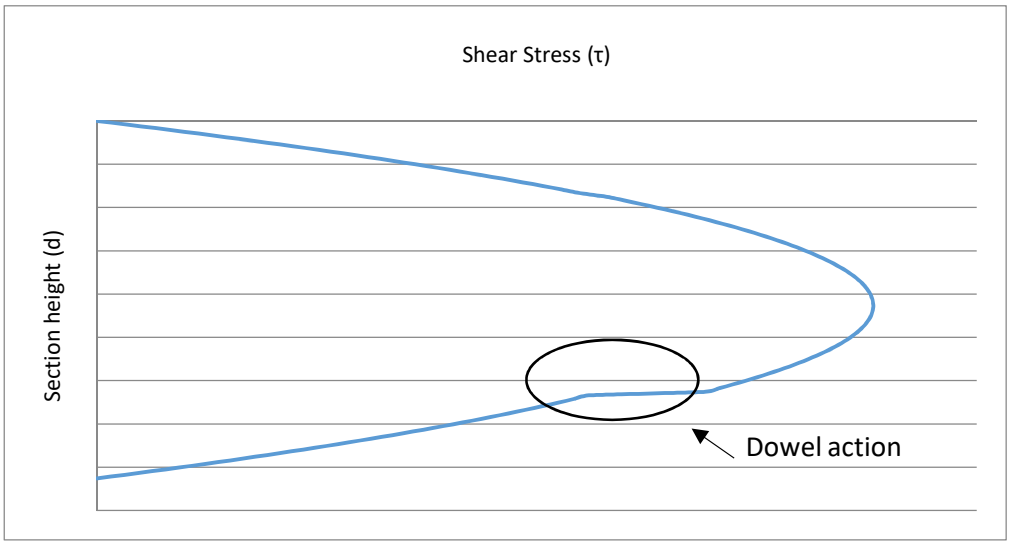

Figure 5-8 Typical pre-cracking shear stress distribution

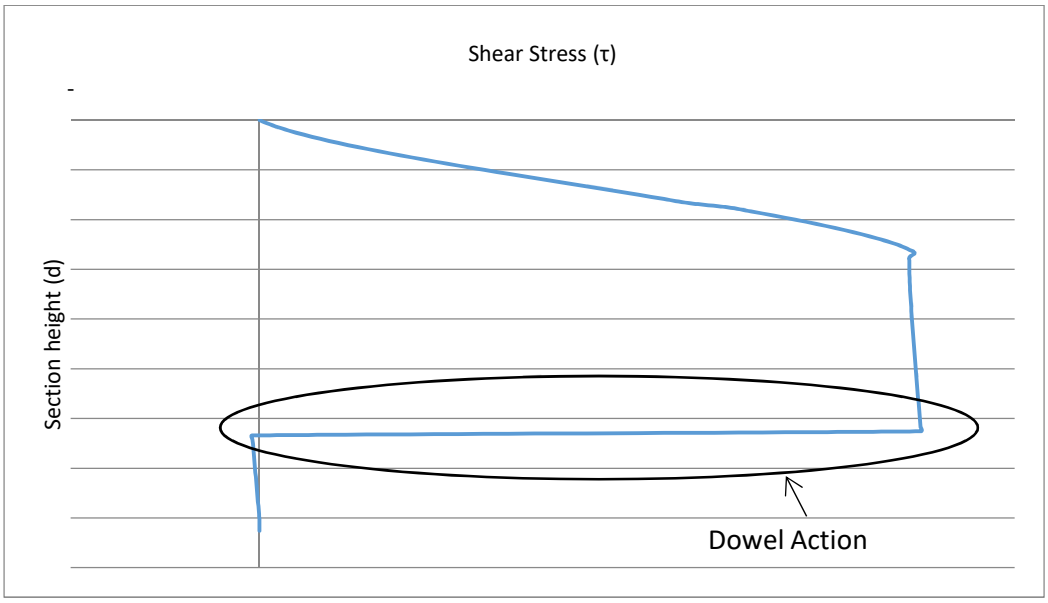

Figure 5-9 Typical post cracking shear stress distribution

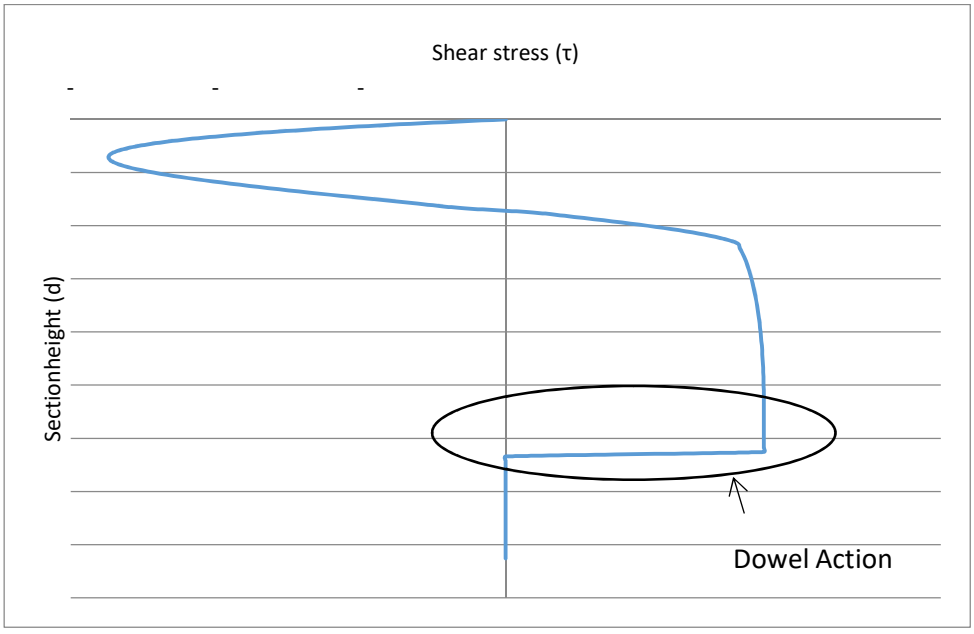

Figure 5-10 Typical post yielding shear stress distribution

5.6 Principal stresses analysis

5.6.1 Principal stress by Mohr's circle

By applying Mohr's Circle for each numerical node, the principle stresses σ_1, σ_2 and their orientations are calculated.

$\sigma_{avg} = \frac{\sigma_x + \sigma_y}{2}$ Where, σ_y=0 (beam theory) (5-40)

$R = \sqrt{\left(\frac{\sigma_x - \sigma_y}{2}\right)^2 + \tau_{xy}^2}$ (5-41)

max $principle\ stress\ \sigma_1 = \sigma_{avg}$+ R (5-42)

min $principle\ stress\ \sigma_2 = \sigma_{avg}$- R (5-43)

$Tan(2\theta) = \frac{2\tau_{xy}}{\sigma_x - \sigma_y}$ (5-44)

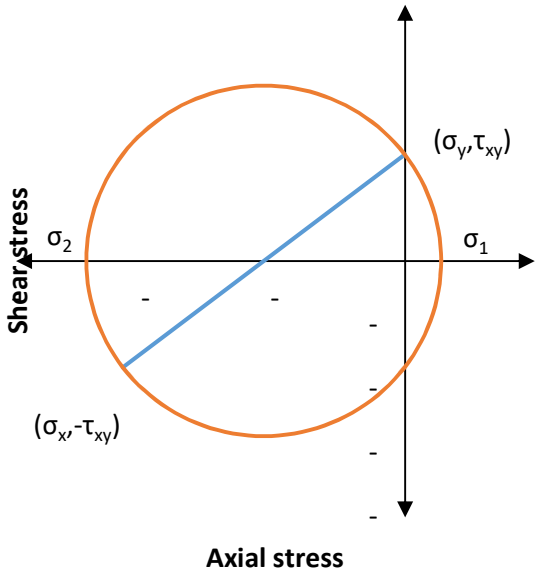

Figure 5-11 Mohr's circle

5.6.2 Modified Kupfer and Gerstle biaxial cracking criterion

Kupfer and Gerstle (1973) have suggested an analytical maximum strength envelope for biaxial loading in concrete. Complying with this envelope, Kupfer and Gerstle also proposed simplified expressions of biaxial strength for different stress combinations. For tension-compression stress state, Kupfer and Gerstle adopted a linear reduction of tensile strength in accordance with the increased compression

$$\sigma_{1t} = \left(1 - \frac{0.8\sigma_{2c}}{f'c}\right) f_r \qquad (5\text{-}45)$$

Where (σ_{1t}) is the major principal tensile stress and (σ_{2c}) is the minor principal compressive stress.

However, this equation does not represent well the case of high ratios of $\frac{\sigma_{2c}}{f'c} > 0.85$ (For example, at $\frac{\sigma_{1t}}{f'c} = 0$, $\frac{\sigma_{2c}}{f'c} = 1.25 > 1$) . Hence, a modified equation was developed here to represent that particular stress state. This equation describes the region $0.85 < \frac{\sigma_{2c}}{f'c} \leq 1$, see Figure 5-12. The linear equation for this segment is as follow

$$\frac{\sigma_{1t}}{f'c} = 0.192\frac{\sigma_{2c}}{f'c} + 0.192 \qquad (5\text{-}46)$$

if (σ_1(principal tensile stress) $\geq \sigma_{1t}$) {"Cracked Concrete"}

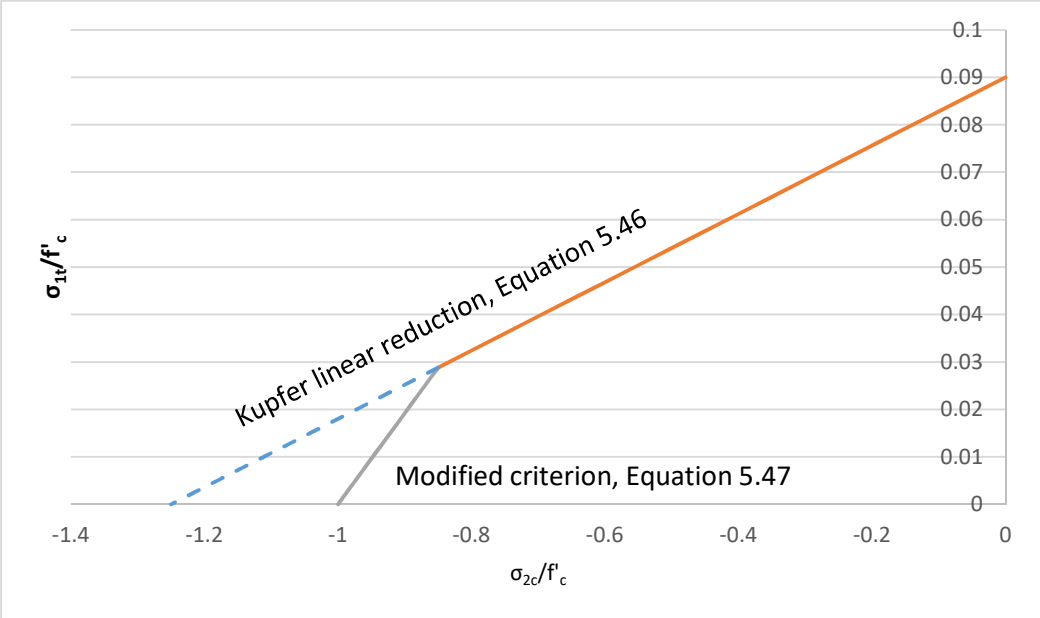

Figure 5-12 Concrete biaxial cracking criterion

5.7 Results

The formulation developed in this study is applied to retrieve the shear stress distribution of cracked concrete at the failure section under the maximum load. Furthermore, Mohr's circle is

used to extract the principal stresses across the beam depth while using the concrete biaxial cracking criterion (modified Kupfer-Gerstle criterion) to predict the cracks within the compression zone.

5.7.1 Example one

The goal of this example is to confirm the accuracy of the non-linear numerical sectional analysis used in this study to predict the sectional response of the beam. This beam was tested by Rasheed et al. (2015). The rectangular beam is a 305mm*153mm (6 in x 12) in cross section. It has a length of 4.88 m (16 ft) and a clear span of 4.72 m (15.5 ft). The main flexural reinforcement consists of 2φ16 (2 No. 5) bars with 2φ10 (2 No. 3) bars used for the compression steel, Figure 5-12.

The concrete nominal compressive strength was 34.5 MPa (5000 psi). While, the material properties of the reinforcing steel were 200,000 MPa (29000 ksi) for the modulus of elasticity and yield strength of 482.3 MPa (70 ksi).

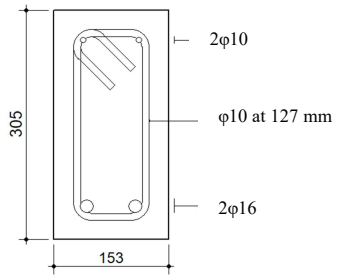

Figure 5-13 Beam R1 section tested by Rasheed et al. (2015)

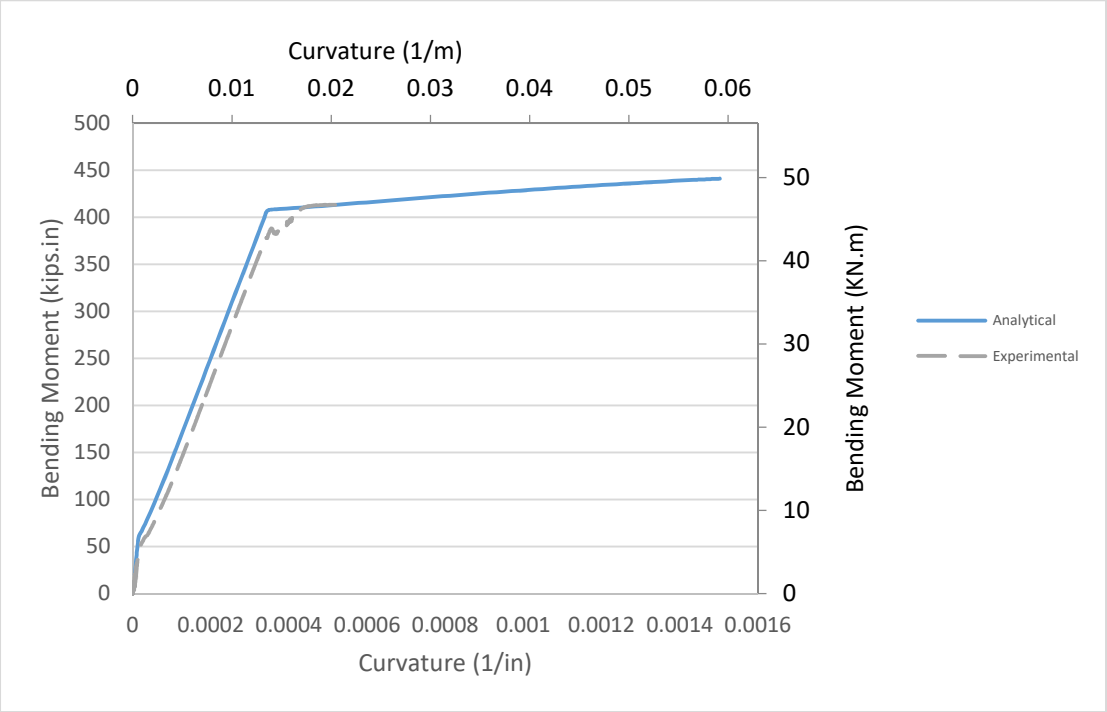

Figure 5-14 Moment-curvature of Beam R1 tested by Rasheed et al. (2015)

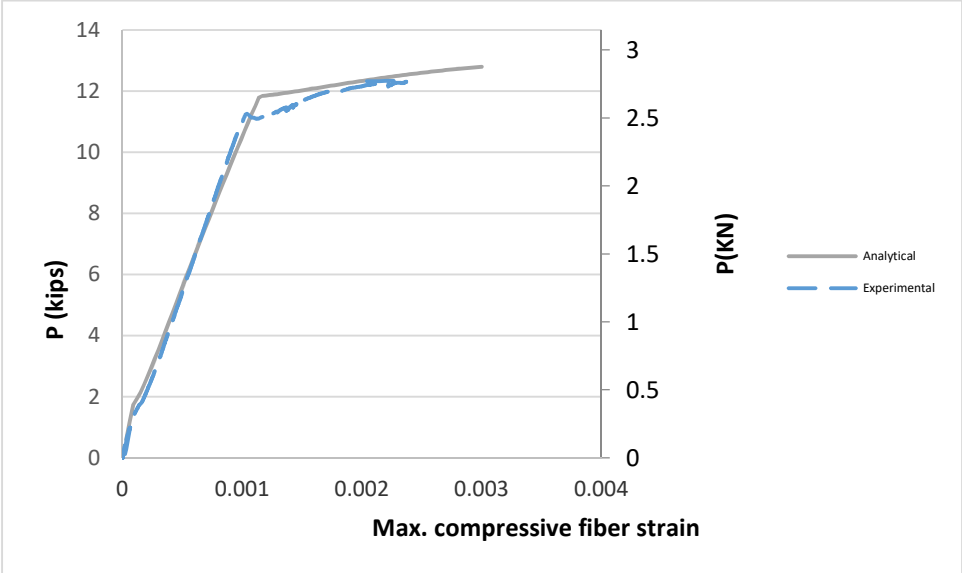

Figure 5-15 Load vs. Max. compressive fiber strain of beam R1 tested by Rasheed et al. (2015).

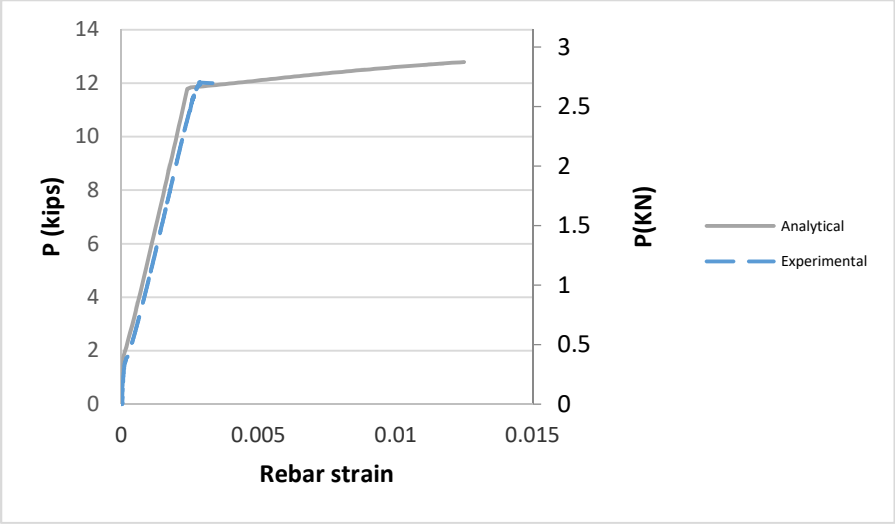

Figure 5-16 Load vs. rebar strain of beam R1 tested by Rasheed et al. (2015).

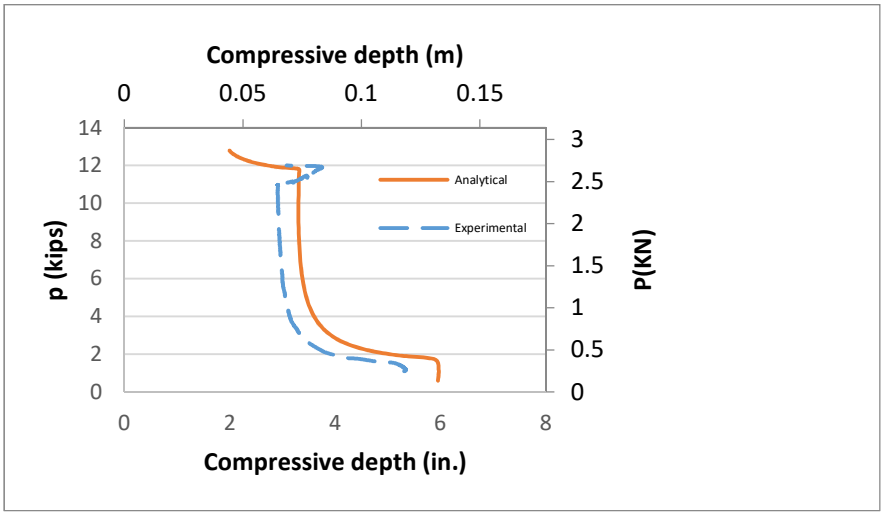

Figure 5-17 Load vs. neutral axis depth of beam R1 tested by Rasheed et al. (2015).

An excellent agreement of the experimental results is observed against the proposed numerical approach. Rasheed et al. (2015) tested this beam under four points bending with shear span of 175.3 mm (5.75 ft). Figure 5-14 and Figure 5-15 present a comparison between the numerical and the experimental data of the maximum compressive strain and the rebar strain. These two graphs show a very good agreement in the post cracking zone and the post yielding region up to the failure of the strain gages. The numerical variation of the neutral axis and the experimentally

evaluated neutral axis comparison is shown in Figure 5-16. A generally good correspondence is observed as well.

These comparisons are presented to illustrate the accuracy of the proposed method in predicting the sectional response of the beam. The bending moment-beam curvature comparison shows an excellent agreement of the sectional response of the beam.

5.7.2 Example two

The second example examined Almusallam (1997) beam. He tested a rectangular beam 200 mm x210 mm (7.87 in x 8.26) in four point bending. The beam has a length of 2.700 m (106.3 in) with a shear span of 1.25 m (49.2 in).The beam main flexural reinforcement consists of 3 φ 14 mm bars with 1 φ 6.25 mm bars used for the compression steel.

The concrete nominal strength is 31.3 MPa (4540 psi). The reinforcing steel has a yielding strength of 552.6 MPa (80.2 ksi) and a modulus of elasticity of 200000 MPa (29000 ksi).

In this second example, the axial stress distribution and the shear stress distribution as well as the principal stress distribution are calculated across the height of the beam at a section positioned just under the load at the failure of the beam. This section was chosen to study the concrete behavior at crushing.

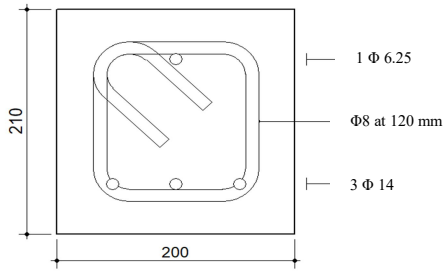

Figure 5-18 Almusallam 1997 beam cross section

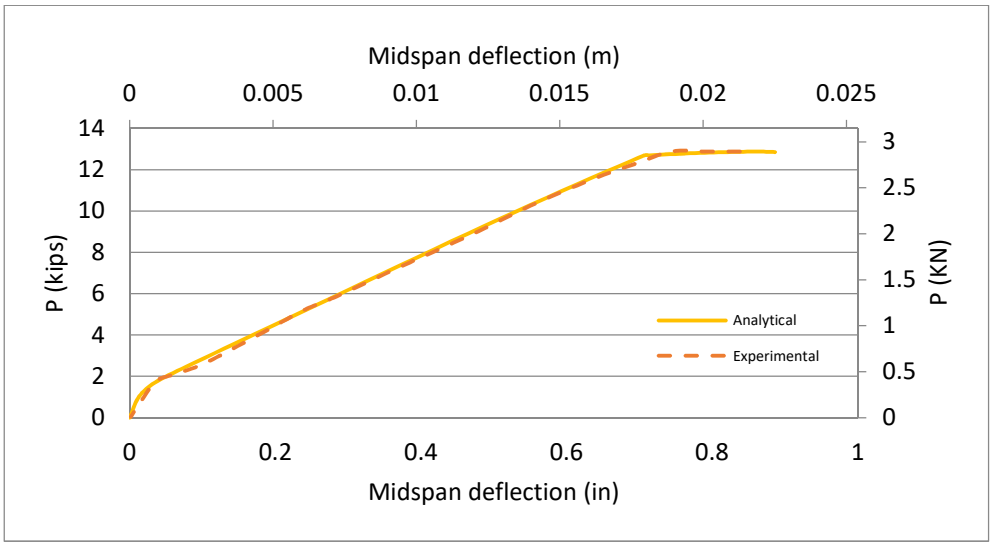

Figure 5-19 Load vs. mid-span deflection for beam tested by Almusallam 1997.

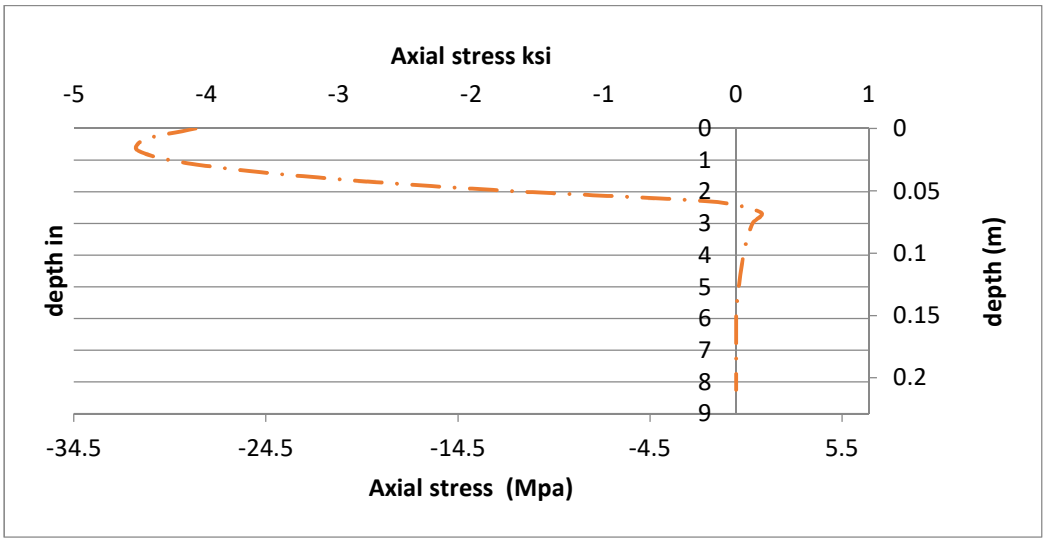

Figure 5-20 axial stress distribution at failure for beam tested by Almusallam 1997

The axial stresses over the height of the beam are calculated in accordance to the concrete material models defined earlier. Where, Hognestad's parabola describes the concrete behavior in compression up to the neutral axis. Under the failure load at the load location, the examined section shows the full Hognestad's parabola development, see Figure 5-20.

To continue with the analysis, shear stresses were then evaluated for the same section using the numerical shear differential equation. For each given section, a preceding section at an infinitesimal distance was taken to be analyzed. In order to compute the shear stress at any given depth (d), the axial forces within the depth (d) for the two successive sections are calculated. Then, the shear stress is found by numerically applying Equation (5.31). The shear stress distribution varies depending on the section location. The examined section is located in the post yielding zone, where the tensile steel has yielded. Figure 5-23 shows the calculated shear stress distribution under ultimate moment at failure. Over the height of the beam, the shear stress profile shows different behaviors which depend on its location. Zone A, see Figure 5-21, describes shear stress profile within the compression zone, it shows a parabolic behavior with a change in shear direction (sign). The next zone, Zone B, starts at the neutral axis and goes through the concrete tensile contribution up to the tensile steel level. At which, dowel action is observed. Dowel action marks the beginning of the third zone (Zone C) where the shear stresses sums up to zero through the entire cover of the beam.

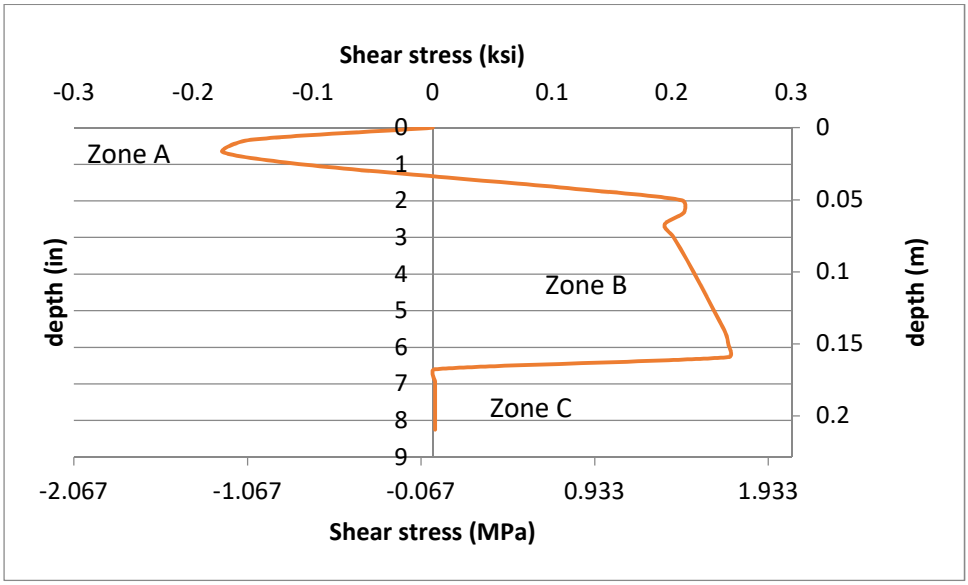

Figure 5-21 shear stress distribution of section three for beam tested by Almusallam 1997

In section three at the failure load just under the concentrated load point, Figure 5-21, it is interesting to observe the opposite change in direction of the shear stresses within the compressive depth. This change is a result of the descending branch of the Hognestad's parabola. Figure 5-22 shows the stress profiles of three different sections in the post yielding zone. The first section represents the early stages of the post yielding zone. At this section, the shear stress sign (direction) does not change. The same observation is made for the second profile that is located slightly prior to the critical section. Section three, at failure, shows the change of the shear stress direction (from negative to positive). This similar change of shear stress direction also appears over a short distance including few sections just before the maximum moment section (i.e. at sections with moments around 97%-100% of the failure moment).

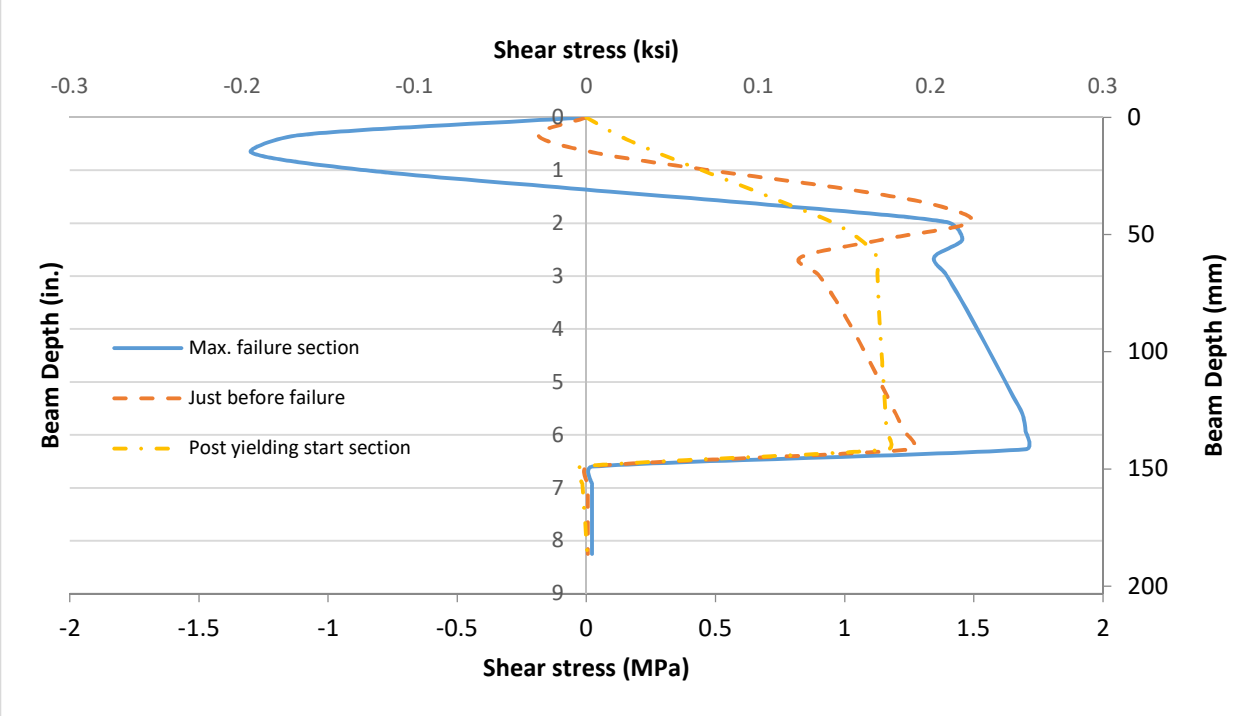

Figure 5-22 Shear stress distributions of three different sections within the post yielding zone for beam tested by Almusallam 1997

Using Mohr's circle and the calculated axial and shear stresses, the principal stresses were generated. Figure 5-23 shows the variation in the major/tensile principal stress for the given section. On the other hand, Figure 5-24 presents the variation of the minor/compressive principal stresses. The two principal stresses were then applied to the biaxial concrete failure criterion to predict the location and orientation of the cracked concrete.

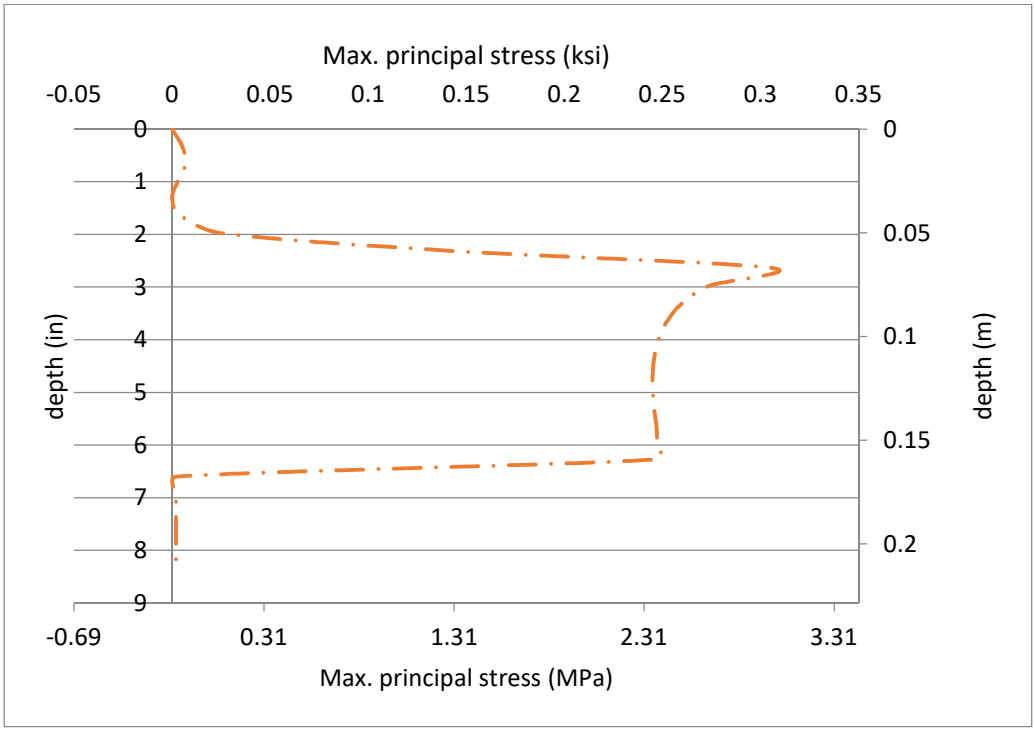

Figure 5-23 Tensile principal stresses of the maximum moment section for beam tested by Almusallam 1997

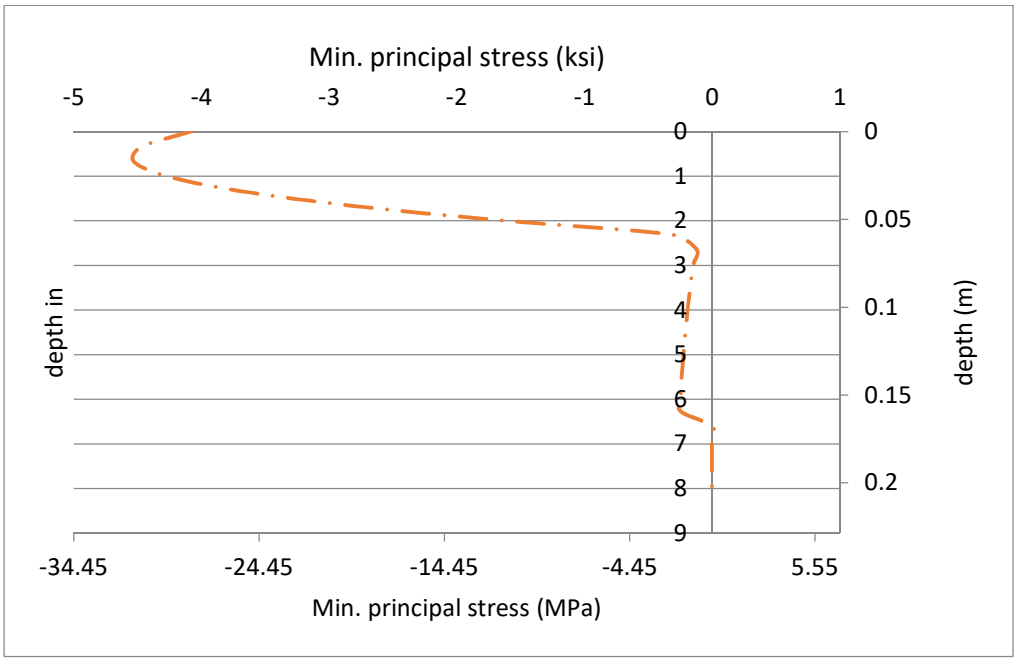

Figure 5-24 Compressive principal stresses of the maximum moment section for beam tested by Almusallam 1997

5.7.2.1 Formation of concrete tensile cracks

At the later load stages near failure, the shear span was divided into a number of sections. Each section was divided into a number of nodes at equal spaces across the height of the section. The proposed analysis was applied on each node to determine if it was cracked. In Figure 5-25, the cracked concrete map is generated using the proposed approach in the post yielding zone for a range of 97% to 100% of the maximum load. The generated cracks within the upper region of the compression zone appear to take a dish-like shape as observed in the experimental results from literature of concrete crushing failure. This finding comes as a result of the axial-shear combined stress state in that zone. Figure 5-26 shows the principal stress state of an element at the upper region of the compression zone under the maximum load. Note that the section depth in Figure 5-25 is measured from the beam bottom surface.

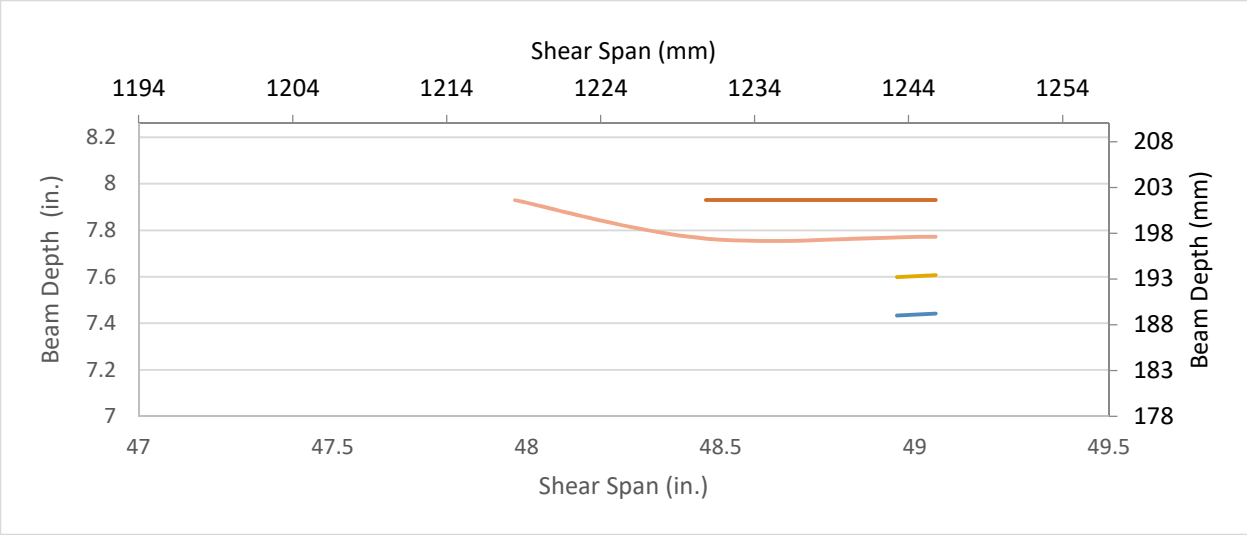

Figure 5-25 Cracks map just below the top of the section at the post yielding zone for beam tested by Almusallam 1997

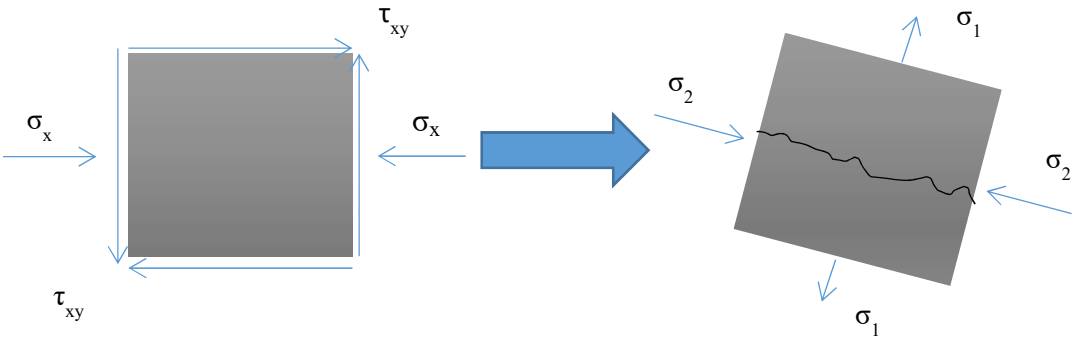

Figure 5-26 The principal stress state of an element in the upper region of the compression zone under the maximum load

5.8 Conclusions

In this study, a new mechanics-based approach is developed to mathematically demonstrate the concrete crushing failure mode of reinforced concrete beams. The actual stress state of a beam element within the compression zone is considered under the assumption of the smeared crack approach. The combination of axial stresses and shear stresses within the compression zone was

used to explain the occurrence of concrete cracking at the crushing point below the top surface through a dish–like crack that develops at the location of maximum moment. The shear stress distribution was numerically retrieved through the transversal shear differential equation and was found to be reversed in this compression region leading to the dish–like crack. This shear stress distribution combined with axial compressive stresses yields tensile-compressive principal stress state that predicts cracking when a biaxial concrete failure criterion is invoked. This study concludes that the concrete crushing is nothing but an oriented principal tensile cracking, which is very similar in behavior and nature to shear or diagonal tension cracks.

5.9 References

Almusallam, T.H., (1997). "Analytical Prediction of Flexural Behavior of Concrete Beams Reinforced by FRP Bars," Journal of Composite Materials, Vol. 31, No. 7, pp 640-657.

Bazant, Z. P., (1984) "Size Effect in Blunt Fracture Concrete, Rock, Metal," Journal of Engineering Mechanics, ASCE, V. 110, No. 4, pp. 518- 535.

Gonnerman, H. F., (1925)"Effect of Size and Shape of Test Specimen on Compressive Strength of Concrete," ASTM, V. 25, pp. 237-250.

Hognestad, E.; Hanson, N. W.; and McHenry, D., (1955) "Concrete Stress Distribution in Ultimate Strength Design," ACI JOURNAL, Proceedings V. 52, No. 4, pp. 455-479

Moody,K.G., Viest, I.M., Elstner, R.c., and Hognestad,E. (1954) "Shear Strength of Reinforced Concrete Beams, Part-1 Tests of Simple Beams ". ACI Journal, proceedings Vol. 51, pp. 317-332.

Portland Cement Association. (2013). Notes on ACI 318-11. "Building Code Requirements for Structural Concrete with Design Applications". 12th edition, Edited by M. E. Kamara and L. C. Novak. Skokie, IL. Portland Cement Association.

Rasheed, H. A., (1990) "Inelastic Behavior of Reinforced Concrete Frame Structures". M.Sc. Thesis, University of Baghdad, Iraq.

Rasheed, H. A., Decker, B. R., Esmaeily, A., Peterman, R. J., & Melhem, H. G. (2015). The influence of CFRP anchorage on achieving sectional flexural capacity of strengthened concrete beams. Fibers, 3(4), 539-559.

Zwoyer, E.N., and Siess, C.P., (1954) “Ultimate Strength in Shear of Simply-Supported Prestressed Concrete Beams Without Web Reinforcement”. ACI Journal, Proceedings Vol. 51, pp. 181-200.

Chapter 6 - Experimental program

Due to the scarcity of flexural reinforced concrete beam tests that reflect the cracking parameters, a small sized experimental program is conducted .The experimental program consists of designing and testing one full scale concrete beams. The beam is designed to fail in concrete crushing after the yielding of the tensile steel. Four-points bending test setup is chosen to reflect the goal of this study. Series of comparisons between the experimental and the numerical results are held to validate the accuracy of the presented approach.

6.1 Beam Geometry

The rectangular beam is a 305 mm*153 mm (6 in x 12) in cross section. It has a length of 4.88 m(16 ft) with a clear span of 4.72 m(15.5 ft) . The main flexural reinforcement consists of 2φ16 (2 No. 5) bars with 2φ10 (2 No. 3) bars used for the compression steel just to provide a caging framework for the shear reinforcement.

The concrete that was used in casting the beam is ready mix with a mix design nominal compressive strength of 34.5 MPa (5000 psi). The material properties of the reinforcing steel were provided by the manufacturer to have a modulus of 200,000 MPa(29000 ksi) and yield strength of 482.3 MPa(70 ksi).

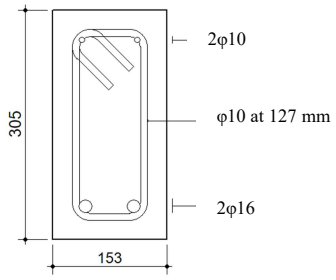

Figure 6-1 Tested beam cross section

6.2 Material Properties

The concrete that was used in casting the six beams is ready mix with a mix design nominal strength of 5000 psi (34.5 MPa). While casting the beams, 6 cylinders were also prepared for the actual material testing. The cylinders were 4in. x 8in. and were tested in compression after 28 days. The results of these cylinders tests showed an average of 5.3 ksi comparing to 5 ksi nominal design strength.

Figure 6-2 Concrete cylinder compression test (before test)

Figure 6-3 Concrete cylinder compression test (after test)

Figure 6-4 Steel tensile test

Regarding the steel reinforcement, three 6-inch steel specimens of each of the tension and compression were tested in tension at by KDOT research lab. The modulus and yield strength of the No. 3 bars (compression steel) were 28500 ksi and 80.1 ksi, respectively. These values represent the average test results of 3 samples. The modulus and yield strength of the No. 5 bars (tension steel) were 28000 ksi and 64.5 ksi, respectively.

6.3 Construction of Formwork and Caging

The fabrication of all wooden formwork and steel rebar caging was at Kansas State University facilities. Since the plywood that is used for the bed of the formwork is available only in 4’ x 8’ sheets, the forms had to be fabricated in two halves then combined to create a 16 ft long form.

Figure 6-5 Form work (front view)

Figure 6-6 Form work

Figure 6-7 Form work (side view)

Figure 6-8 Steel cage work

Eight strain gages at three different locations were used to capture the tensile strain along the beam depth. The first location is within the shear span at 49 inches from the mid-span. The second location is within the shear span at 47 inches from the mid-span of the other side of the beam. The third location is at the mid-span. The first and the second location had two strain gages; one at the tensile steel level and one on the top surface of the beam. The third location, at mid-span, included four strain gages, where two were located on the steel and two were located on the top surface to capture the maximum compressive strain.

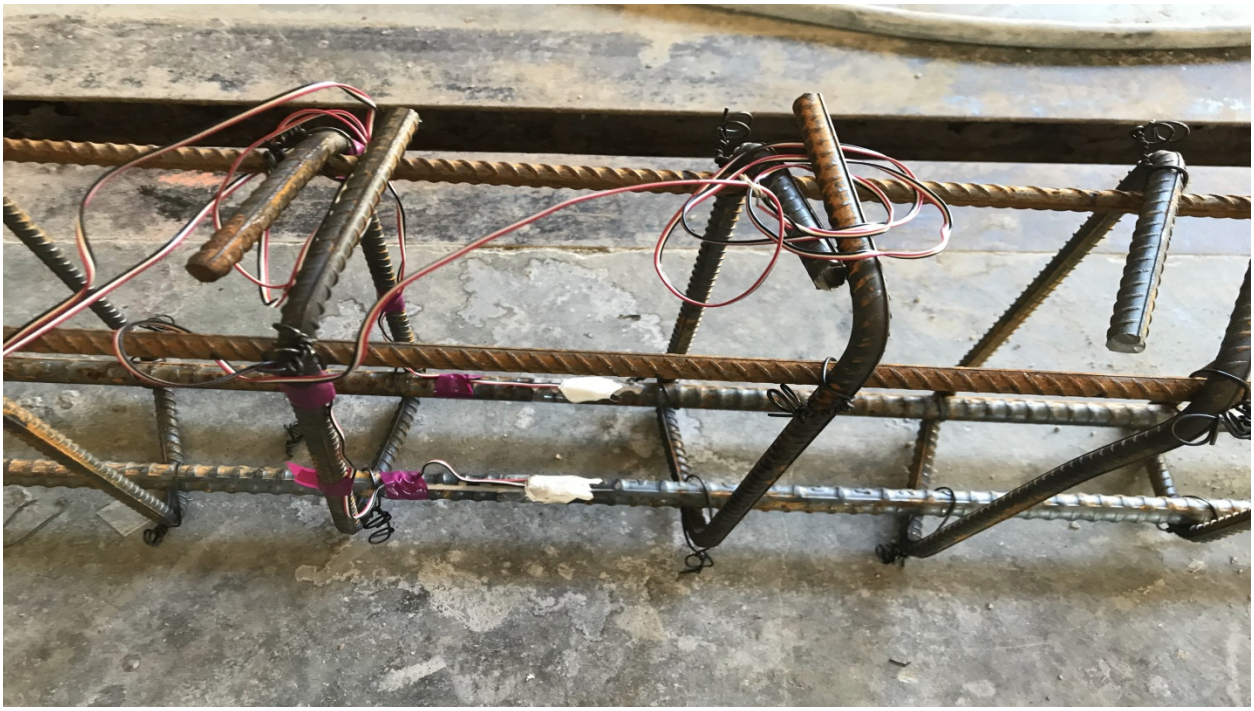

Figure 6-9 Tensile steel strain gages

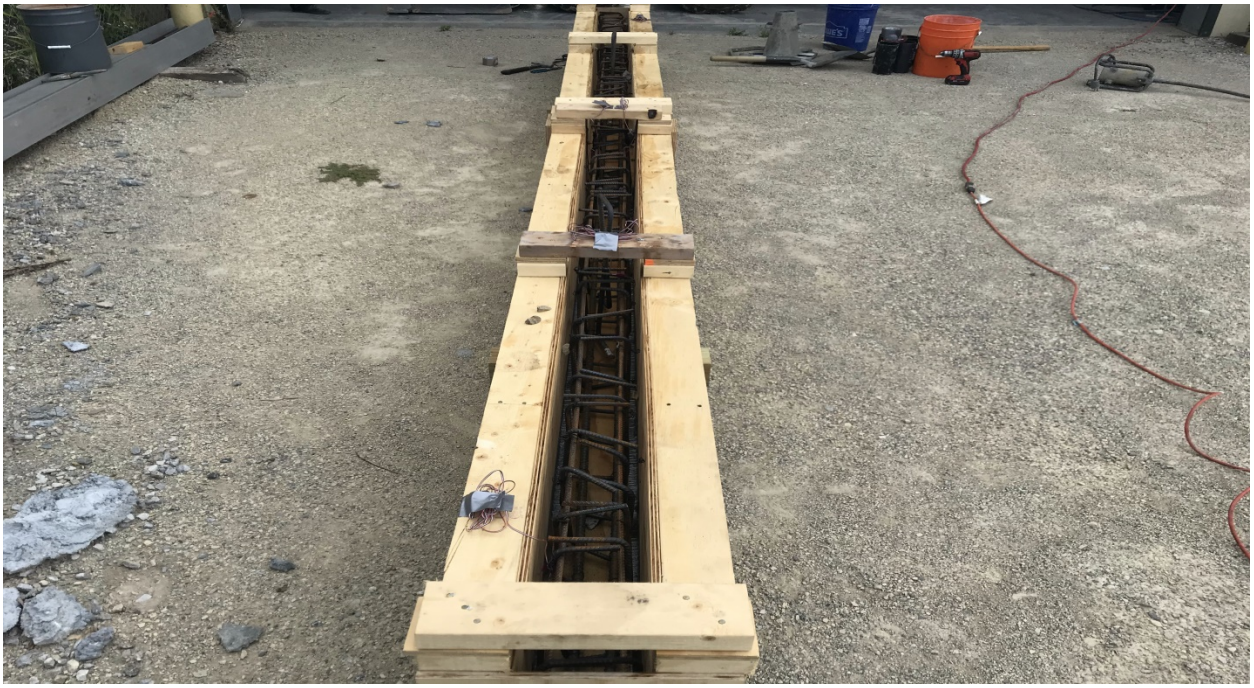

Figure 6-10 Form work and cage work

Figure 6-11Form work and cage work with strain gages

Figure 6-12 Casted reinforced concrete beam (front view)

Figure 6-13 Casted reinforced concrete beam (side view)

Figure 6-14 Casted reinforced concrete beam

6.4 Test Setup

The beam was tested in four-point bending using a 4-ft long steel spreader beam and. The beam was simply supported with plates and rollers at the supports. The supports are placed 3 inches (75 mm) from the edge of the beam, providing a clear span of 15.5 ft (4724.4 mm).

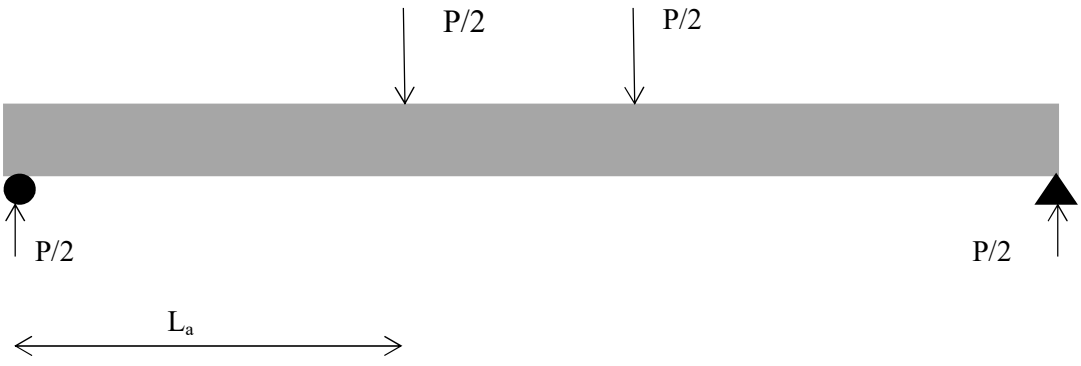

Figure 6-15 Profile of simply supported beam under four-point bending

Figure 6-16 Test setting

Figure 6-17 Spreader beam

6.5 Test Results

The beam failed in ductile behavior, where the tensile steel yielded at 5.78 kips before the concrete fails at 5.8 kips with a maximum compressive strain of 0.0038. The experimental moment-curvature, moment-maximum compressive strain, load-maximum compressive strain, load-rebar stain were generated and compared to the presented nonlinear sectional analysis.

A very good agreement was observed for the moment versus curvature as well as moment versus maximum compressive strain. These comparisons confirm and validate the accuracy of the proposed sectional analysis response. Furthermore, the experimental numerical derivative of the variation of the strain profile parameters were compared to the numerical derivative found through the proposed approach.

Figure 6-18 Tested beam concrete failure

Figure 6-19 Tested beam principal tensile cracking (side one)

Figure 6-20 Tested beam principal tensile cracking (side two)

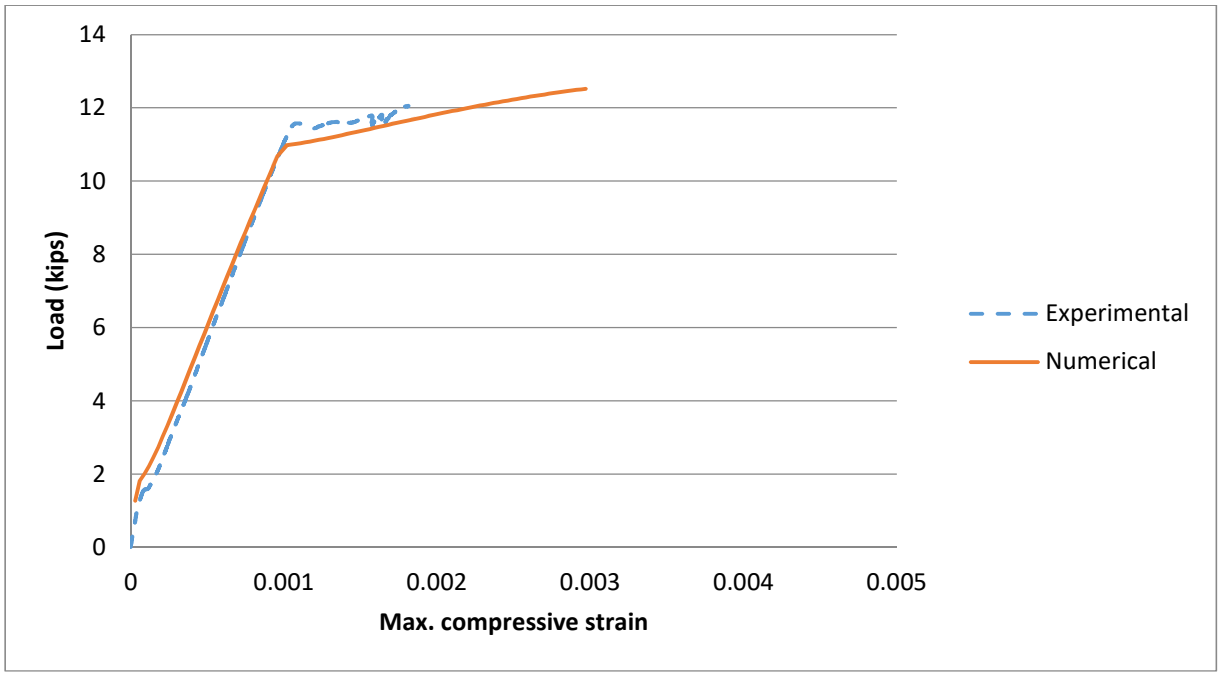

Figure 6-21 Load-max. compressive strain graph of the tested beam

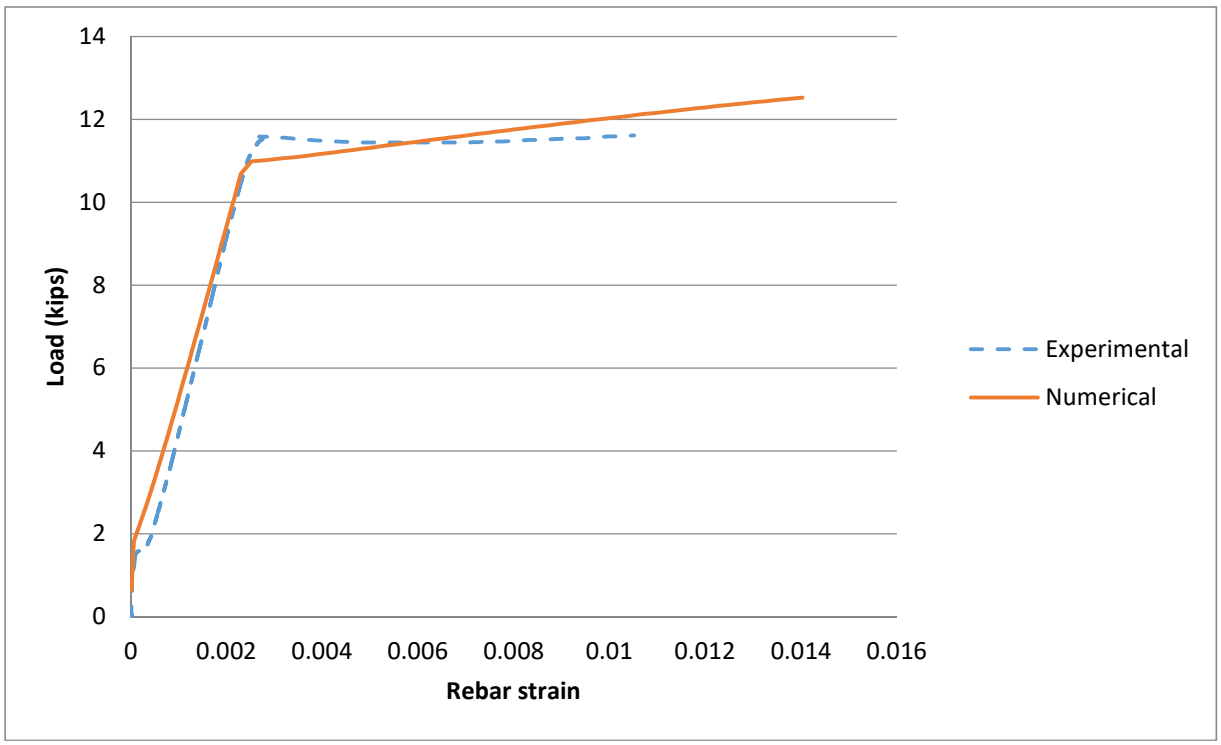

Figure 6-22 Load-rebar strain graph of the tested beam

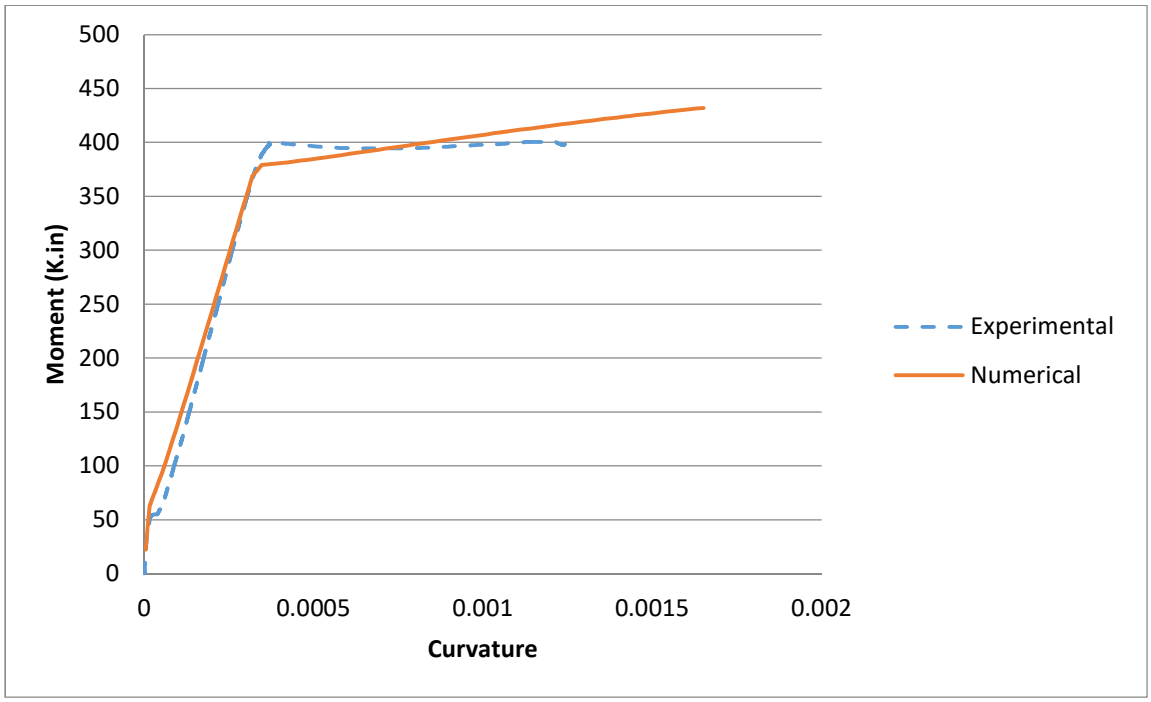

Figure 6-23 Moment-curvature graph of the tested beam

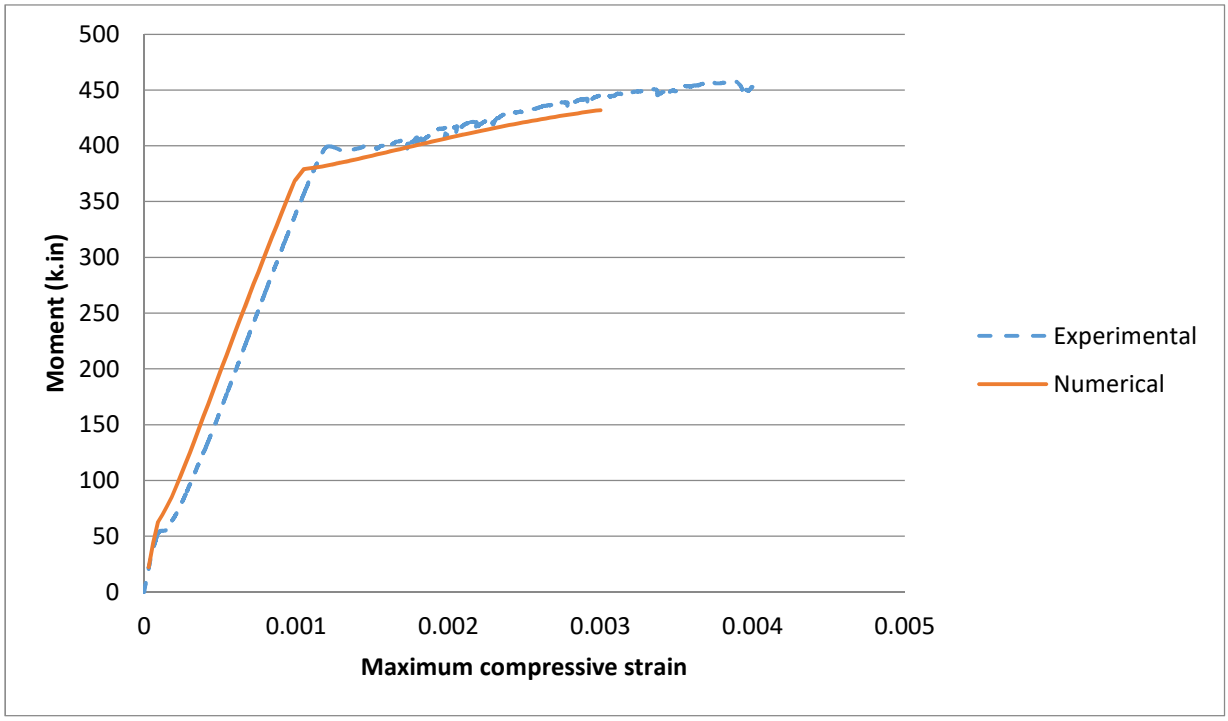

Figure 6-24 Moment-maximum compressive strain graph of the tested beam

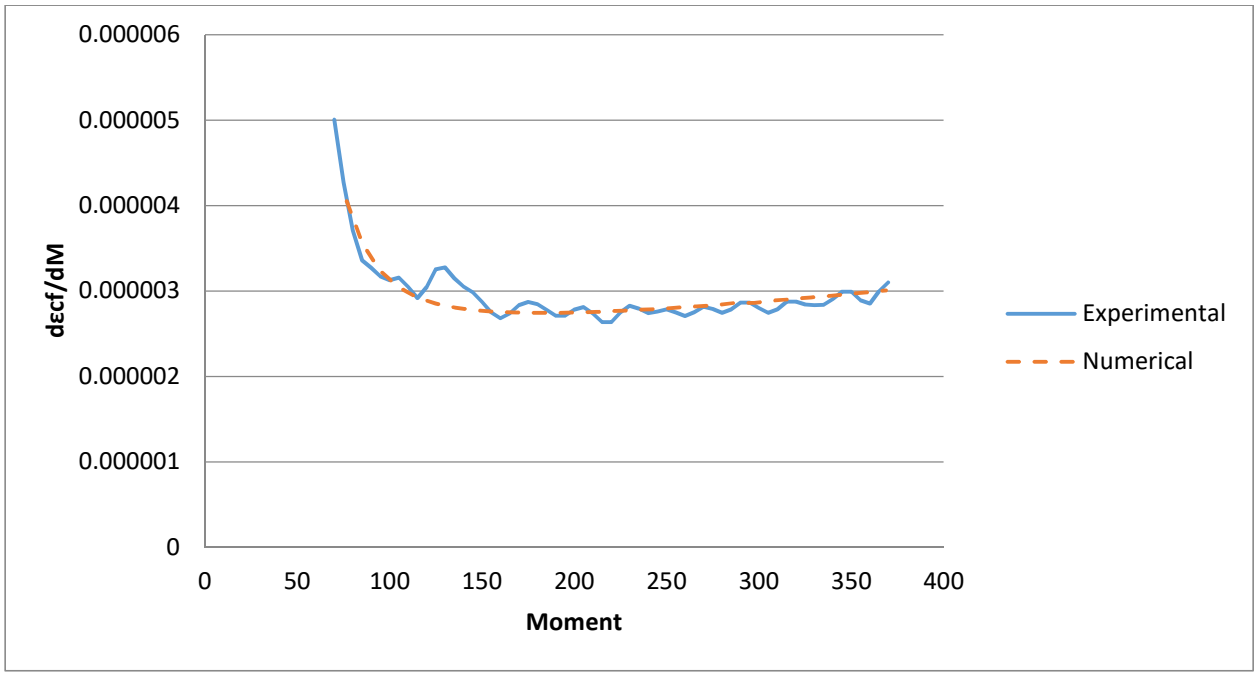

Figure 6-25 Moment- $d\varepsilon_{cf}/dM$ graph of the tested beam

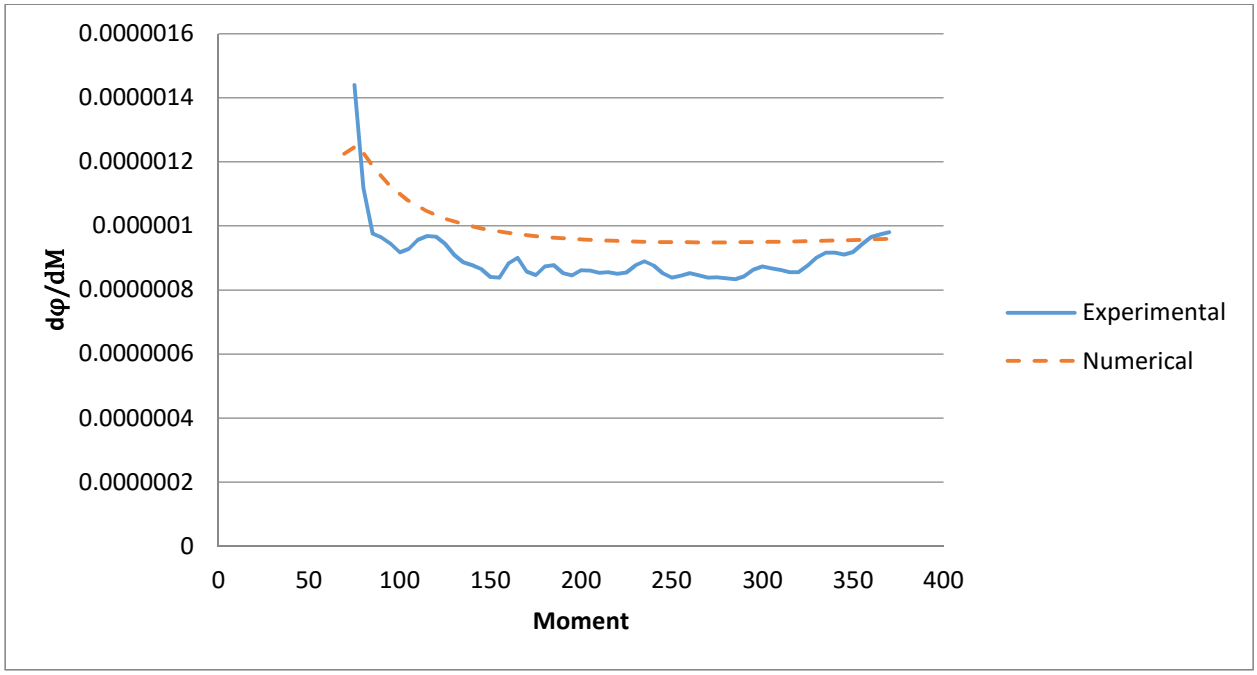

Figure 6-26 Moment- dφ/dM graph of the tested beam

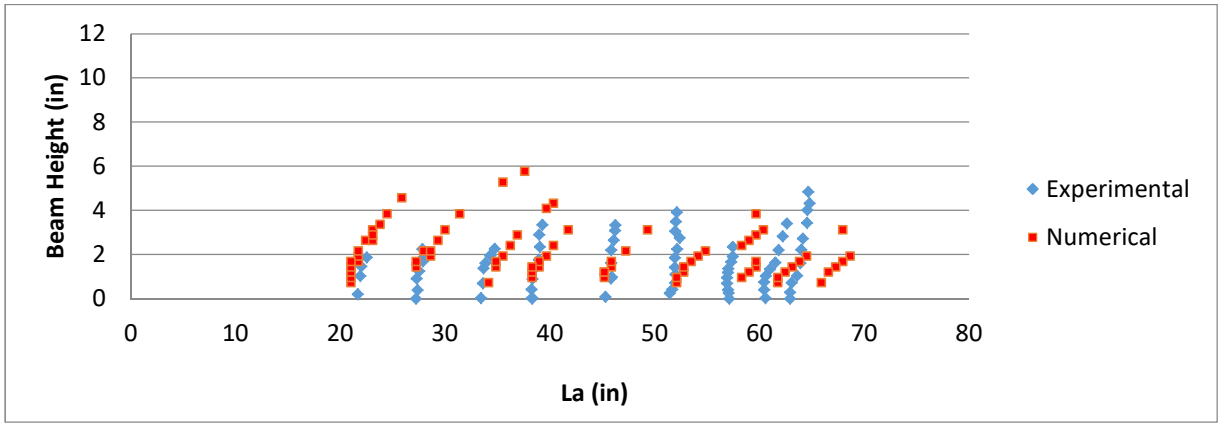

Figure 6-27 Shear cracks comparison (Numerical vs. Experimenta)

Chapter 7 - Conclusions and Recommendations

7.1 Conclusions

The first part of this study was conducted to develop a tensile constitutive model for nonlinear analysis of flexural concrete beams reinforced with steel bars. An incremental-iterative numerical analysis was followed to study the nonlinear flexural beam behavior and generate the analytical graphs. The proposed tensile constitutive model has a sudden drop at cracking strain, followed by a descending curve up to zero at($1.4\varepsilon_y$). Series of comparisons were performed to validate the accuracy of the adopted model against the global experimental behavior for a large pool of beams. Two extra comparisons were conducted to check the applicability of the model against the sectional response of different beams. As a result of these comparisons, the model showed an excellent agreement with the validating experiments for the sectional and the global responses.

A secondary goal of this step was to confirm the trilinear behavior for moment versus curvature and moment versus maximum compressive strain graphs. Through all the comparisons in this study, and by using the proposed model, the trilinear behavior was observed in all the sectional and the global responses. Even though the literature has several tension stiffening models, the authors believe that this new model is more objective since:

1. The final degradation of cracked concrete is related to the yielding strain in steel rather than multiples of the cracking strain of the concrete.
2. The loss of energy due to cracking fracture is captured in a more pronounced way than earlier model.
3. The current model furnishes a single mathematical expression making it easier to implement in analytical formulations.

In this study, a novel non-linear formulation was developed using the smeared crack approach. It is used to predict the shear stress profile along the shear span of shallow beams in flexural cracked concrete at all stages of loading up to flexural failure. These shear stress profiles are coupled with the nonlinear axial stress profiles to obtain the principal stress distribution along the shear span. Kupfer and Gerstle failure criterion is used to predict the likely occurrence of new shear-flexural cracks by setting the major principal stress equal to the limit provided by the Kupfer criterion.

It is interesting to observe the prediction of diagonal tension cracks along a curved path, which is expected to be much more accurate than other shear theories that assume a constant shear crack orientation.

An analytical formulation of shear stress distribution in cracked reinforced concrete, throughout its stages of post-cracking and post yielding, is presented using the smeared crack approach. This formulation uses the transverse shear differential equation to compute the shear stress at any given depth across the height of the beam through the derivative of axial forces acting above that desired depth. While the axial forces are found in accordance with the corresponding strains profile, which is computed by idealizing the sectional response of the beam to trilinear sectional relationships. Furthermore, the effect of the longitudinal steel on shear stress distribution, known as dowel action, is computed for the first time and found to be significant enough not to be ignored as typically done in design codes. In addition, the study provided a detailed evaluation of the variation of the strain profile parameters (φ, ε_{cf}) with respect to shear span or the corresponding moment, which is found to be non-linear compared to other studies that assume it as a constant. This analytical formulation was then applied to an experimental study to retrieve the shear stresses at three different cross sections under different applied loads. It is interesting to

observe for the first time from the generated shear profiles certain key features of the behavior that may prove to be very useful in interpreting shear failures.

Regarding concrete crushing, a mechanics-based approach is developed to mathematically demonstrate the concrete crushing failure mode of reinforced concrete beams. The actual stress state of a beam element within the compression zone is considered under the assumption of the smeared crack approach. The combination of axial stresses and shear stresses within the compression zone was used to explain the occurrence of concrete cracking at the crushing point below the top surface through a dish–like crack that develops at the location of maximum moment. This study concludes that the concrete crushing is nothing but an oriented principal tensile cracking, which is very similar in behavior and nature to shear or diagonal tension cracks.

7.2 **Recommendations**

From the major conclusions presented in the preceding section, additional works could be made in the future, as follows

1. Combine the discrete crack approach which would result into a more accurate prediction of crack locations
2. Develop a simplified approach for easier application.
3. Generate a complete a comprehensive software to predict the tensile cracking as well as the concrete failure in the compression zone.